SYNTHESIS AND CHARACTERIZATION OF MULTIWALLED CARBON NANOTUBES-SILVER NANOPARTICLES REINFORCED POLYVINYL ALCOHOL NANOCOMPOSITES (PVA/MWNT-AgNP) AS HIGH PERMITTIVITY MATERIALS

YUSLIZA BINTI YUSOF

FACULTY OF ENGINEERING
UNIVERSITY OF MALAYA
KUALA LUMPUR

2019

SYNTHESIS AND CHARACTERIZATION OF MULTIWALLED CARBON NANOTUBES-SILVER NANOPARTICLES REINFORCED POLYVINYL ALCOHOL NANOCOMPOSITES (PVA/MWNT-AgNP) AS HIGH PERMITTIVITY MATERIALS

YUSLIZA BINTI YUSOF

THESIS SUBMITTED IN FULFILMENT OF THE REQUIREMENTS FOR THE DEGREE OF DOCTOR OF PHILOSOPHY

FACULTY OF ENGINEERING
UNIVERSITY OF MALAYA
KUALA LUMPUR

2019

UNIVERSITY OF MALAYA
ORIGINAL LITERARY WORK DECLARATION

Name of Candidate: Yusliza Yusof

Registration/Matric No: KHA 120008

Name of Degree: Doctor of Philosophy (Ph.D)

Title of Project Paper/Research Report/Dissertation/Thesis (“this Work”):

Synthesis and Characterization of Multiwalled Carbon Nanotubes Reinforced Polyvinyl Alcohol Nanocomposites (PVA/MWNT-AgNP) as High Permittivity Materials

Field of Study: NANOMATERIALS ENGINEERING

I do solemnly and sincerely declare that:

(1) I am the sole author/writer of this Work;
(2) This Work is original;
(3) Any use of any work in which copyright exists was done by way of fair dealing and for permitted purposes and any excerpt or extract from, or reference to or reproduction of any copyright work has been disclosed expressly and sufficiently and the title of the Work and its authorship have been acknowledged in this Work;
(4) I do not have any actual knowledge nor do I ought reasonably to know that the making of this work constitutes an infringement of any copyright work;
(5) I hereby assign all and every rights in the copyright to this Work to the University of Malaya (“UM”), who henceforth shall be owner of the copyright in this Work and that any reproduction or use in any form or by any means whatsoever is prohibited without the written consent of UM having been first had and obtained;
(6) I am fully aware that if in the course of making this Work I have infringed any copyright whether intentionally or otherwise, I may be subject to legal action or any other action as may be determined by UM.

Candidate’s Signature Date:

Subscribed and solemnly declared before,

Witness’s Signature Date:

Name:

Designation:

ABSTRACT

This study about tailoring high dielectric permittivity of multiwalled carbon nanotubes-silver nanoparticles reinforced polyvinyl alcohol nanocomposites (PVA/MWNT-AgNP). The combination of MWNT and silver nanoparticles (AgNP) is an alternative way to yield high permittivity (ε) polymer composites that is favorable for electrical/electronic industry with attractive features. The hybrid fillers of MWNT-AgNP are produced via a single step route of chemical reduction method prior to the solution mixing process with PVA matrix. The characterization of the as-synthesized MWNT-AgNP was done using Raman spectroscopy, Fourier transform infrared (FTIR), field emission scanning microscopy (FESEM) and transmission electron microscopy (TEM). The properties of PVA/MWNT-AgNP nanocomposites with different AgNP contents are characterized in terms of morphology, structure properties, thermal stability, electrical and dielectric properties. Main finding shows that the inclusion of MWNT-AgNP in PVA matrix not only improves the electrical conductivity, but at the same time triggers a significant increase in dielectric permittivity of the nanocomposites. Impedance spectroscopy analysis shows high dependence of ac-conductivity, σ_{ac} and dielectric permittivity, ε' over frequency within 100 Hz to 1MHz. The maximum value of σ_{ac} is $4.0\text{x}10^{-5}$ S/m and ε' is about 600 for the nanocomposites containing 1.0 wt% of AgNP. FESEM analysis reveals random distribution of MWNT embedded in the matrix with high irregular interfaces can act as the conductive bridges when in contact together with AgNP. The average particles size of AgNP was found in the range of 17nm to 55nm. In addition, UV-vis analysis correlates other results with the absorption of visible light to the occurrence of charge transfer process between the fillers and the matrix. Vector network analyzer (VNA) further evaluates electromagnetic properties of the nanocomposites at a higher frequency of 8 to 12 GHz (X-band). In this part, the ε' value of the nanocomposite containing 1.0 wt% of AgNP remains stable at 25 over the X-band frequency, while the permeability μ', is approaching close to 0.5 due to low susceptibility of the nanocomposites with magnetic field. Both properties influence the ability of these nanocomposites to reduce the amount of transmitted electromagnetic waves. This is attributed to a higher wave absorption than the reflection behavior of the nanocomposite with the increased of AgNP-dielectric interfaces. Overall, PVA/MWNT-AgNP nanocomposite is promising material to impart high permittivity with good electromagnetic absorption. Thus, it can offer great potentials in electrical applications such as high-energy storage and dielectric-wave absorbance materials at high frequency.

ABSTRAK

Kajian ini melibatkan penghasilan bahan berketelusan tinggi oleh polivinil alkohol komposit nano yang diperkuatkan dengan nanotiub karbon pelbagai dinding-nanopartikel perak (PVA/MWNT-AgNP). Kombinasi di antara nanotiub pelbagai dinding (MWNT) dan nanopartikel perak (AgNP) merupakan satu kaedah alternatif untuk menghasilkan komposit polimer yang berketelusan tinggi bersesuaian untuk keperluan industri elektrik / elektronik dengan ciri-ciri yang menarik. Hibrid MWNT-AgNP dihasilkan melalui satu langkah tunggal berdasarkan kaedah penurunan kimia sebelum proses pencampuran larutan dengan matrik PVA. Pencirian MWNT-AgNP dilakukan menggunakan spektroskopi Raman, transformasi fourier inframerah (FTIR), mikroskopi elektron imbasan pancaran medan (FESEM) dan mikroskop elektron (TEM). Sifat-sifat komposit nano PVA / MWNT-AgNP dengan kandungan AgNP yang berbeza dicirikan dari sifat morfologi, struktur, kestabilan haba, serta sifat elektrikal dan dielektrik. Hasil penemuan utama menunjukkan kemasukan MWNT-AgNP bukan sahaja meningkatkan konduksi elektrik, tetapi pada masa yang sama telah mencetuskan peningkatan yang ketara dalam ketelusan dielektrik,ε dalam komposit nano. Analisis Spektroskopi Impedans (IS) menunjukkan kebergantungan kekerapan yang tinggi terhadap konduktiviti arus ulang alik, σ_{ac} dan ketelusan dielektrik, ε' komposit nano pada julat kekerapan rendah dari 100 Hz to 1MHz. Nilai maksimum σ_{ac} adalah $4.0\text{x}10^{-5}$ S/m dan ε' pada sekitar 600 untuk komposit nano yang mengandungi 1.0% berat AgNP. Analisis FESEM mendedahkan bahawa taburan secara rawak MWNT yang tertanam di dalam matrik PVA dengan permukaan sempadan yang tidak teratur boleh bertindak sebagai penghubung konduktif apabila bersentuhan dengan AgNP. Purata saiz zarah AgNP ditemui dalam julat antara 17nm hingga 55nm. Di samping itu, hasil analysis UV mengaitkan hasil penemuan yang lain dengan penyerapan cahaya yang boleh dilihat dengan proses perpindahan cas antara bahan pengisi dan matrik. Penilaian selanjutnya oleh Analisis Rangkaian Vektor (VNA) menilai sifat-sifat elektromagnetik komposit nano pada kekerapan yang lebih tinggi iaitu 8 hingga 12 GHz (X-band). Dalam peringkat ini, nilai ε' komposit nano mengandungi 1.0% berat AgNP kekal stabil pada 25 pada julat kekerapan X-band, sementara ketelapan,μ menghampiri nilai 0.5 disebabkan kerentanan yang rendah oleh komposit nano dengan medan magnet. Kedua-dua sifat ini mempengaruhi keupayaan komposit nano untuk mengurangkan jumlah gelombang elektromagnetik yang dihantar. Ini disebabkan oleh penyerapan gelombang yang lebih tinggi berbanding tingkah laku pantulan komposit nano dengan peningkatan permukaan sempadan dielektrik-AgNP. Secara keseluruhannya, PVA / MWNT-AgNP memberi jaminan bagi menghasilkan bahan-bahan ketelusan yang tinggi dengan penyerapan elektromagnetik yang baik. Oleh yang demikian, PVA / MWNT-AgNP komposit nano boleh memberikan potensi besar dalam aplikasi elektronik seperti penyimpanan tenaga tinggi, dan bahan penyerapan gelombang dielektrik pada kekerapan yang tinggi.

ACKNOWLEDGEMENTS

Thanks to Allah for His Great Blessing and Solawat to our beloved Prophet Mohammad (P.B.U.H) and again foremost, praise to God Almighty, Allah S.W.T for His blessing and guidance for me to complete this research. It is a pleasure to convey my gratitude in my humble acknowledgement to a great number of people who contributed in various ways throughout this research. In the first place I would like to convey my greatest thankfulness to my supervisor, Prof. Mohd Rafie Johan who has helped a lot in giving full support, guidance, advice, suggestion, and encouragement to me from the very early stage of this research till I could manage to complete this thesis. My deepest gratitude goes to my family members, my lovely parents, my brother and sister, and not forgetting to both of my sons, for their non-stop moral support and encouragement in my study. Special acknowledgement to the laboratories and facilities that I have used throughout my research at Faculty of Engineering, University of Malaya (UM), Nanotechnology & Catalysis Research Centre (NANOCAT), UM, and Institute of Advanced Technology (ITMA), University Putra Malaysa (UPM). I am also grateful toward all lab technicians who have assisted me with their kindness and tolerance in doing my experimental works. I also would like to extend my appreciation to my colleagues in Nanomaterial Engineering Research Group (NERG) for providing me a conducive atmosphere to conduct my research. Thank you again to all. Last but not least, I would like to give my sincere gratitude to all people who were involved either directly or indirectly in helping me throughout this project.

TABLE OF CONTENTS

LIST OF FIGURES

LIST OF TABLES

LIST OF SYMBOLS AND ABBREVIATIONS

Symbol	Description
ε'	Dielectric permittivity
σ_{ac}	ac Conductivity
μ	Permeability
A	Absorbance
a	Each crystal structure
A	Film area
ac	Alternating current
Ag^+	Silver ions
$AgNO_3$	Silver nitrate
AgNP	Silver nanoparticles
C_o	Capacitance of the two electrode plates without sample
CTC	Charge transfer complexes
d	Crystalline lattice spacing
D	Crystallite size
d	Thickness
DMF	Dimethylformamide
EDX	Energy dispersive X-ray
EMI	Electromagnetic interference
f	Content of conductive fillers
f	Measuring frequency,
f_c	Percolation threshold

FESEM	Field emission scanning electron microscopy
FTIR	Fourier transform infrared
H_2O_2	Hydrogen peroxide
HNO_3	Nitric acid
I	Transmitted light intensity
ICP-OES	Inductive coupled plasma-optical emission spectrometer
I_D	Intensity of D-band
I_G	Intensity of G-band
I_o	Incident light intensity.
IS	Impedance spectroscopy
I-V	Current–Voltage
K	Shape factor
LSV	Linear sweep voltammetry
M'	Real part of dielectric modulus
M''	Imaginary part of dielectric modulus
M^*	Complex dielectric modulus
MWNT	Multi-walled carbon nanotubes
n	Integer for crystalline planes
PTFE	Polytetrafluoroethylene
PVA	Polyvinyl alcohol
q	Dielectric exponent of insulating region
Rpm	Revolutions per minute
SDS	Sodium dodecyl sulphate
SPR	Surface plasmon resonance

t	Critical exponent of conducting region
T	Transmittance
TEM	Transmission electron microscope
TGA	Thermogravimetric analyzer
UV-Vis	Ultraviolet-visible analysis
VNA	Vector network analyzer
wt	Weight
XRD	X-ray diffractometer
β	Peak broadening at half-maximum intensity in radians
ε''	Dielectric loss
ε_o	Permittivity of the free space
θ	Diffraction angle of incidence rays
λ	Wavelength
φ	Phase angle

CHAPTER 1 : INTRODUCTION

This chapter describes the background, objectives, scope and limitation, as well as the significant of research in this work.

1.1 Research background

The development of polymer nanocomposites is based on the combination of one or more nano-sized fillers with various shape (e.g. fiber, spheroid, nanotubes and nanoparticles) dispersed in continuous polymer matrix. The evolution from micro to nanostructured materials as the building blocks in composite materials lead to fascinating changes in physical and chemical properties due to high aspect ratio of surface area to volume. The interaction amongst fillers and the matrix increases as the particles size get smaller, thus improving the strength, heat resistance and conductivity of the materials.

Carbon nanotubes (CNT) has received wide attention from many researchers since Iijima discovered it in 1991 (Iijima, 1991). Distinct from other carbon materials like graphite or diamond, the CNT is a 1-dimensional structure with high aspect ratio. CNT is known as an excellent conductive filler since it allows motion of the electrical carriers along one controllable direction (Lu et al., 2011). The interest in CNT has triggered its derivative materials for multi-functional applications. In recent years, advanced polymer nanocomposites are prompting hybrid fillers of CNT and metal nanoparticles in order to impart unique mixing characteristics from both nanostructured materials. The hybrid fillers can promote multi-functionalities of polymer composites for various purpose including catalytic, optical, electronic and magnetic applications (Sahoo et al., 2010; Lu et al., 2011).

Meanwhile, high permittivity of polymer matrix composites (PMC) have triggered important needs for passive component in electrical/electronic fields. These materials are used in polarizable media such as embedded capacitors, piezoelectric transducers, amplifiers, and memory elements (Ahmad, 2012). Generally, the high permittivity materials is able to store more electric energy than the lower permittivity. However, traditional dielectric materials developed from ceramic materials such as mica and SiO_2 has exhibited high-ε properties with excellent thermal stability. On the other hand, PMC has some advantages over the conventional ceramic dielectric materials because it can combine the dielectric properties of the fillers with the polymer matrix to offer a low temperature processing, good formability and adhesion strength.

This thesis discuss the significance of integrating multi-walled carbon nanotubes/silver nanoparticles (MWNT-AgNP) reinforced polyvinyl alcohol (PVA) nanocomposites as high permittivity materials. The properties of PVA/MWNT-AgNP nanocomposites are investigated thoroughly in terms of morphology, structure properties, thermal stability, electrical and dielectric properties as well as their electromagnetic properties.

1.2 Problem statements

The massive growth in electronic industry has raised the interest in high permittivity (high-ε) materials that able to store high electric energy. The key problem of conventional dielectric materials arise from the challenging fabrication process of silica /ceramic based materials that involves large energy consumption due to high sintering temperature (>500°C) and their brittleness. Meanwhile, the use of polymer composites filled with inorganic/ceramic fillers at high concentration of (>50 vol%) have degraded the processing and flexibility of the polymers (Dang et al., 2012).

The innovation of carbon nanotubes (CNT) filled polymer composites would be promising as an alternative approach for the high-ε applications with better performance and lightweight material. Apart from the excellent electrical conductivity of CNT, it contributes a significant increase in dielectric permittivity due to large surface area and high aspect ratio of the fillers. However, the use of CNT at certain amount causes poor processability of the polymer due to high accumulation of the CNT initiated by van der Waals forces. Therefore, there is an interest of integrating CNT-AgNP in polymer composites to attain good electrical conductivity at much lower percolation threshold (Liang et al., 2007; Zhang et al., 2010; Xin & Li, 2011; Saini et al., 2013).

To date, not much work has reported about the significance of CNT-AgNP as the conductive fillers to induce high-ε polymer composites. It has been reported that CNT/polymer nanocomposites have shown a parallel trend of the dielectric permittivity and dielectric loss due to their high surface area to volume ratio (Zhang et al., 2009; Dang et al., 2012). Zhen et al., (2013) has reported the low frequency dependence of dielectric permittivity of polymer nanocomposites with CNT less than 5 wt%. Whereas few studies are focusing on lowering dielectric loss of polymer nanocomposites triggered by of AgNP in Coulomb Blockade effect of single nanoparticles (Lu et al., 2005; Lu et al., 2006). Recently, the effective used of metallic nanoparticles for absorption of electromagnetic wave at the metal–dielectric interface was reported at very high frequency (Zhao et al., 2010; Melvin et al., 2014, 2015).

However, the broad applications of polymer composites are still limited because many polymers are almost transparent to electromagnetic waves. These composites are not able to block electromagnetic radiation that common exists in the environment, including the radio waves, microwaves and X-rays. Thus, it requires further modification in order to take advantage of their lightness, low cost and easy shaping of the polymer.

This study aim to attain high permittivity materials in a three-phase composite system that comprised of MWNT-AgNP reinforced polyvinyl alcohol (PVA) matrix. MWNT is chosen in this work because it has better performance to price ratio (PPR) compared to single wall carbon nanotubes (SWNT) for large-scale productions and low cost. PVA is a good dielectric host matrix due to high density of hydroxyl groups for encapsulating MWNT and nanoparticles as well. The different in electrical conductivity between MWNT and AgNP can create high interfacial polarizations within the dielectric medium to induce a parallel increase in dielectric permittivity and electrical conductivity. This may also contribute to electromagnetic properties of the materials.

1.3 Research objectives

This thesis principally focuses on the preparation and characterization of PVA filled with MWNT-AgNP as the hybrid conductive fillers. In light of this purpose, this work intends to explore the influence of AgNP hybridizing MWNT on the properties of PVA nanocomposites. The research work aims to address the following objectives as below:

i. To synthesize MWNT-AgNP and PVA/MWNT-AgNP nanocomposites at various AgNP contents.

ii. To characterize morphology, structural and thermal properties of the synthesized nanocomposites.

iii. To study electrical, dielectric and electromagnetic properties of the synthesized nanocomposites.

iv. To determine the optimum composition of the nanocomposites as high permittivity materials.

1.4 Scope of works

The scope of this works is synthesizing and characterizing of (a) MWNT-AgNP hybrid and (b) MWNT-AgNP filled PVA nanocomposites. Firstly, MWNT is functionalized through mild oxidation treatment by ultrasonication of the MWNT in nitric acid (HNO_3) followed by hidrogen peroxide (H_2O_2). Afterward, MWNT-AgNP are produced with different volume of $AgNO_3$ via a single chemical route by reducing silver ions (Ag^+) from an aqueous silver nitrate ($AgNO_3$) in MWNT solution, which assisted with sodium dodecyl sulphate (SDS) as surfactant. Structural properties of the synthesized MWNT-AgNP powder are characterized by Raman spectroscopy and Fourier transform infrared (FTIR). Morphological properties are carried out by Field emission scanning microscopy (FESEM) and transmission electron microscopy (TEM). Secondly, the synthesized MWNT-AgNP are mixed with PVA matrix by solution mixing, and casted into glass Petri dishes to obtain PVA/MWNT-AgNP nanocomposite films. Secondly, the properties of MWNT-AgNP reinforced PVA nanocomposites are evaluated with regard to the different AgNP contents (0.1, 0.3, 1.0 and 1.8 wt%). The concentration of AgNP are determined by using inductive coupled plasma-optical emission spectrometer (ICP-OES). The structural and morphology properties of the nanocomposites are characterized by X-ray diffraction (XRD), FTIR and FESEM, respectively. Electrical conductivity and dielectric properties of the nanocomposites are evaluated by using Impedance Spectroscopy at low frequency range from 100Hz to 1 MHz. While electromagnetic properties of the nanocomposites are characterized by using Vector Network Analyzer at X-band frequency from 8 GHz to12 GHz.

1.5 Significant of research

This research highlight the importance of integrating high permittivity materials from the combination of MWNT-AgNP reinforced PVA nanocomposites. In this work, the MWNT-AgNP was synthesized via a single route chemical reduction of silver nitrate, prior to the fabrication of PVA nanocomposites by solution mixing and casting technique. This approach is simple, low-cost and effective for small-scale fabrication. Another improvement in this work is by introducing mild oxidation treatment for the attachment of AgNP on MWNT surface, which assisted by the used of surfactant, SDS. This approach could minimize severe damage on the nanotube structures and care electrical properties of the MWNT. It is significant to have a good understanding of the synthesized nanocomposites in terms of morphological, structural, thermal, electrical and dielectric properties. The findings demonstrate that the inclusion of MWNT-AgNP not only improves the electrical conductivity, but also triggers a significant increase in dielectric permittivity of PVA nanocomposites. This study also have shown good correlation between high permittivity and electromagnetic properties of the nanocomposites. The great implication of this work is to develop high permittivity of PVA/MWNT-AgNP nanocomposites with weak frequency dependence special at microwave frequency. This is desirable for the design of high dielectric-absorbing materials. Apart from this, it can increase reliability of lightweight and flexible materials for electronic devices in high-frequency applications.

1.6 Thesis outline

The thesis outline describes an overall structure of the writing, which is comprised of five main chapters. Chapter 1 covers the introduction in general context of CNT-AgNP based polymer composites with some related issues, in order to define the purposes and significance of this work. Next, chapter 2 address the information already exist in this research field, the key ideas relate to the theory of dielectric permittivity and analytically review most relevant literatures based on others work. Chapter 3 defines all the materials and synthesis methods, including sample preparation for different characterization techniques. Chapter 4 subsequently elaborates results and discussion based on the experimental data or figures presented in this section. Finally, chapter 5 provides a brief conclusion of the research findings and some recommendations for future works.

CHAPTER 2 : LITERATURE REVIEW

This chapter covers a general review of the relevant literatures in this field. It discuss the subject matter by providing main ideas, theories and seminal works from previous studies with the current-state of knowledge.

2.1 Conductive filler/polymer composites

As advanced technologies are growing, conductive filler/polymer composites have been explored progressively in many research works. The composites are typically consist of an insulating polymer matrix and dispersed network of conductive fillers, which allow electrical current flow through the polymeric material. The efforts has focused to combine the advantages of both polymer and fillers that can produce composites with high conductivity, good processability, lightweight, low density, corrosion resistance and enhanced mechanical properties (Thongruang et al., 2002; Grossiord et al., 2008).

The development of conductive fillers/polymer has to be sought for a low percolation threshold concentration (PTC) and high electrical conductivity. The polymer composites have been formulated using conductive fillers such as graphite, carbon black, carbon fibres, metallic particles, intrinsically conductive polymer and currently carbon nanotubes (Rybak et al., 2010). The percolation and conductivity of polymer nanocomposites depend greatly on the shape, content and dispersion of the fillers , their degree of orientation and bundling, thermodynamic interactions between the polymer matrix and the fillers, the interaction between the filler particles themselves, as well as the processing conditions (Thongruang et al., 2002; Grossiord et al., 2008).

Electrically conducting polymer composites with volume conductivity higher than 10^{-10} S/cm are categorized as relatively inexpensive materials for multifunctional applications (Ma et al., 2010). Examples of conductive polymer composites in applications such as battery and fuel cell electrodes, electrically conducting adhesives, antistatic coatings and films, corrosion-resistant materials, electromagnetic interference shielding and so forth. These conductive composites are possibly preferred to replace metals or semiconductors in suitable applications as shown in Figure. 2.1.

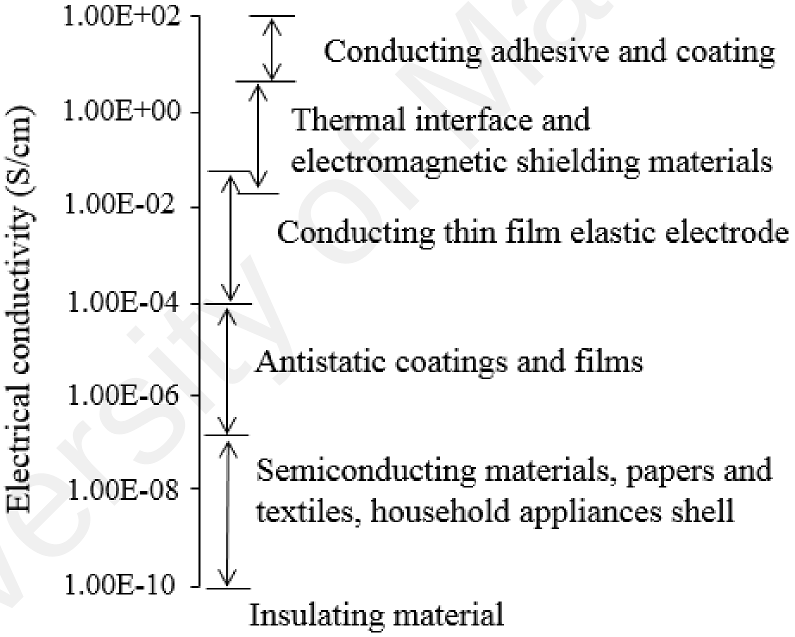

Figure 2.1: Typical applications of conductive composites (Ma et al., 2010).

2.1.1 Polyvinyl alcohol (PVA)

PVA is a water-soluble synthetic polymer that made from transesterification of polyvinyl acetate to polyvinyl alcohol. The residual contents of acetyl groups after a final hydrolysis step determines degree of hydrolysis in most PVA products. PVA chemical formula is $[CH_2CH(OH)]_n$ and its structure is given in Figure 2.2. It is an atactic polymer that exhibits irregular stereochemical configuration which mainly consist of 1,3 diol units and a few of 1,2 diols units, depending on the polymerization conditions (Hallensleben, 2000). PVA is a semi-crystalline polymer and the crystalline domains depends on its hydrolysis degree. A high hydrolysis degree corresponds to low acetyl contents and leads to a higher crystallinity of the polymer. PVA is a polar polymer and is good as dielectric host due to its high content of hydroxyl groups. Hydroxyl groups are strong permanent dipoles that can align with the electric field to increase polarization (Kulshrestha et al., 2014; Van et al., 2014).

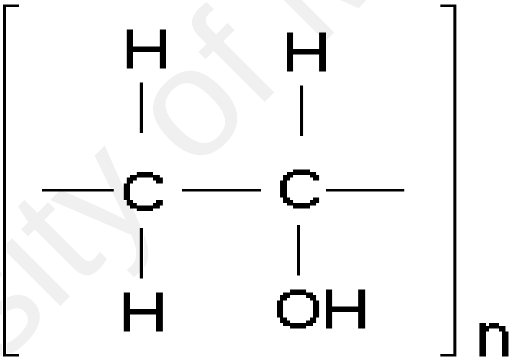

Figure 2.2: Chemical structure of PVA.

The structure properties of PVA depends on the hydrolysis degree and its final molecular weight. The melting point of fully hydrolyzed PVA is at 230 °C and for the partially hydrolyzed degree is in the range of 180-190 °C. It has good mechanical strength and flexibility, as well as high oxygen and moisture resistance properties (Mercader, Poulin, & Zakri, 2010). PVA is water-soluble at elevated temperature due to its hydrophilic nature and the presence of hydroxyl groups. The solubility rate increases with decreasing hydrolysis degree of the polymer. PVA a non-toxic and it is recognized among few vinyl polymers that biodegrades slowly. It is susceptible for biodegradation in the presence of suitably acclimated microorganisms (Chiellini et al, 2003). PVA is found in wide applications such as textiles, papermaking, adhesives, coating and special applications due to its biocompatibility, good processability, film forming and adhesive properties.

Table 2.1: Physical properties of PVA.

Chemical formula	[-CH_2CHOH-]n
Melting point (partial hydrolyzed)	200 °C (392 °F; 473 K)
Density	1.19-1.31 g/cm^3
Strength	1.6 ± 0.1 GPa
Elastic modulus	48 ± 3 GPa
Refractive index(n_d)	1.477

2.1.2 Multi-walled carbon nanotubes

Since the discovery of carbon nanotubes (CNT) by Iijima (1991), great works have been made in the area of nanoscale carbon materials due to their unique mechanical, electrical and thermal properties (Sahoo et al., 2010). CNT possess high aspect ratio more than 1000 because of large length (up to several microns) to small diameter (a few nanometers). CNT can be classified into single-walled nanotubes (SWNT) and multi-walled nanotubes (MWNT). SWNT consist of single sheet of graphene rolled seamlessly to form a cylindrical with diameter of order 1 nm and length of up to cm. MWNT consist of an array of such cylinder formed concentrically and separated by 0.35 nm, similar to the basal plane separation in graphite (Iijima, 1991). MWNT can have diameters from 2 to 100 nm and lengths of tens of microns. The geometric structures of SWNT and MWNT are shown in Figure 2.3.

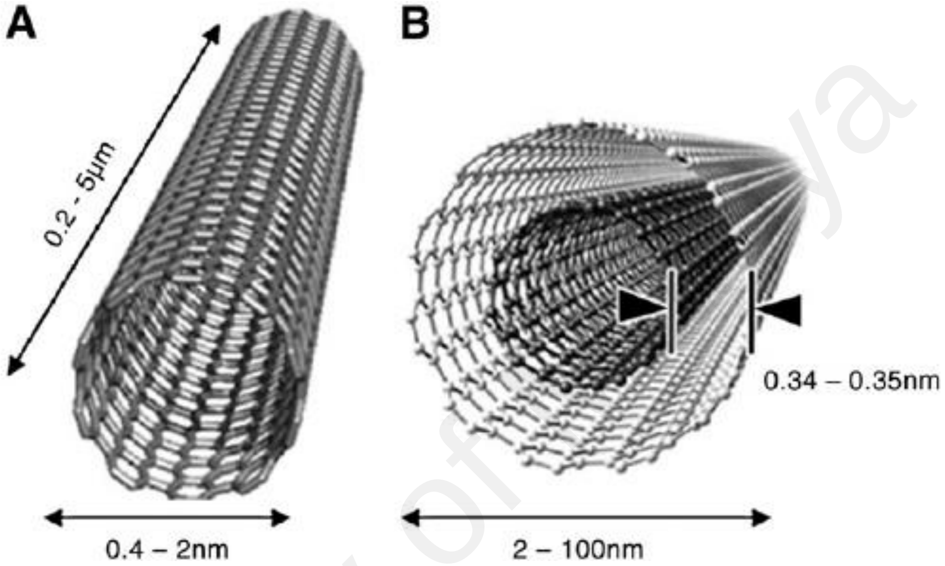

Figure 2.3: Schematic illustration of (A) single-walled carbon nanotube (SWNT) and (B) multiwalled carbon nanotube (MWNT) (Reilly, 2007).

In this study, MWNT has drawn special attention because it consist of several coaxially SWNT nested each other with interlayer distances similar to the graphite. The larger diameter of MWNT allows a better study for quantum interference phenomena in a magnetic field such as Aharonov-Bohm effect (Forro, 2001). One main benefit of MWNT is that the multi-walled configuration offer good stability upon chemical functionalization on the tube walls without deteriorating the internal tubes. MWNT also has better performance to price ratio (PPR) as compared to SWNT for large-scale productions. Nowadays, MWNT can be grown with or without magnetic catalytic particles via chemical vapor deposition (CVD) technique at a much lower temperature (700-950°C) than the arc arc-discharge process (Lehman et al., 2011).

2.1.2.1 Structure and electronic properties

In general, the structure properties of CNT are influenced by their one-dimensional (1-D) characters. According to Meyyapan (2009), chemical reactivity of CNT are related to the pi-orbital mismatch caused by an increased curvature. For the same reason, a smaller nanotube diameter results in an increased reactivity. Covalent chemical modification of either sidewalls or end caps has shown to be possible. For example, the solubility of CNT in different solvents can be controlled in this way. Therefore, it is expected that other physical properties are influenced by these parameters. The CNT as a whole is very flexible because of the great length and have a very large Young modulus in their axial direction. The nanotubes mechanical properties are extremely strong, stiff, and relatively ductile, which can be bent and stretched into shapes without catastrophic failure. Each single-walled nanotube has tensile strengths range between 50 and 200 GPa (approximately magnitude greater than carbon fibers); this is the strongest materials known materials. The Young's Modulus is about one tetrapascal [TPa (1 TPa = 10^3 GPa)], while fracture strains in between 5% and 20%, and has relatively low densities (Smalley, 2003).

CNT also have a unique electronic properties that change significantly with the chiral vector, **C** = (n, m) that defines on how a graphene sheet is rolled to form the carbon nanotube structure. CNT can show metallic or semiconducting behavior depending on the chirality. According to the rolling angle of the graphene sheet, CNT have three chiralities: armchair, zigzag, and chiral one. The tube chirality is defined by the chiral vector, $C_h = na_1 + ma_2$ (Figure 2.4), where the integers (n, m) are the number of steps along the unit vectors (a_1 and a_2) of the hexagonal lattice (Ma et al., 2010). Metallic CNT behave as long ballistic quantum conductor with the charge carriers, exhibiting a large phase coherence. It exhibits the strongest electrochemical properties possibly because the lower resistance allows a greater double layer charge buildup. It means that the characteristics length of electron motion is suppressed, leading to quantization effects on electrical conductivity. Individual tubes can conduct electron with coherence lengths of several microns and carry the highest current density of known material (Inpil et al., 2006).

In this respect, the electrical and electronic properties of MWNT is an exciting field of research. Even one may think that MWNT do not qualify as 1-D conductor, but their large diameter could favor low-ohmic contact because the electric current induced into the outermost of nanotube is somewhat similar to large diameter of SWNT (Forro, 2001).

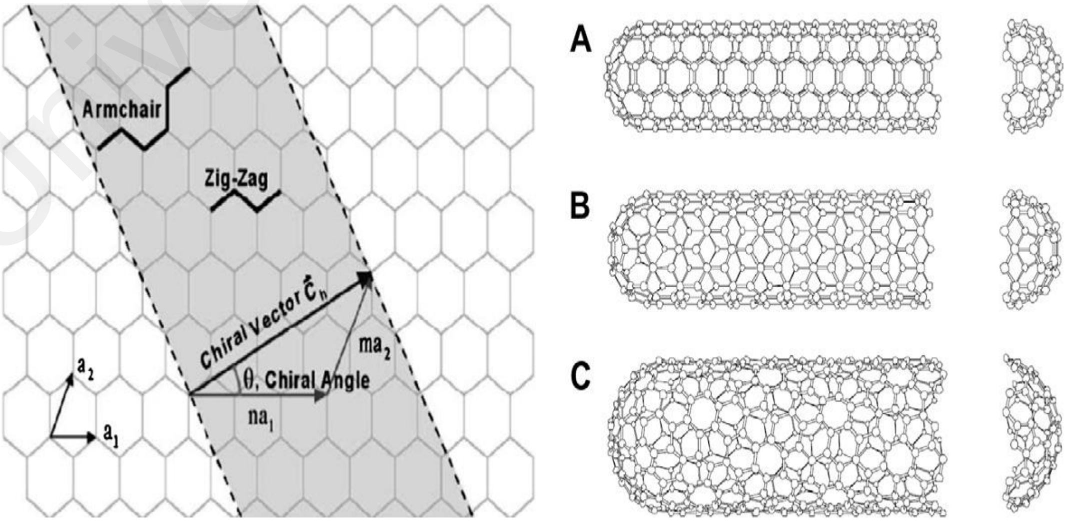

Figure 2.4: Schematic structure of CNT with different chirality: a) armchair structure b) zigzag structure c) chiral structure (Ma et al., 2010).

2.1.3 Silver nanoparticles

The interest in nanotechnology has been devoted to metallic nanoparticles with a diameter size of less than 100nm. Silver nanoparticles (AgNP) are amongst noble metals that exhibit unique optical, electrical and thermal properties significantly distinct from their bulk counterparts due to large surface area and quantum confinement effects. These unique properties are influenced by the shape and size distribution of AgNP, depending on the synthesis methods, reducing agent and stabilizers (Pastoriza & Liz, 1999). Figure 2.5 shows TEM image of spherical AgNP.

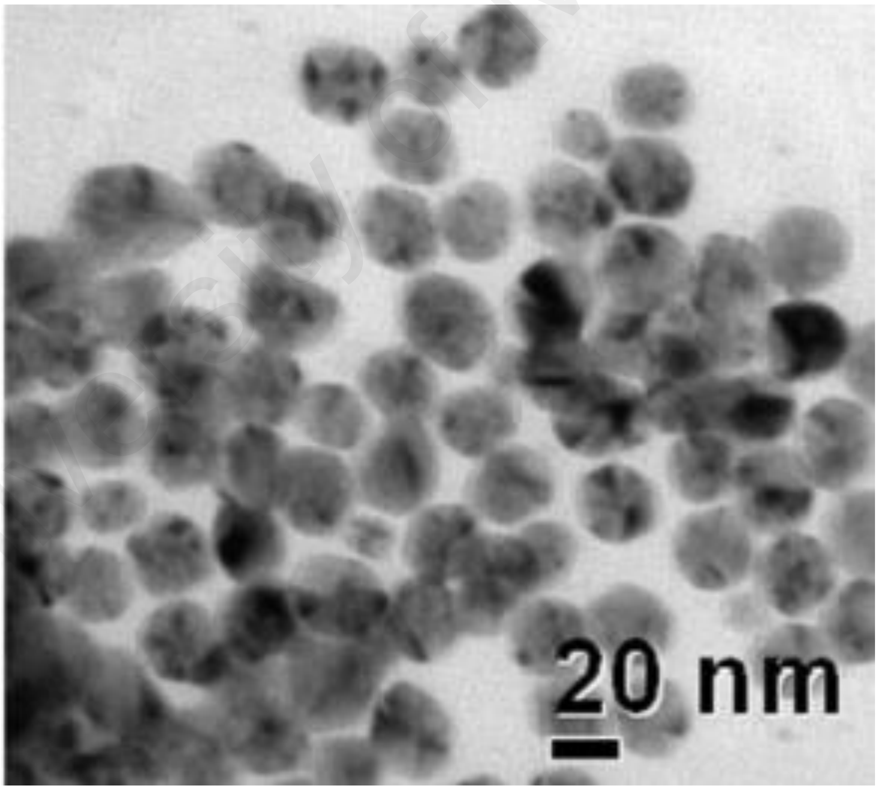

Figure 2.5: TEM image of silver nanoparticles (Bhui et al., 2009).

There are two common routes of synthesizing AgNP. The first one is a physical approach that utilizes evaporation/condensation technique. The source material placed in a boat centered at a tube furnace is vaporized under atmospheric pressure into a carrier gas. AgNP also synthesized with laser ablation of metallic bulk materials in solution. The second one is a chemical approach in which the metal ions (Ag^+) reduced in aqueous solution of water or organic solvents. Chemical reduction method frequently used to yield stable colloidal silver with particle size of several nanometer. The reductants commonly used are borohydride, citrate, ascorbate and elemental hydrogen (Kholoud et al., 2010). An environmental friendly approach also has been applied to synthesis AgNP by the use of native plant or fruit extract and bio-organisms. These green methods are safe, low cost, fast and efficient ways to produce crystalline nanoparticles with variety of shapes (Kouvaris et al., 2012).

2.1.3.1 Optical and electrical properties

The intense study in unique optical behavior of AgNP arises due to quantum size and effective plasmon resonance when the nanoparticles are irradiated by oscillating electric field (Figure 2.6). The interaction of light and spherical nanoparticles causes the displacement of free conduction electrons coherently oscillate with the electric field (Kelly et al., 2003). In these regards, AgNP have attracted great interest in various applications such as surface plasmon effects, photonics, surface enhanced Raman scattering, catalysis, and data storage (Gupta et al., 2010; Kholoud et al., 2010), as well as in medical sector for diagnosis, anti-microbial and drug delivery (Kouvaris et al., 2012).

The electrical conductivity of AgNP distinct from their counterparts when the energy levels become discrete, rather than continuous as the size of the metal is reduced to nanometer scale. The discrete spacing between energy levels known as Kubo gap ($\delta = 4E_f/3N$) is dependence on Fermi energy of the metal E_f, and number of atoms in the clusters, N (Siwach & Sen, 2008). As the size of the nanoparticle increases, the spacing between energy levels is diminished. At low temperature, the nanoparticle behaves like an insulator because the Kubo gap is significant. The conductivity will be the same as in bulk metal when the thermal energy is greater than this gap.

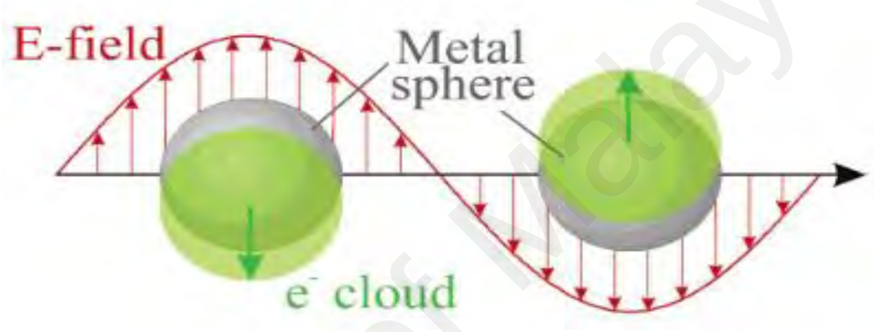

Figure 2.6: The plasmon oscillation in spherical nanoparticles (Kelly et al., 2003)

2.2 Formation of hybrid carbon nanotube-silver nanoparticles

Numerous researches have reported different techniques of synthesizing carbon nanotubes-silver nanoparticles (CNT-AgNP) hybrid. Generally, the structure and reactivity of CNT surface can serve as metal template for nanoparticles growth. The formation of AgNP deposited on CNT surface may involve the reduction of silver salt via dry or wet chemistry techniques. There are various techniques used in the literatures such as impregnation (Planeix et al, 1994), electroless metal plating (Wang et al., 2004), self-assembly (Ellis et al., 2003), electrodeposition (Quinn et al. 2005), physical vapor deposition (Zhang et al. 2000), and '*in situ*' photochemical reduction method (Zhao et al. 2010).

Another common method of depositing AgNP on the CNT surface is via the wet chemical reduction that requires reduction agents such as ammonia, formaldehyde, N,N-dimethylformamide (DMF) and alcohols (Liu et al., 2006, Georgakilas et al., 2007, Alimohammadi, Parvinzadeh, & Shamei, 2012). Although, it is still challenging to synthesize CNT-AgNP via "in-situ" reduction techniques because only some AgNP could deposit onto the CNT surface (Ahmadpoor, Zebarjad, & Janghorban, 2013). Therefore, surface modification of CNT through functionalization is required to promote active groups on sidewalls of the nanotubes while improving hydrophobic nature and aggregation of high CNT content in polymer matrices. However, strong oxidation treatments at elevated temperature can cause severe structural damage and fragment CNT into shorter length with reduced aspect ratios. It is unfavorable for the formation of conductive polymer composites because it hinders electrical flow of the nanotubes itself (Du, Bai, & Cheng, 2007; Ahmed, Haider, & Mohammad, 2013). In this regards, few researches have conducted mild oxidation treatment to functionalize the surfaces of CNT at relatively low temperature while minimizing nanotube damage. For example, the oxidation treatment using HNO_3 and H_2O_2 still could promote the functional groups (-OH, C=O, -COOH) on the nanotube surfaces (Aville et al.,2009; Ahmed et al., 2013).

Apart from the chemical oxidation treatment, another methods was proposed via a substrate enhanced electroless deposition (SEED) process. It is favorable for depositing metal particles with lower redox potentials than that of CNT such as Cu and AgNP (Qu & Dai, 2005). Sahoo et al. (2011) conducted a method for depositing different densities of AgNPs on the CNT network by catalyst-free technique. This approach is an alternative to the electrodeposition process that commonly needs the use of chemicals and/or catalysts.

2.3 Fabrication methods of CNT/polymer nanocomposites

The performance of CNT in polymer matrix depends on the dispersion of CNT and interfacial interactions between the CNT and the polymer. Several factors including polymer matrix viscosity, moulding temperature and processing time influences the performance of a conductive network (Deng et al., 2009). The mixing of CNT based fillers with various polymer matrices, including thermoplastic, thermosets and elastomers are commonly processed by different fabrication methods as below (Vaisman et al., 2006; Ma et al., 2010):

i. 'In-situ' polymerization technique

In-situ polymerization is an efficient method to prepare uniform dispersion of CNT in a thermosetting polymer. The CNT dispersion are mixed with monomers, either in the presence or in absence of a solvent. Then theses monomers polymerized via addition with a hardener or curing agents at an elevated temperature. The advantages of this method is that covalent bonding formed between the functionalized CNT and polymer matrix.

ii. Coagulation

This technique begin with a carbon nanotube-polymer suspension in which carbon nanotubes have been well dispersed by sonication and the poured into excess of a non-solvent, causing the polymer to precipitate and entrap the nanotubes bundles. This precipitation process is rapid, so the carbon nanotube apparently do not aggregate or combine during the coagulation process and provides better nanotube dispersion. The advantage by using this technique is produced uniform nanotube-based composite.

iii. Solution/solvent Casting

In this technique involves preparing a suspension of nanotubes in a polymer solution. Then, allowing the solvent to evaporate in order to produce nanotube-polymer nanocomposites. The problem in this technique is the nanotubes tend to agglomerate during solvent evaporation, which leads to inhomogeneous nanotube distribution in polymer matrix. In some cases, solution mixing could achieve better state of CNT dispersion than melt mixing.

iv. Melt Mixing

This technique commonly applicable to thermoplastic polymers as the matrix materials. It does not require solvent to disperse the CNT but it uses a high temperature and high shear forces to disrupt the nanotube bundles. The problem is it is not provide uniform nanotube dispersion. It is need subsequent processing step called passing using special equipment such as extruder, and injection molding.

v. Latex technology

This is a relatively new method to incorporate CNT in most polymers produced by emulsion polymerization. The CNT are initially dispersed in an aqueous surfactant before mixing with a polymer latex. Latex is a colloidal dispersion of discrete polymer particles in aqueous medium. The process is relatively easy, cost-effective, reliable and safe for large-scale fabrication technique.

2.4 Overview of the related previous works

In many literatures, CNT-AgNP have been used as the conductive fillers to prepare polypropylene (PP) (Liang et al, 2007) , polystyrene (PS) (Xin and Li, 2011) and epoxy

(Ma, Tang and Kim, 2008) nanocomposites by melt compounding and solution mixing. Their results found that CNT-AgNP could significantly enhance the electrical conductivity and mechanical properties of nanocomposites compared to pristine CNT. Xin and Li (2011) confirmed that PP and PS containing CNT-AgNP could decrease the percolation threshold for electrical conductivity. It was found that CNT-AgNP filled nanocomposites, which are prepared by solution mixing could avoid oxidation of the AgNP and has better electrical properties. This is because of AgNP and help to improve dispersion of CNT in the polymer matrix because of the reduced surface energy and van Waals forces between CNT.

Alimohammadi et al. (2012) also highlighted that silver deposited MWNTs surfaces could reflect a high portion of radiation at UV region due to the light scattering of larger nanoparticles or aggregation of modified MWNTs. Therefore, CNT-AgNP mostly appropriate to increase the UV reflection properties of materials in various polymeric nanocomposites and coatings applications. Fortunati et al. (2011) fabricated CNT-AgNP with a biodegradable polymer, poly (ε-caprolactone) (PCL) by solvent cast technique. The results found antimicrobial effects of AgNP on various bacteria that can encourage its application as conductive antimicrobial nanostructures. This because AgNP could act as conductive bridges among nanotube bundles and facilitate electron transfer that help to facilitate the formation of conductive pathways.

Most recent, Zhang et al. (2016) investigated surface-enhanced Raman scattering (SERS) activities of CNT decorated with AgNP produced via a simple citrate reduction method. They conducted a time-course SERS mapping to study the evaporation process of probe molecules and simulated the electromagnetic field distribution by the finite difference time domain (FDTD) method. Another researcher has found a significant electronic enhancement of specific capacity for CNT/bone charcoal composite was increased by twice with incorporation of only 0.8 wt.% of Ag NP decoration (Matsubara et al., 2016).

The latest trends of CNT-AgNP and PVA composites are emphasizing on electrical and dielectric properties of the materials. Alghunaim et al. (2016) did the optimization and spectroscopic studies of CNT/PVA nanocomposites at high frequency. The behavior of both dielectric constant and dielectric loss were reported decrease as the frequency increases when the dipole direction in PVA oriented toward the applied field. Meanwhile, Amrin & Deshpande (2016) reported the dielectric relaxation and ac conductivity behavior of carboxyl functionalized CNT/PVA nanocomposite in frequency range of 0.1 Hz–1 MHz. The increment in electrical conductivity was analyzed a Jonscher power law to show the dominant charge transport mechanism in the nanocomposite.

Currently, the advanced study of MWNT-AgNP and its composites have been given attention to electromagnetic applications. In previous work, the effective used of integrating CNT-AgNP was reported for the absorption of electromagnetic wave at the metal–dielectric interface at very high frequency (Zhao et al., 2010; Melvin et al., 2014; Melvin et al., 2015). However, the microwave-absorption properties can be altered by controlling heat-treatment temperature and time. These factors may change the defect and surface organic groups on CNT surfaces (Zhang et al., 2017). Besides that Wang et al. (2018) have study on Terahertz (THz) dispersion characteristics of super-aligned CNT. They measured the enhanced transmission spectra with THz incident wave through subwavelength apertures to retrieve the refractive index, effective permittivity, and conductivity of the materials (Wang et al., 2018).

2.5 High permittivity materials

The history of permittivity dates back to the 18th century and arises from electronic polarization of molecules and atoms when exerted under an external electric field. Permittivity is expressing charge storage capability and is defined by Maxwell's equations over many molecules (Baker, 2010). The term high permittivity (ε) refers to materials with high dielectric constant as compared to the conventionally used silicon based devices. The ε value of any materials greater than silicon nitride (ε > 7) are categorized as high permittivity, while those with ε value smaller than silicon dioxide (ε< 4) are categorized as low permittivity materials. Table 2.3 listed the high-ε materials that widely found in electronic industries such as memory cell dielectrics, gate dielectrics, and capacitors (Singh & Ulrich, 1999). A statistic shows rapid growth in electronic industry has fascinated great interest for passive electronic components as reported in Figure 2.7.

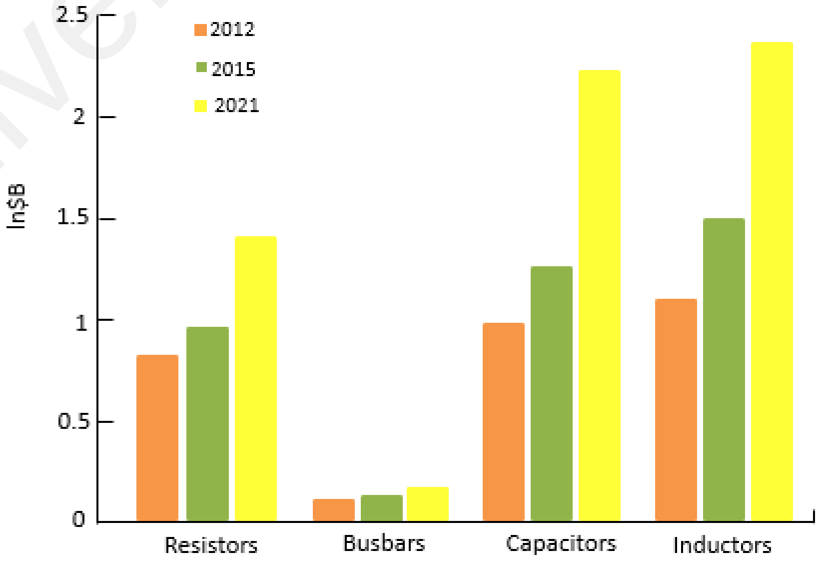

Figure 2.7: Shows the market trend of passive components in Europe and Asia (*Inverter Technology, Trends and Market Expectations report*, 2016).

Table 2.1: Some important permittivity materials and the applications (Singh & Ulrich, 1999).

	Dielectric Constant	Application
$PbMgNbO_3$+$PbTiO_3$	22,600	B
$PbLaZrTiO_3$	1000	B
$BaSrTiO_3$	300	B
TiO_2	50	A,C
Ta_2O_5	25	A,B
CeO_2	20	A
$BaZrTiO_3$	17.3	E
Al_2O_3	9	B
(Bz,Ca,Sr)F_2	7.3	D

A: Gate dielectrics B: Capacitor dielectrics C: Photoelectrochemical cells
D: Epitaxial dielectrics E: Gate dielectrics for organic transistors on plastic

2.6 Theory of dielectric properties

2.6.1 Permittivity

The permittivity is a fundamental parameter of dielectric properties and is denoted by the greek symbol, ε (epsilon). It defines the ability of a material to polarise in response to an external electric field. A higher permittivity value indicates a greater polarization created by the material under an external field. Relative permittivity, ε_r is also referred as the dielectric constant, *k* that is defined as the permittivity of a material in relation to that of free-space, ε_0 (where $\varepsilon_0 = 8.854x10-12$ F/m). It is a complex measure of the real part, ε' (energy stored) and imaginary part, ε'' (dielectric loss) of the permittivity. The loss tangent (tan delta,δ) denotes the dissipation factor or the losses in a material by the ratio of the imaginary part to the real part of the permittivity as shown in the below equations.

$$k = \varepsilon/\varepsilon_0 = \varepsilon_r^* = \varepsilon' - j\varepsilon'' \tag{2.1}$$

$$\tan \delta = \frac{\varepsilon''}{\varepsilon'} \tag{2.2}$$

The permittivity always relates with the capacitance of energy stored in a dielectric material by neutralizing charges at the electrodes when subjected to the external field (Figure 2.8). This can be expressed by the following equation.

$$C = \frac{\varepsilon_0 * \varepsilon_r * A}{d} \tag{2.3}$$

Where C is the capacitance, A is the area of plate and d is the sample thickness.

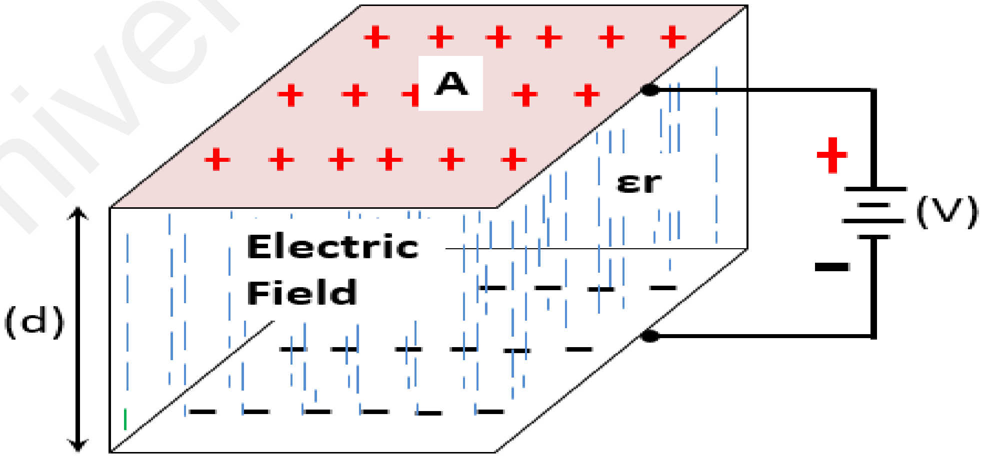

Figure 2.8: The charges orientation of a parallel plate capacitor.

2.6.1.1 Mechanism of the polarization

The measure of permittivity is attributed to the polarization effects when the material interacts with an external electric field. Physically, a dielectric material has random arrangement of the electric charge carriers or electrons around the nuclei. The charges are polarized when subjected to the external electric filed by separating the the positive and negative charges in different direction to the applied field. This lead to the formation of electric dipole moment in the dielectric materials. There are few mechanisms of polarization contributing to the variation in permittivity of materials (Ahmad, 2012):

i. Electronic polarization: It involves the displacement of electrons locally bound in neutral atoms with respect to the nucleus.
ii. Atomic polarization: It occurs due to the distortion or stretching of the adjacent atomic position in a molecule or lattice structure.
iii. Orientational (dipolar) polarization: It most happens in polar polymers or any molecules when there is an imbalance of charge distribution, creating a tendency for permanent dipole moment as the electrons rearrange themselves to align with the electric field.
iv. Interfacial/space charge polarization: It occurs when the mobile charges are impeded at interfacial regions within a material. The accumulation of these charges increases the capacitance with an in increase in relative permittivity.

The characteristics of relative permittivity is dependent on the frequency as the polarization changes with the oscillating electric field. An illustration in Figure 2.9 shows that dipolar (orientational) and ionic polarization have strong interaction at the microwave frequency but quite lossy. This is the principal reason of heating food in a microwave oven. There is a relaxation effect for the dipolar polarization as the frequency increases in microwave region. Whereas the atomic and electronic polarizations are comparatively weak but instantaneously, able to follow in phase with the changes of electric field. These mechanisms could lead to a resonance effect at the frequency beyond 10^{12} Hz.

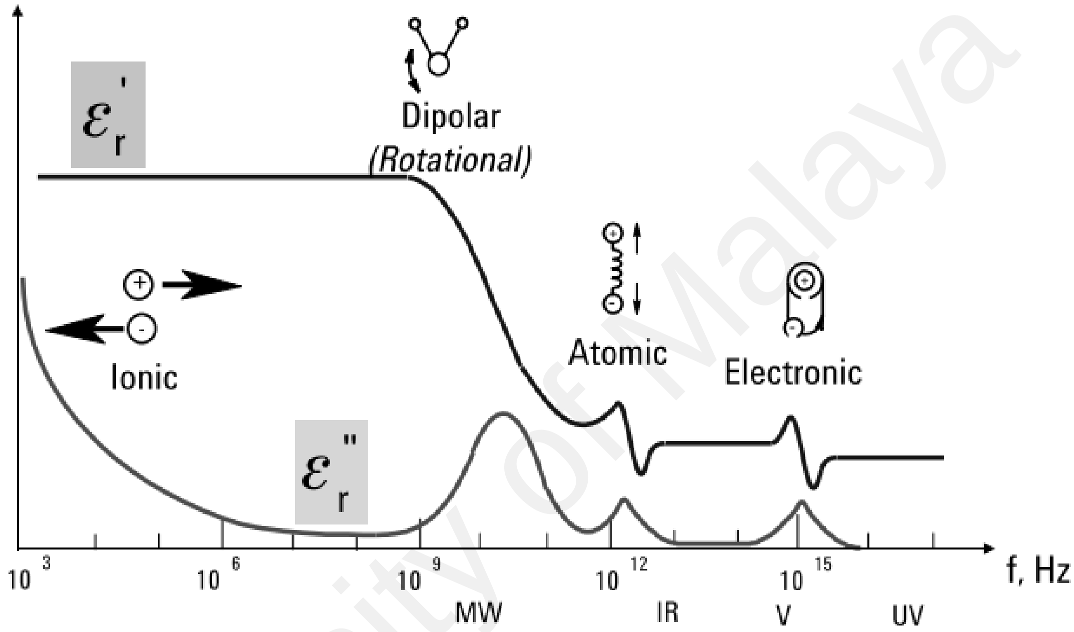

Figure 2.9: The distribution of dielectric mechanisms in response of frequency

2.6.2 Permeability

Permeability (μ_r) defines the response of a material with a magnetic field. It is also a complex quantity that comprised of the real part, μ' (energy stored) and imaginary part, μ'' (energy loss) of the permeability as shown below:

$$\mu_r^* = \mu / \mu_0 = \mu' - j\mu'' \tag{2.4}$$

where μ_0 is the permeability of free space ($\mu_0 = 1.257 \times 10^{-6}$ H/m).

The permeability of nonmagnetic materials is taken close to the permeability of free space ($\mu_r = 1$). Conversely, there is a substantial magnetic property for ferromagnetic materials such as iron, cobalt, nickel and their alloys ($\mu_r > 1$).

2.6.3 Electromagnetic principles

In electromagnetism, the oscillation of current flows create both magnetic field and electric field at the same time. Electromagnetic waves are known varies with wavelength,λ and inversely proportional to frequency of the oscillation ($\lambda = c/f$). Electromagnetic radiation commonly comes from radio waves, visible light or x-rays can propagate in free space and pass through a material at a slower velocity *v,* than the speed of light *c* ($c = 3\text{x}10^8$ m/s). This is because the wave propagation depends on permittivity and permeability of the material under test (MUT) (Figure 2.10). There is a mismatch since the wave impedance in a material *Z,* is lower than the impedance of free space Z_0 orη. This factor causes some of the wave is reflected at material surface while part of the wave is transmitting through the MUT. Therefore, the wavelength, λ_d, within the material is shorter than the initial wavelength λ_0 in free space. Thus, there will be attenuation or insertion loss of the transmitted wave because certain materials also have some losses. These basic electromagnetic principles are simplified as below:

$$\text{Impedance of free space, } \eta = Z_0 = \sqrt{\frac{\varepsilon_o}{\mu_o}} = 120\pi \tag{2.5}$$

$$\text{Impedance of material, } Z = \frac{\eta}{\sqrt{\varepsilon r'}} \tag{2.6}$$

$$\text{The wavelength, } \lambda_d = \frac{\lambda_o}{\sqrt{\varepsilon r'}}, \tag{2.7}$$

The velocity of wave, $v = \frac{c}{\sqrt{\varepsilon r'}}$, (2.8)

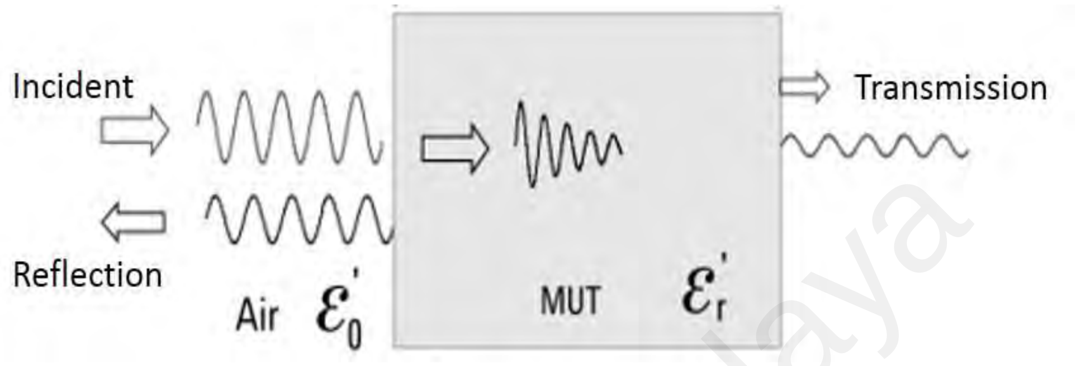

Figure 2.10: Propagation of electromagnetic wave passing through a material.

2.7 Percolation model of conductive fillers

The conducting behaviour of a composite occurs when it undergoes an insulator-to-conductor transition at critical filler loading known as the percolation threshold concentration (PTC). The PTC commonly decreases as aspect ratio of the fillers increases (Deng et al., 2009). However, the electrical conductivity of polymer composites strongly depends on the fillers loading. Figure 2.11 shows typical electrical conductivity behavior of polymer nanocomposites as a function of filler concentration. Below PTC, the composite remains an insulating material since the filler particles are not interconnected or formed small clusters in the polymer matrix. Once PTC value is reached, the particles are able to form a conducting network of fillers and the conductivity increases by many orders of magnitude over a small range of filler loading. In this state, the percolation threshold coincides with the formation of a system spanning, and conduction network of fillers particles in the continuous polymer phase. It implies that conductivity occurs by some tunneling or hoping process through the insulating layer that separates between the filler particles (Grossiord et al., 2008). Far above PTC, the conductivity levels off and do not increase significantly with further addition of the fillers due to the presence of insulating layer between filler particles, which are not in actual contact with each other.

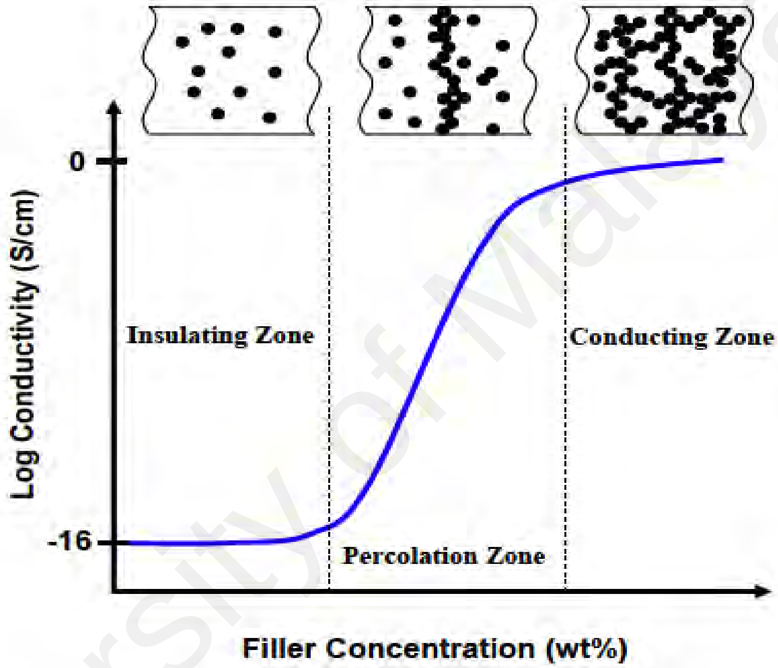

Figure 2.11: Schematic of electrical conductivity as a function of filler concentration (Kim, 2007).

The use of conducting fillers not only increase conductivity but also induce high dielectric permittivity based on Maxwell–Wagner polarization (Dang et al., 2012). The dielectric behavior in a percolating system is very sensitive to the fillers concentration. A slight change in concentration near the percolation threshold can make a drastic change in the dielectric properties and exhibits a non-linear increase in dielectric value beyond the percolation threshold. The conductive fillers with high aspect ratio such as

CNT, always exhibits parallel increases of dielectric permittivity and loss attributed to the increase in conductivity at low percolation threshold.

2.8 The outlooks of high permittivity materials

High permittivity materials have high demands for product miniaturization with high speed performance for the next generation of passive materials in electrical engineering. Apart from electronic industry, they are widely used in many civilian and military applications such as active vibration control, aerospace, underwater navigation and surveillance. For example, rubber composites with high permittivity are used as the cable accessories in electrical engineering to balance the distribution of electric field at cable terminal from failure. Figure 2.12 lists some other potential applications of high permittivity polymer composites.

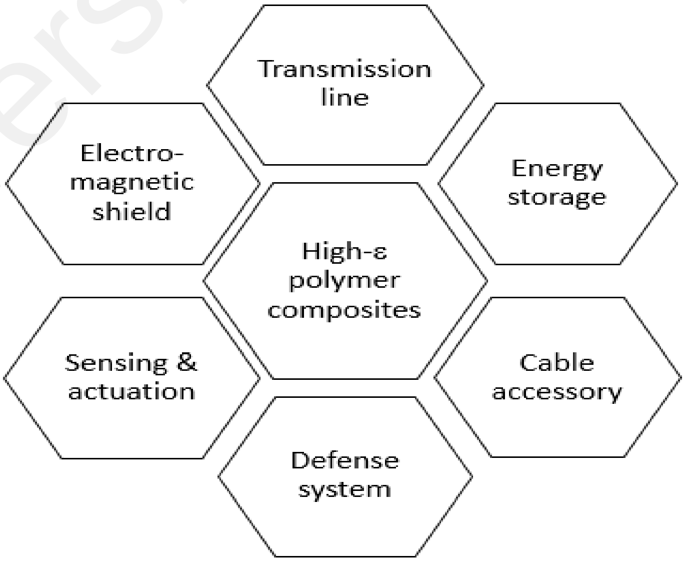

Figure 2.12: The outlooks of high permittivity materials

2.9 Summary

Overall, this chapter provides a brief literature review that covers the study of CNT based materials, silver nanoparticles and their hybrid nanocomposites. The study has cited numerous previous works done by other researchers that are still relevant to the current work. It also outlines the key ideas, few related theories and the outlooks for high permittivity materials.

CHAPTER 3 : METHODOLOGY

This chapter outlines the materials and experimental procedures cover throughout this study. Section 3.1 describes all materials used in the experimental work, while Section 3.2 elaborates samples preparation in three major steps. First part is the functionalization of MWNT by mild oxidation approach. Second part is the synthesis of MWNT-AgNP as the fillers and the third is the fabrication of MWNT-AgNP filled PVA nanocomposites via solution mixing and casting process. Section 3.3 describes various characterization and spectroscopy techniques used to identify the materials and properties of the synthesized samples.

3.1 Materials

Polyvinyl alcohol (PVA) powder (M_w = 31000-50000 g/mol, 98-99% hydrolyzed) was obtained from Sigma-Aldrich. Multi-walled carbon nanotubes (MWNT) with purity of >90% having a diameter of 4-20 nm and length of 10-30 μm were purchased from Nanoshel LLC, Hydrogen peroxide (H_2O_2, 30%) and nitric acid (HNO_3, 65%) supplied by R&M Chemicals were used for mild functionalization of the MWNT. Silver Nitrate ($AgNO_3$, 0.1 mol/L) and N,N-dimethylformamide (DMF, 73.1 g/mol) supplied by R&M Chemicals were chosen as Ag precursor and reducing agent, respectively. Sodium dodecyl sulfate (SDS) obtained from R & M Marketing Essex was selected as surfactants to ensure good dispersion of the MWNT and AgNP.

3.2 Samples preparation

3.2.1 Functionalization of MWNT

MWNT were functionalized through mild oxidation treatment by using nitric acid (HNO_3, 65%), followed by hydrogen peroxide (H_2O_2, 30%). Following this, 1 g of MWNT was treated with 100 ml of HNO_3 in an ultrasonic bath for 30 min. Then the solution was diluted with deionized water and filtered through under vacuum. The filtered material was washed with deionized water for several times until the pH value becomes neutral. These steps were repeated by substituting the solvent with H_2O_2. The filtered carboxylic acid-functionalized MWNT (MWNT-COOH) was dried in an oven set at 60°C for 24 h.

3.2.2 Synthesis of MWNT-AgNP

MWNT-AgNP were synthesized in a single step route via chemical reduction technique by reducing silver ions (Ag^+) from the silver salt ($AgNO_3$) in the presence of MWNT. Initially, 420 mg of acid treated MWNT and 160 mg of SDS were added into 140 ml of DMF, and then sonicated in an ultrasonic bath for 30 minutes. The mixed solution was prepared in four beakers and heated to 80°C, followed by aqueous $AgNO_3$ (0.1 mol/L) into the solutions at a flow rate of 60 ml/min for different volumes percentage (10, 30, 50 and 70 vol%). The hot solution was stirred continuously for 1 h and left to cool at room temperature for 24 h. Then the precipitated material was filtered and washed with ethanol, water and acetone for several times. The final product of MWNT-AgNP were dried in a vacuum oven at 60°C for 24 h.

Table 3.1: Experimental composition of the prepared samples.

Sample names	PVA (mg)	MWNT (mg)	SDS (mg)	$AgNO_3$ (ml)	DMF (ml)
PVA	5000	-	-	-	-
PVA/MWNT	5000	420	160	-	-
PVA/MWNT-AgNP 0.1wt%	5000	420	160	16	140
PVA/MWNT-AgNP 0.3wt%	5000	420	160	60	140
PVA/MWNT-AgNP 1.0wt%	5000	420	160	140	140
PVA/MWNT-AgNP 1.8wt%	5000	420	160	327	140

3.2.3 Synthesis of PVA/MWNT-AgNP nanocomposites

PVA/MWNT-AgNP nanocomposites were prepared via solution mixing technique. Initially 1000 mg of the synthesized MWNT-AgNP powder and 160 mg of SDS were dispersed in 100 ml of distilled water. The mixed solution was ultrasonicated in a water bath for 30 minutes. Next, 5000 mg of PVA was added into the mixed solution and slowly heated to 85°C with continuous stirring at 750 rpm using overhead stirrer. The hot solution was hold for 1 hour to ensure a homogenous solution throughout the heating process. Then, the viscous solution was immediately cast to glass Petri dishes of 10 cm in diameter and left to dry at ambient room temperature. Subsequently, the prepared composite films were peeled off from the Petri dishes and stored in a vacuum desiccator before characterizations. The average film thickness was obtained about 0.32 mm. These steps were repeated to fabricate various samples of PVA/MWNT-AgNP nanocomposites with different AgNP loading as shown in Table 3.1. The concentration of AgNP present in the samples were determined by using inductive coupled plasma-optical emission spectrometer (ICP-OES) analysis and were obtained as 0.1, 0.3, 1.0

and 1.8 wt%. Additionally, pure PVA and PVA/MWNT were fabricated with similar procedures of the PVA/MWNT-AgNP nanocomposites. The schematic diagram of experimental procedure is illustrated below in Figure 3.1.

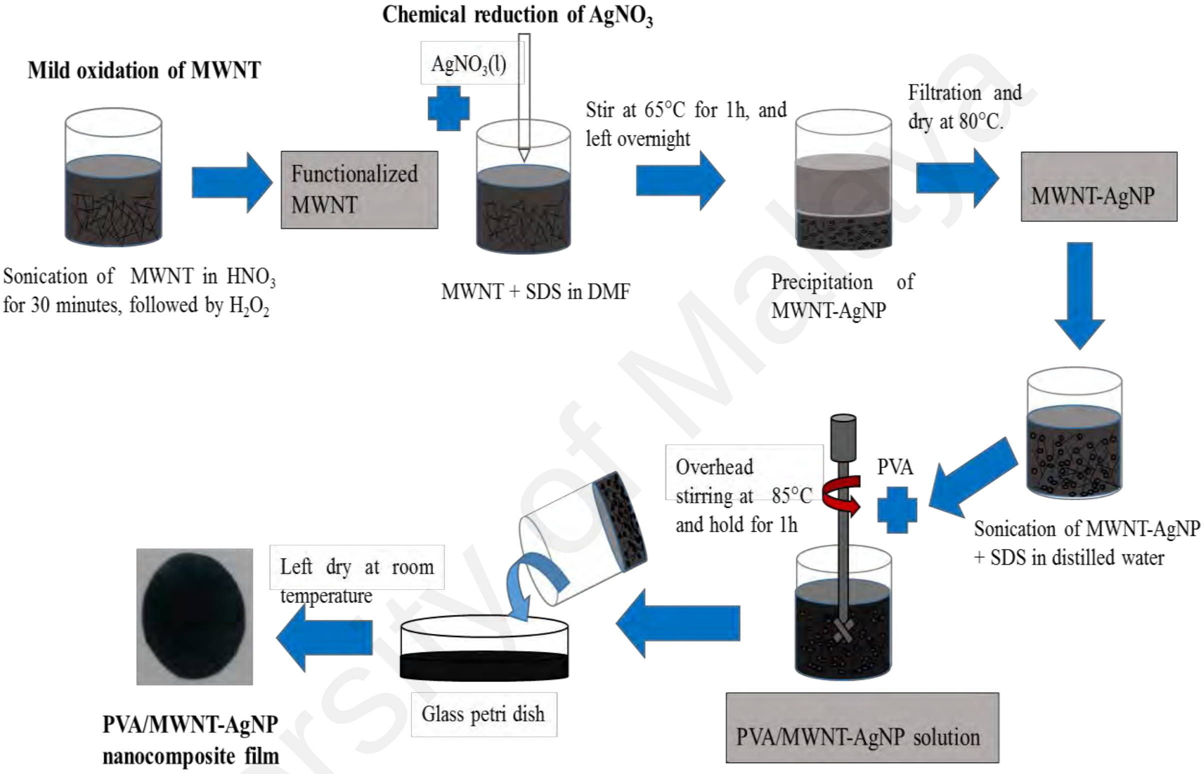

Figure 3.1: Schematic synthesis of PVA/MWNT-AgNP nanocomposites.

3.3 Characterization techniques

3.3.1 X-Ray diffraction (XRD)

X-Ray diffractometer (XRD) is a non-destructive technique used for determination of crystallographic structure, phase purity and interplanar spacing of a crystalline material. XRD is based on constructive interference of monochromatic X-rays generated by heating the filament of a cathode ray tube and directed towards the crystalline sample. Figure 3.2 shows the interaction of incident x-rays with the samples produces diffraction (constructive interference) equation according to Bragg's Law:

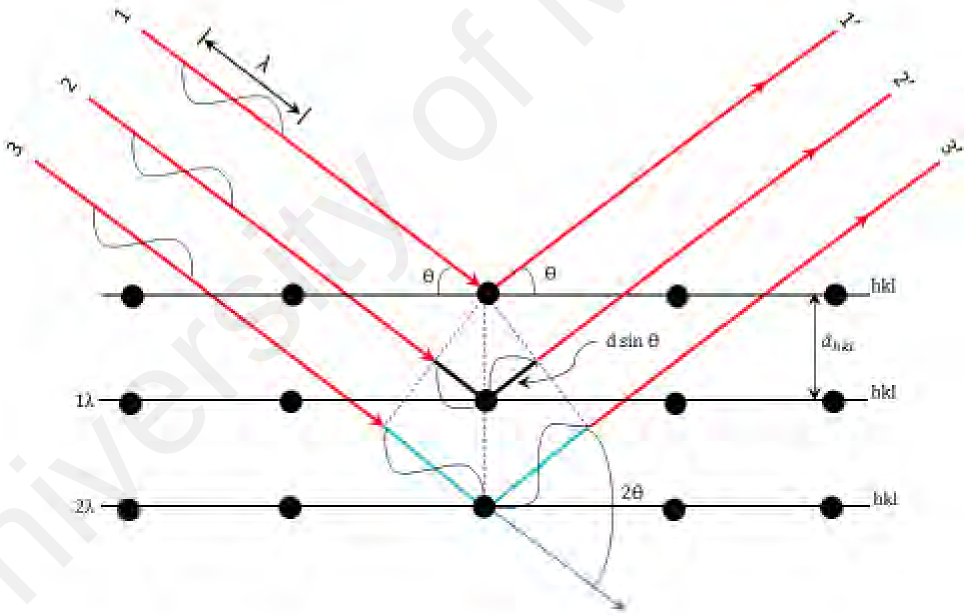

Figure 3.2: Constructive interference of x-ray beams at *hkl* planes.

$$n\lambda = 2d \sin \theta \qquad (3.1)$$

where n is an integer for crystalline planes, λ is the radiated wavelength, d is the crystalline lattice spacing, and θ is the diffraction angle of incidence rays. Phase identification of a mineral can be found from conversion of the diffracted peaks to lattice spacing (*d*) by comparing the d-spacing with standard reference pattern. Interplanar spacing is a function of Miller indices (*hkl*) and lattice parameter, *a* can be determined for each crystal structure:

$$d_{hkl} = \frac{a}{\sqrt{h2 + k2 + l2}} \tag{3.2}$$

The crystallite size, D can be calculated from the half width-maximum peak by Scherer equation:

$$D = \frac{K\lambda}{\beta \cos\theta} \tag{3.3}$$

where *K* is the shape factor, and *β* is the peak broadening at half-maximum intensity in radians. The shape factor for spherical crystalline grains is 0.9 and *D* denotes to the grain size of the nanoparticles. The XRD pattern of the samples were recorded using a PANalytical EMPYREAN X-ray diffractometer with CuKα radiation of λ = 1.54060 nm. The data was collected by scanning the samples through diffraction angle in the range of 2θ = 10° to 80°.

3.3.2 Ultraviolet-visible spectroscopy (UV-Vis)

UV-Vis spectroscopy measures the absorption of light through a liquid sample within ultraviolet and visible wavelength. When an electromagnetic radiation set upon a sample, the absorption of photon causes the atoms and molecules to undergo transitions from ground state to higher electronic state. According to Bohr's model, every electron in an atom exhibits a discrete energy level. Ultraviolet and visible light are energetic enough to promote outer electrons to the higher energy levels. The more easily the electrons excited, it can absorb the longer wavelength of light. The concentration of an analyte in solution can be determined from the absorbance at certain wavelength in accordance to Beer-Lambert Law:

$$A = -\log T \tag{3.4}$$

$$T = I/I_o \tag{3.5}$$

where A is the absorbance, T is the transmittance, I is the transmitted light intensity and I_o is the incident light intensity.

The UV-Vis measurements was carried out using a Carry Win UV 50, spectrophotometer. The absorption spectra were scanned at low rate within wavelength from 200 nm to 800 nm. The samples were dispersed in deionized water and treated in an ultrasonic bath for 20 minutes to ensure good dispersion of the solution. Then the solution was put in a rectangular and transparent cell, known as quartz cuvette with an internal width of 1 cm prior to the UV-Vis measurements.

3.3.3 Fourier-transform infrared (FTIR)

Fourier transform infrared (FTIR) spectroscopy is a rapid characterization tool used to identify vibrational frequency of different chemical bonds presence in most materials. Principally, FTIR uses an interferometer and polychromatic light to generate an interferogram, and then mathematically decoded by a fourier transformation. IR process measures vibrational frequency of bonds in molecules triggers through irradiation with infrared light. Upon irradiation with infrared light, certain bonds induces stronger molecular vibrations that can be detected and translated into a visual representation called IR spectrum. The IR spectrum of the samples were analysed using a PerkinElmer-Spectrum 400 FTIR spectrometer. It provides information on molecular fragments of certain functional groups and molecular fingerprint of the nanocomposites. The measurement was taken with a scan rate of 4-16 cm^{-1}/min within a wavenumber range from 400 cm^{-1} to 4000 cm^{-1}.

3.3.4 Raman spectroscopy

Raman spectroscopy is a spectroscopic technique that is extremely sensitive to geometric structure and bonding within molecules. This technique is used to characterize quality and purity of different carbon allotropes such as carbon carbon nanotubes, graphene, diamond etc. Raman scattering also known as Raman Effect refers to inelastic scattering of monochromatic light from a laser source. The inelastic scattering occurs when the monochromatic light changes upon interaction with a sample. The light may be reflected back, absorbed or even scattered in different ways. There are two types of scattering: elastic scattering (known as Rayleigh scattering) and inelastic scattering (known as Raman scattering). Raman scattering can be classified based on their energy level: Stokes Raman scattering (higher energy level) and Anti-Stokes Raman scattering (lower energy level). The difference in energy level is mainly due to the vibrational or rotational energy of the molecules in the sample. The schematic illustration as shown in Figure 3.3. Micro-Raman spectrometer (HORIBA Scientific, JOBIN YVON) was used to characterize the vibrational properties and structural changes of MWNT in the presence of AgNP. The spectrometer uses a green laser with an excitation wavelength of 532 nm and equipped with a CCD detector. The acquisition time was set at 20-30 s for at least two cycles. Ten different spots were taken for the analysis.

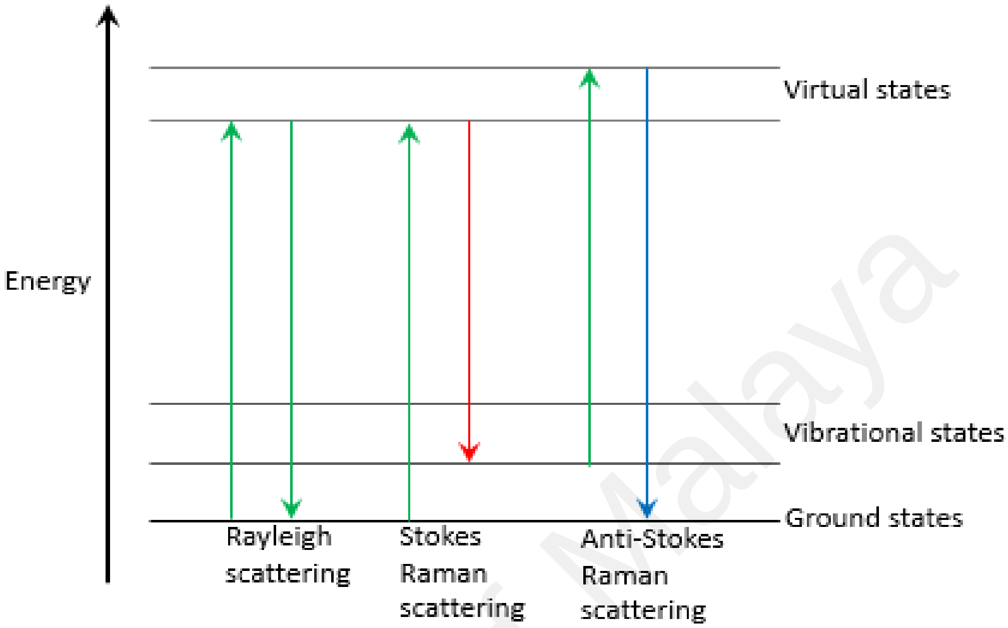

Figure 3.3: Illustration of different energy transitions in Raman Scattering.

3.3.5 Thermogravimetric analyzer (TGA)

Thermogravimetric analyzer (TGA) is an analytical technique used to evaluate thermal stability and the decomposition behavior of a material as it is heated. Through TGA process, the weight changes of a substance is monitored as a function of temperature or time in a controlled atmosphere. It also can measure the loss of water or solvent, oxidation, catalytic residue, as well as the filler and ash content. This equipment consists of a sample pan that is supported by a precision balance in a furnace that can be heated or cooled during the analysis. The procedure commonly employs air, oxygen, argon, or nitrogen as the sample atmosphere where the gas flows over the sample and exits through an exhaust.

The thermal analysis was conducted using a TGA MettlerToledo,SDTA851e to analyze decomposition behavior and filler content of the samples. The sample size is approximately 10 mg and was placed in an aluminium pan. The test was carried out at a heating rate of 10° C/min within a temperature range of 40–600° C under air atmosphere.

3.3.6 Field emission scanning electron microscopy (FESEM)

FESEM is a microscopic technique used to examine surface and structures of a sample with a wide range of magnification (15 to 100,000x). It uses field emission to generate electron beam that is about 1000 times smaller than the standard SEM. When the electron beam bombards on the surface of a sample, the reflected beam of electrons is collected by a detector to produce electronic signals that is displayed on a cathode ray tube. The reflected beam comprises of different scattering mainly secondary electrons and backscattered electrons (Figure 3.4). The secondary electrons are used for viewing the surface topography while backscattered electrons control the image contrast.

FESEM was performed to observe surface morphology of the MWNT-Ag and its nanocomposites by using an FEI QUANTA 450 FEG at accelerating voltage of 3kV. The samples are mounted on a special holder before inserted into the high vacuum part of the microscope through an exchange chamber that fixed on a moveable stage. For non-conducting sample, it is often coated with a very thin layer (1.5 - 3.0 nm) of gold or other metals to achieve better resolution with good quality signal. Energy dispersive X-ray (EDX) analysis was performed by using investigative tool in FESEM to determine composition and elements present in the samples. It was operated at a voltage of 15 kV. The analysis includes the identification of lines and intensities in the EDX spectrum.

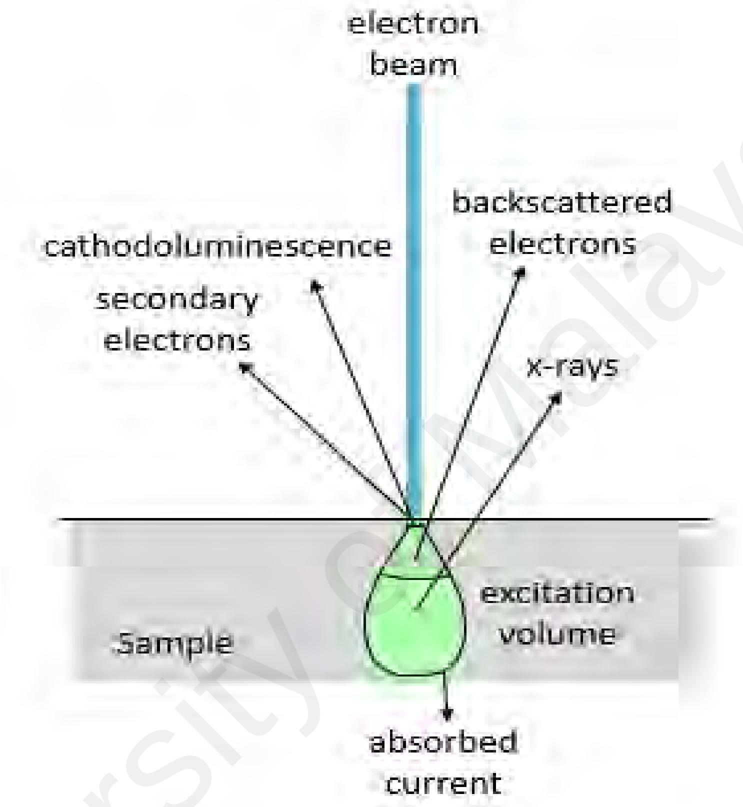

Figure 3.4: Different scattering of the reflected electrons beam.

3.3.7 Transmission electron microscope (TEM)

TEM is a useful microscopic technique for the analysis of internal microstructures in a sample. The principle work is using a beam of electrons that is transmitted through a sample to form an image. The sample must be prepared in very thin section to allow transmission of the incident beam through the material. TEM analysis was employed by using JEOL-JEM 2100-F to determine the particle size, nanotube structures and crystal orientation of the as-synthesized MWNT-AgNP. The sample was dispersed in a deionized water and was subjected to ultrasonication in a water bath for 20 minutes. It is important to ensure well dispersion of the materials before the analysis. Then the suspension was dropped onto a support film, formvar/carbon coated-copper 300 mesh grids with a diameter of 3.05 mm. The grid was placed on a sample holder before inserted into high vacuum part of the machine.

3.3.8 Metrohm Autolab

Metrohm Autolab Potentiostat is a high technology electrical instrument that allows different types of experiment with various compatible instruments. It is able to run cyclic voltammetry, linear sweep voltammetry, chrono methods, electrochemical noise and many other applications. In this work, current-voltage (I-V) characteristics of the samples were measured by using an Autolab Potentiostat (PGSTAT204), equipped with an advanced electrochemical software, Nova 1.10.1. The Autolab calibration was initially performed by checking the wires connection with a simple circuit system or known as a dummy cell.

The testing was prepared by sandwiching a circular sheet of the nanocomposite with a diameter of 25 mm between two steel foils on both sides of the sample. This is important to ensure a good electrical contact between top and bottom of the sample holder. The measurement was carried out by using a linear sweep voltammetry (LSV) staircase. The parameter used a scan rate of 0.05V/s and step potential of 0.20V. The applied voltage was varied from 1 to 10V. Electrical conductivity of the samples are determined based on the current-voltage relationship as follows:

$$\sigma = d/RA\ (\Omega.m)^{-1} \qquad (3.6)$$

where, d is the sample thickness, *A* is the surface area, and R is the resistance estimated by the gradient (*m=1/R)* as a relation with linear fit of the I–V graph.

.

3.3.9 Impedance spectroscopy

Impedance spectroscopy (IS) is a common tool used to measure dielectric properties of a material stimulated by an alternating current (AC) at low frequency. Impedance is the electrical resistance to the AC source in a complex electrical system. The dielectric measurement for the nanocomposites was performed by using HIOKI LCR HiTester. In this technique, the nanocomposites with average film thickness of about 0.32 mm was sandwiched between two disk electrodes of 25 mm diameter to form a capacitor (Figure 3.5). The measurement was tested as a function of frequency within range from 100 Hz to 1 MHz at room temperature and the applied voltage was monitored at 1V.

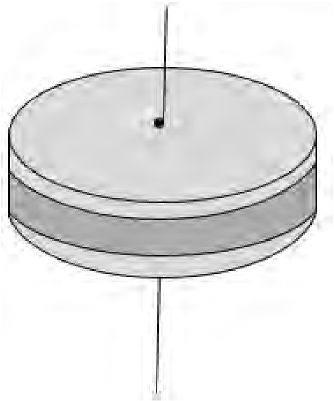

Figure 3.5: An illustration of the material under test for IS.

The data from IS were analyzed by Nyquist or Cole-cole plot (Figure 3.6). The frequency dependence of the dielectric properties and ac conductivity of the nanocomposites can be calculated from real, Z' and imaginary, Z'' components of the complex impedance, |Z| as the following relations:

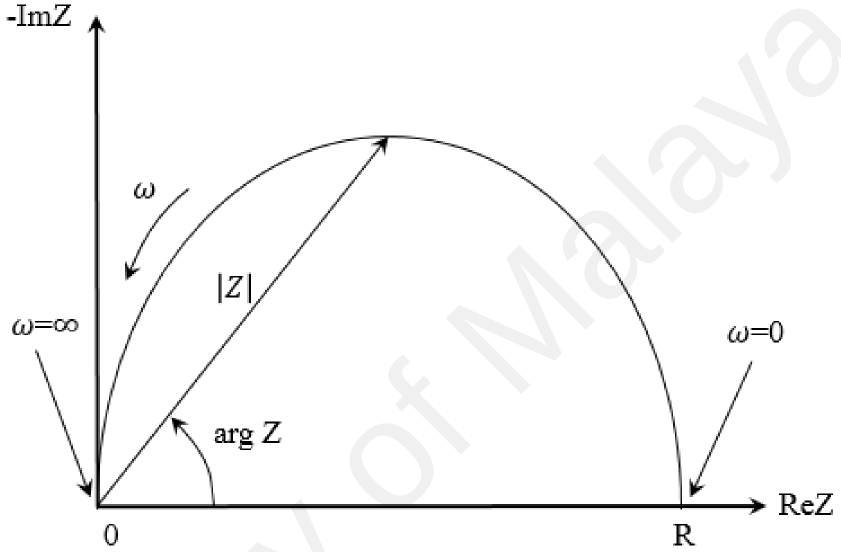

Figure 3.6: A Nyquist plot diagram.

$$Z' = Z \cos \varphi \tag{3.7}$$

$$Z'' = Z \sin \varphi \tag{3.8}$$

where φ is the phase angle. While permittivity defines the response of an external field with the electric dipole moment of the sample. The dielectric permittivity, ε′ and the dielectric loss, ε″ of the nancomposites were calculated from subsequent equation:

$$\varepsilon' = \frac{Z''}{2\pi f C_{\circ} Z^2} \tag{3.9}$$

$$\varepsilon'' = \frac{Z\prime}{2\pi f C_{\circ} Z^2} \tag{3.10}$$

where f is the measuring frequency, C_o is the capacitance of the two electrode plates without sample and calculated by $C_o = \varepsilon_o A/d$, where A is the film area, d is the thickness, ε_o is the permittivity of the free space = $8.854\text{x}10^{-12}$. The ac conductivity (σ_{ac}) of the thin film samples at a frequency were obtained from the following equation:

$$\sigma_{ac} = 2\pi f \varepsilon_o \varepsilon'' \tag{3.11}$$

Dielectric modulus is used to analyze relaxation phenomenon due to space charge polarization by using the dielectric formula (Zhen, Arredondo, & Zhao, 2013). The dielectric modulus in complex form is given by:

$$M^* = \frac{1}{\varepsilon^*} = M' + iM'' \tag{3.12}$$

where M′ and M″ are the real and imaginary part of dielectric modulus. Calculation of the dielectric modulus is given by the following formula:

$$M' = \frac{\varepsilon\prime}{(\varepsilon'^2 + \varepsilon\prime\prime^2)} \tag{3.13}$$

$$M'' = \frac{\varepsilon\prime\prime}{(\varepsilon'^2 + \varepsilon''^2)} \tag{3.14}$$

3.3.10 Vector Network Analyzer

Vector network analyzer (VNA) is an instrument that enables high frequency stimulus-response commonly used for radio frequency and microwave measurements. The test involves measurement of both magnitude and phase from the incident, reflection, and transmission waves that pass through a transmission line. A common transmission line technique is using a section of rectangular a waveguide or a coaxial airline. The measurement is carried out by using N5227A PNA network analyzer, Keysight Technologies (formerly known as Agilent Technologies) that comes with 2-ports connected to X-band waveguide WR-90 that has 4 holes fixed at both ends (Figure 3.7). The nanocomposite sheets were enclosed on a sample launcher of rectangular waveguide with dimension of 23 x 10 mm. The VNA was calibrated based on Thru Reflect Line (TRL) calibration technique for 201 frequency points. The calibration standard cancelled out the effect of cables and connectors as well as imperfections of the test setup by testing the sample using an ideal reflector and absorber.

Figure 3.7: The setup of X-band waveguide connected with the VNA.

The test allows simultaneous measurement of electrical network scattering parameters or S-parameters (S_{ii}) between the two ports by using an algorithm software, 85071E to perform the conversion of complex permittivity, ε* and permeability, μ* (Figure 3.8). The TRL setup directly measures the reflected power signal (S_{11}) and transmitted power signal (S_{12}) over the given frequency range from port 1 to port 2 and vice versa. Thus, the electromagnetic characterization for transmission (T), reflection (R) and absorption (A) can be simply expressed by the following equations:

$$T=|S_{12}|^2 = |S_{21}|^2 \tag{3.15}$$

$$R=|S_{11}|^2 = |S_{22}|^2 \tag{3.16}$$

$$A= 1-R-T \tag{3.17}$$

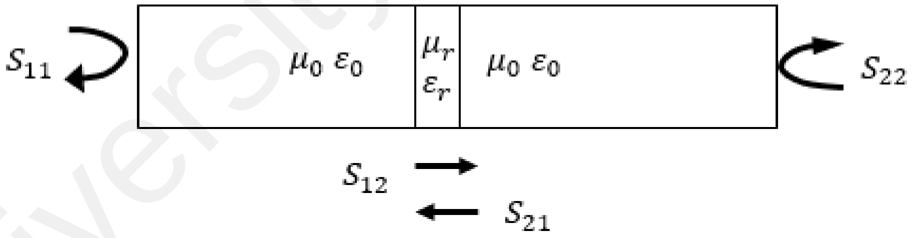

Figure 3.8: Measurement of S-parameters in a X band waveguide (Soleimani et al., 2012)

3.3.11 Summary

A complete view of the sample preparation and characterizations involved through this study are summarized in the flowchart as shown in Figure 3.9.

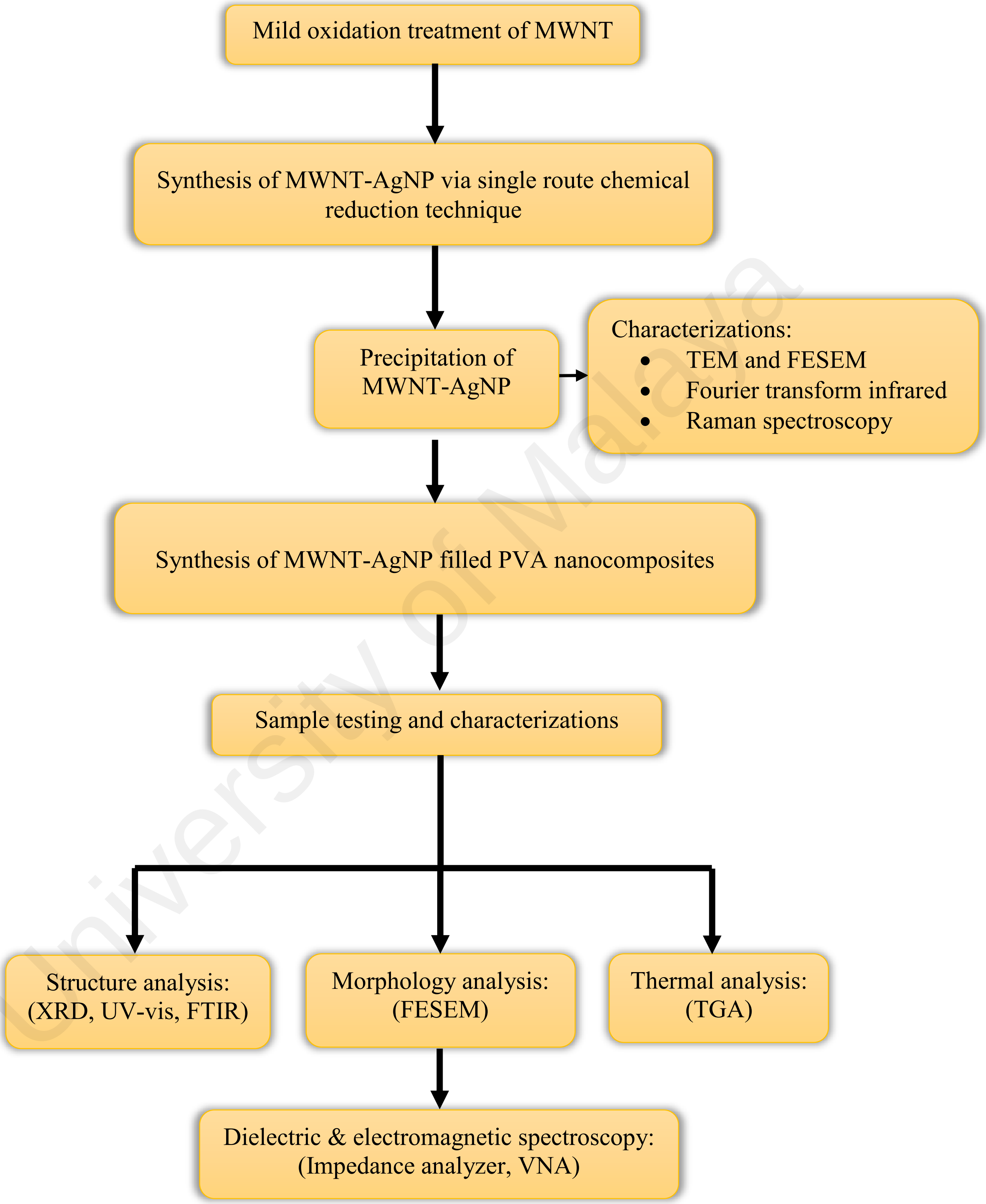

Figure 3.9: Experimental flowchart of research work.

CHAPTER 4 : RESULTS AND DISCUSSION

This chapter is about the results and discussion of research work that comprised of two main sections: Section 4.1 discussed the results of decorating AgNP onto MWNT (MWNT-AgNP) as hybrid fillers are obtained via single step of chemical reduction technique. While Section 4.2 discussed the results of MWNT-AgNP reinforced PVA nanocomposites. The main findings are discussed and interpreted in terms of morphology, structural, thermal, electrical and dielectric properties. The results have addressed the significance of MWNT-AgNP with different loading of AgNP (0.1, 0.3, 1.0 and 1.8 wt%) in tailoring high permittivity PVA nanocomposites at low-frequency (100Hz-1MHz). Furthermore, the findings have revealed the electromagnetic characteristics of the nanocomposites in X band frequency.

4.1 Properties of MWNT-AgNP hybrid

4.1.1 Microstructure analysis

Morphology of pristine MWNT and MWNT-AgNP hybrid are shown by field-emission scanning electron microscopy (FESEM) images in Figure 4.1. The FESEM images show that pristine MWNT are clear like slender fibers and much bend at the end tubes. Whereas the hybrid structure of MWNT-AgNP shows the presence of much spherical AgNP deposited on the MWNT surfaces. The particles seems brighter due to a higher atomic number of silver (Ag) than that of carbon (C). The formation of AgNP is due to the reduction of Ag^+ in DMF solution. In this work, the applied temperature during synthesis process could increase reaction rate and monodispersity of AgNP than the reaction at room temperature (Santos & Marza, 1999). The reaction is stated as below.

$$HCON(CH_3)_2 + 2Ag^+ + H_2O \rightarrow 2Ag + (CH_3)_2NCOOH + 2H^+ \qquad (4.1)$$

The energy dispersive X-ray (EDX) spectrum in Figure 4.2 shows a strong peak of C followed by Ag peaks that indicates the dominance of carbon contents as compared to silver content. It confirms the deposition AgNP onto the MWNT surface in the hybrid structures. The small peaks attributed to Na and S are coming from the used of surfactant, SDS while N peak was obtained during the reduction process of AgNP with DMF as shown in Equation 4.1. A low peak of oxygen designates the formation of carbon containing oxygen-functional groups (COOH) on sidewalls of the nanotubes produced after mild oxidation treatments, which is needed to preserve good electrical conductivity of MWNT. This is discussed further by Fourier-transform infrared (FTIR) analysis.

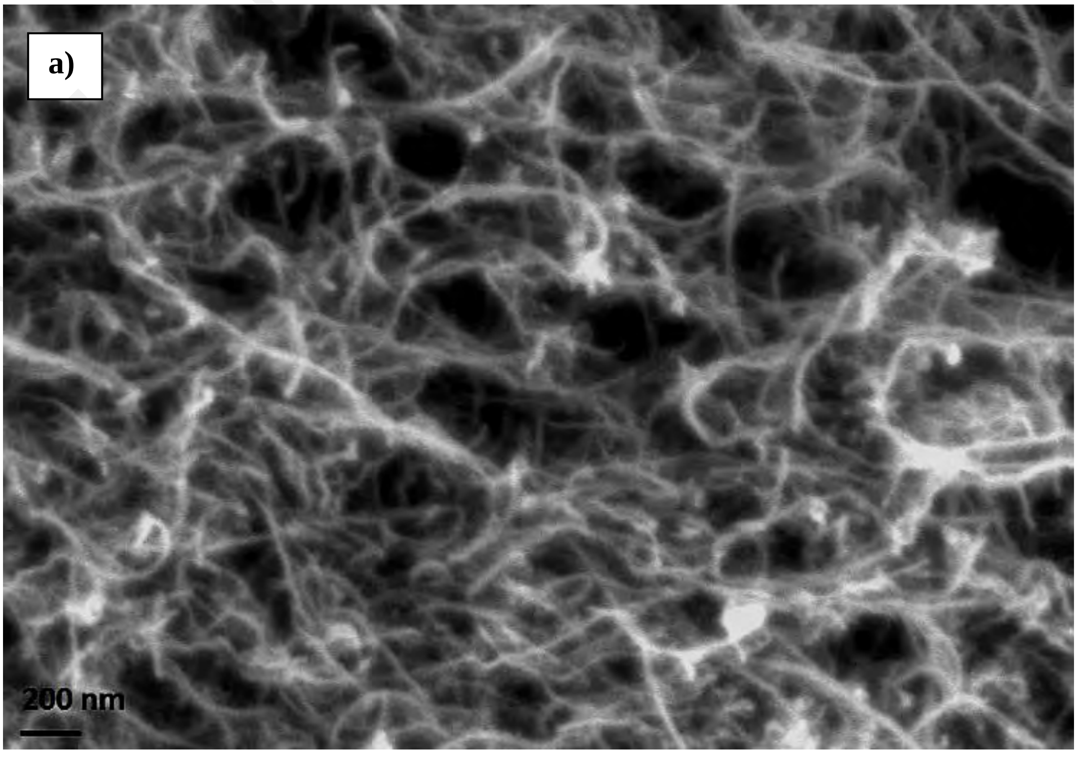

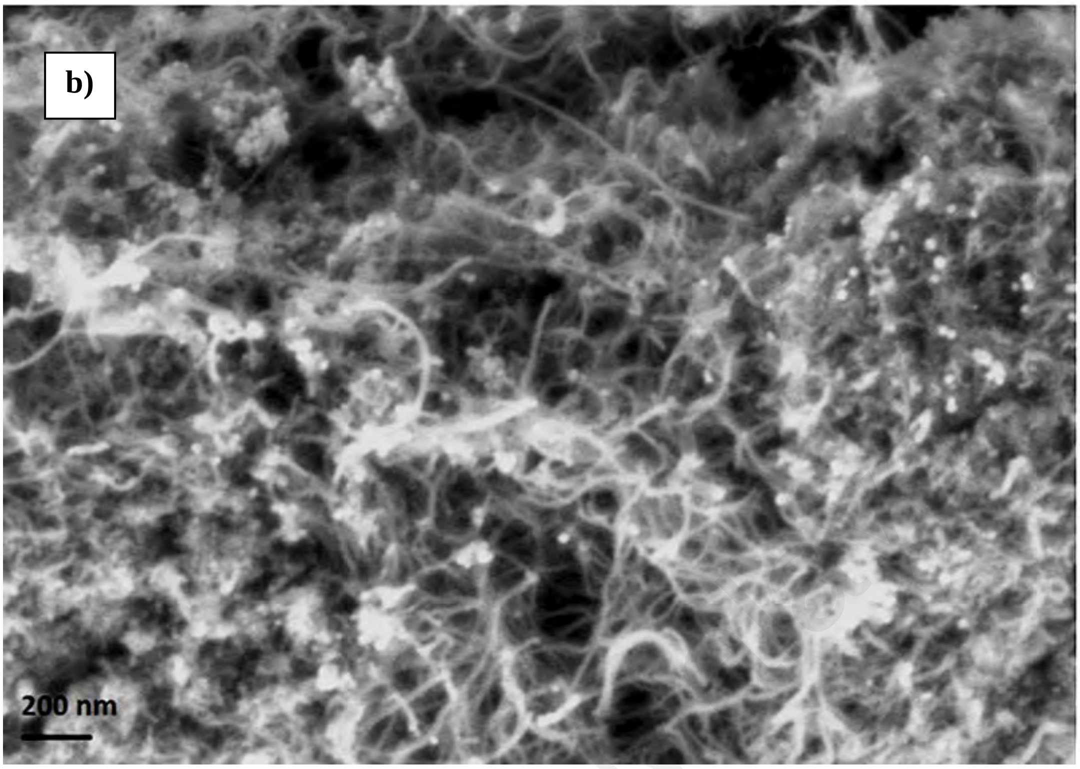

Figure 4.1: FESEM images (a) pristine MWNT and (b) MWNT-AgNP hybrid.

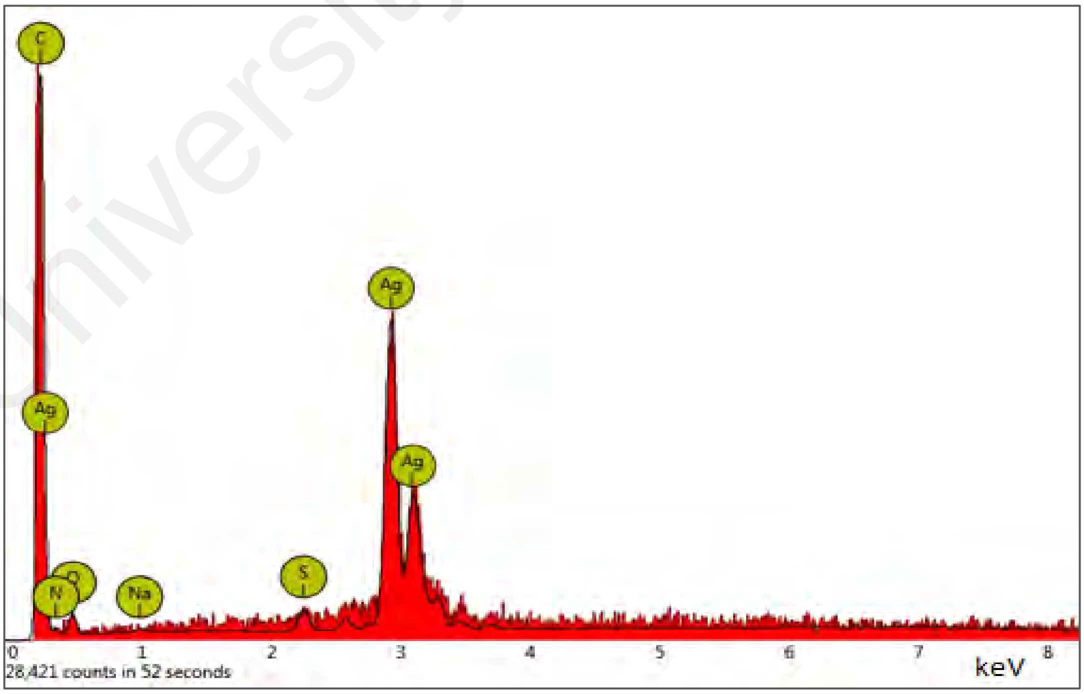

Figure 4.2: EDX spectrum of the MWNT-AgNP hybrid.

Meanwhile, the particles size and internal structures of the MWNT were analysed by using transmission electron microscope (TEM). Figure 4.3 shows the TEM images of MWNT-AgNP synthesized at different volume of $AgNO_3$ as the Ag precursor. The images reveals actual nanotube structures of MWNT having an outer and inner diameters of 10-20 nm and 4-7 nm, respectively. The presence of AgNP can be spotted as the dark fine particles with average particle sizes from 5 to 10 nm. It can be seen that some of the AgNP was deposited onto the nanotube surfaces, while others are isolated around the nanotubes due to homogeneous nucleation of the AgNP during the synthesis process. In this work, the formation of carboxylic groups might be limited via mild oxidation treatment because the functionalization on MWNT surfaces were not fully covered.

Therefore, the addition of SDS is required to reduce van der Waal attractions and support well dispersion of MWNT. At the same time, SDS could help the heterogeneous nucleation of AgNP on MWNT surface (Georgakilas et al., 2007). As the concentration of AgNP produced is high enough with increasing the volume of $AgNO_3$, it could lead to the aggregation of AgNP to form Ag clusters because of steric effect (Song et al., 2009). This circumstance captivate the MWNT that have been much bent and kinked to accumulate around the AgNP due to the insufficient debundling power of SDS as the anionic surfactant to disperse the individual nanotubes when the concentration of SDS was remain unchanged. It appears that disturbing the nanotube structures at very high concentration of AgNP assembled on the surface can increase bonding/linking of the nanotubes due to defect in graphite structure. This can be discussed further in Raman spectroscopy analysis.

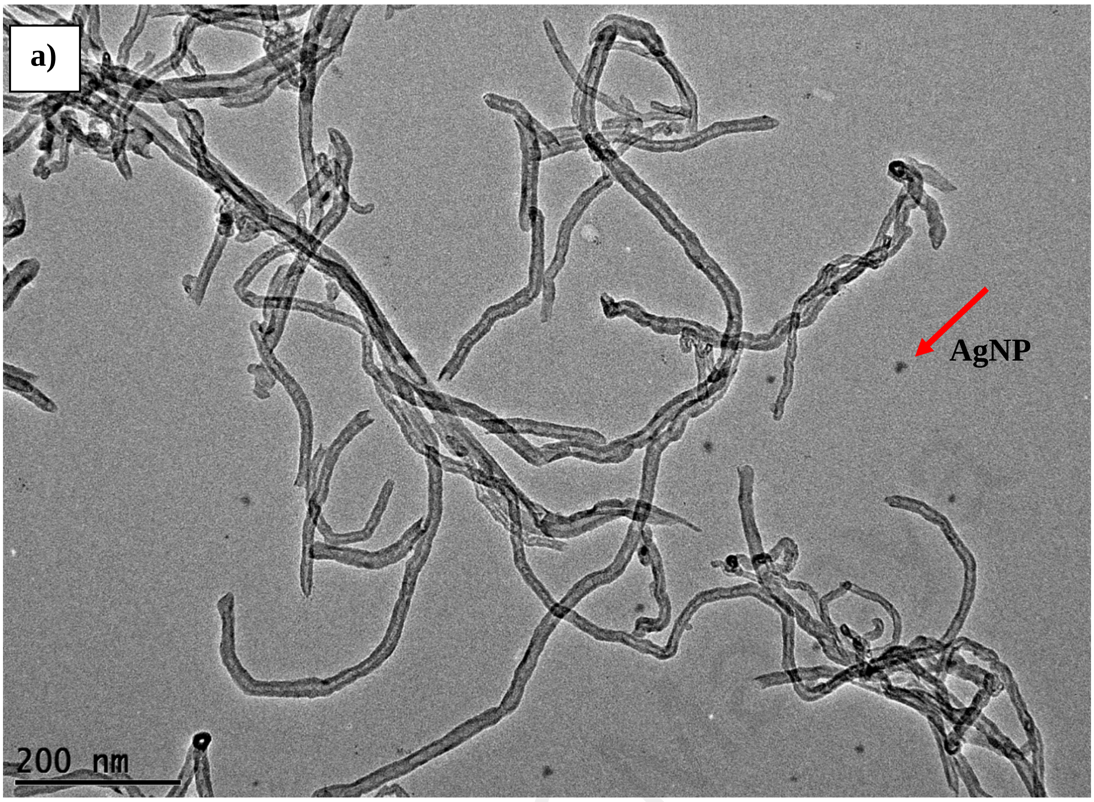
a)
AgNP
200 nm

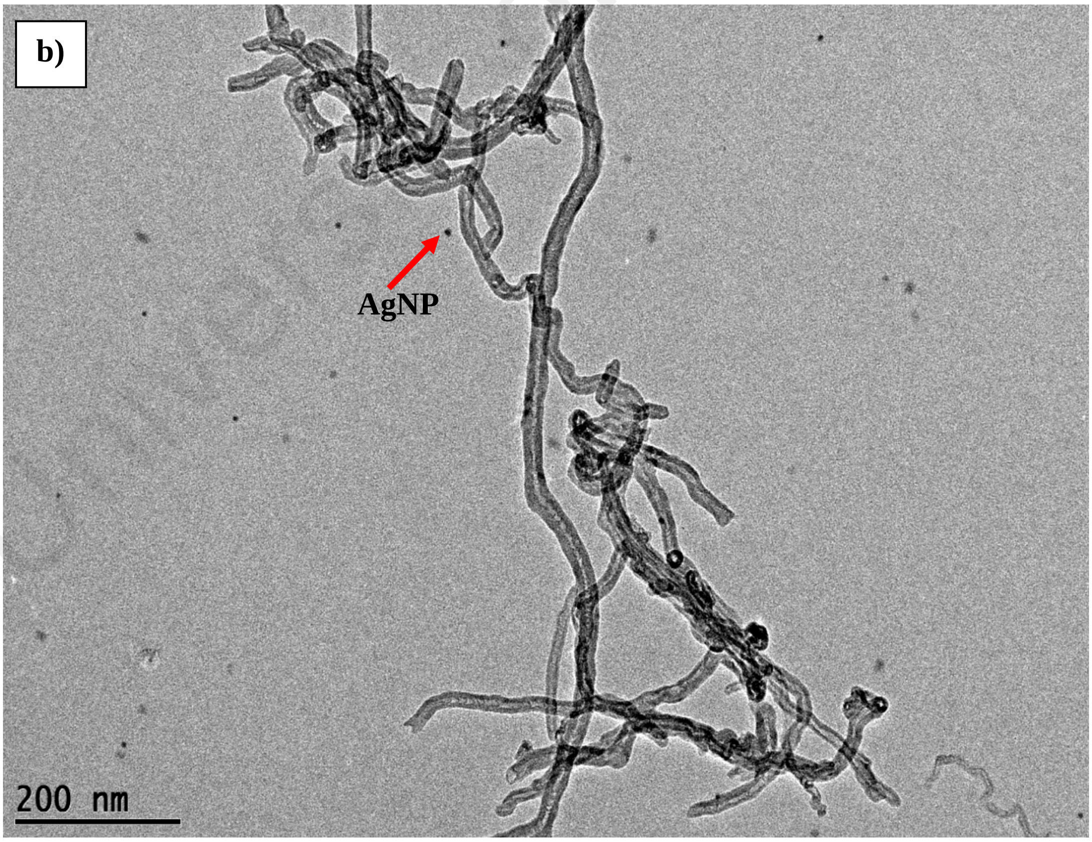
b)
AgNP
200 nm

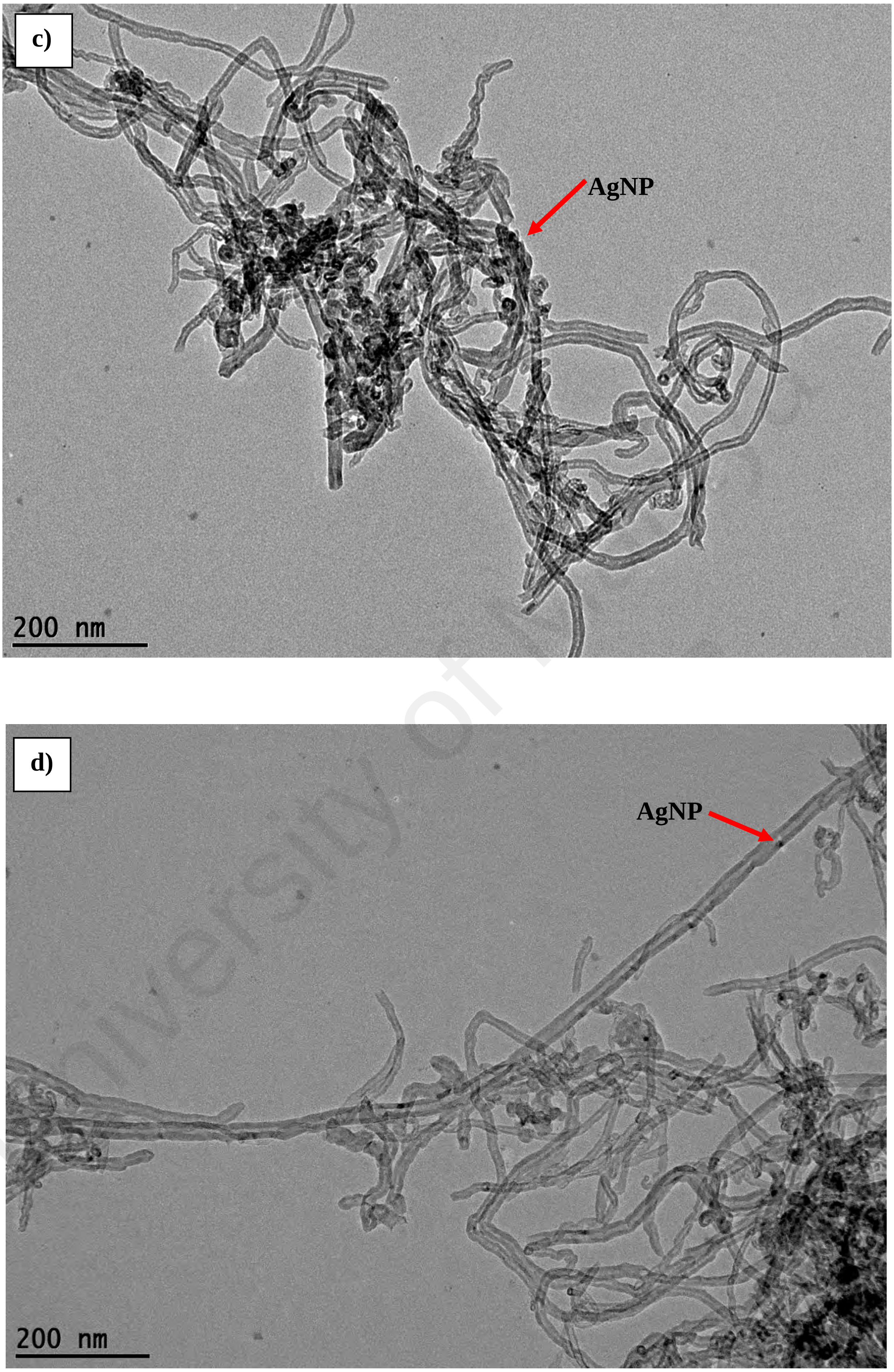

Figure 4.3: TEM images of MWNT-AgNP hybrid obtained with different vol. % of $AgNO_3$ (a) 10 (b) 30 (c) 50 (d) 70.

High-resolution TEM image in Figure 4.4 shows AgNP that is deposited onto the outer surface of MWNT. The measured spacing of lattice fringes in the image corresponds to MWNT and AgNP was 0.34 nm and 0.23 nm (111) planes, respectively. This observation indicates the deposition of AgNP with MWNT are crystallized structure, which is consistent with some others work (G. Lu et al., 2007) (Peng & Chen, 2012). The mechanism for direct deposition of AgNP onto the surface of the MWNT is illustrated in Figure 4.5. The interactions between carboxyl groups (COOH) and the Ag cations (Ag^+) resulted in self-assembly of AgNP onto the functionalized MWNT. The self-assembly process involved the electrostatic interactions between SDS molecules with Ag^+ to obtain positively charged of Ag-SDS nanoparticles, which assembled with negatively charged from carboxylic groups created on sidewalls of the nanotubes.

However, the adsorption of ionic surfactant much depends on the amount of purification and functionalization of the nanotube surfaces. The AgNP also can be nucleated via precipitation with functionalized CNT without additional of the ionic surfactant, but strong chemical oxidation can cause severe damage to the nanotube structure (Ramin & Taleshi, 2013). The drawback of severe cnt damage can limit their great potential as electrical reinforcement. Instead, the adsorption of the SDS molecules also may occur without functionalization of the nanotubes. The decoration of AgNP is attained from supramolecular self-assembly of the SDS molecules onto the surface of the nanotubes. It is promoted through electrostatic interactions between the hydrophobic linear chains of the SDS molecules and the sidewalls of the nanotubes (Valmalette et al., 2014).

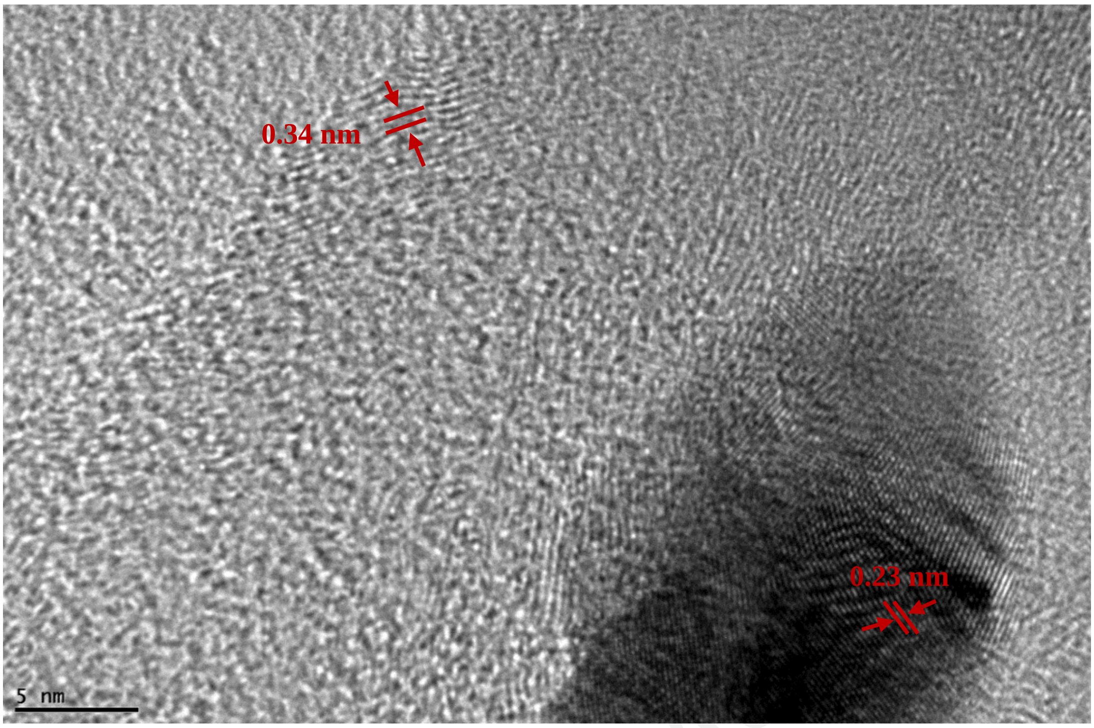

Figure 4.4: HRTEM image of AgNP deposited onto the MWNT surface.

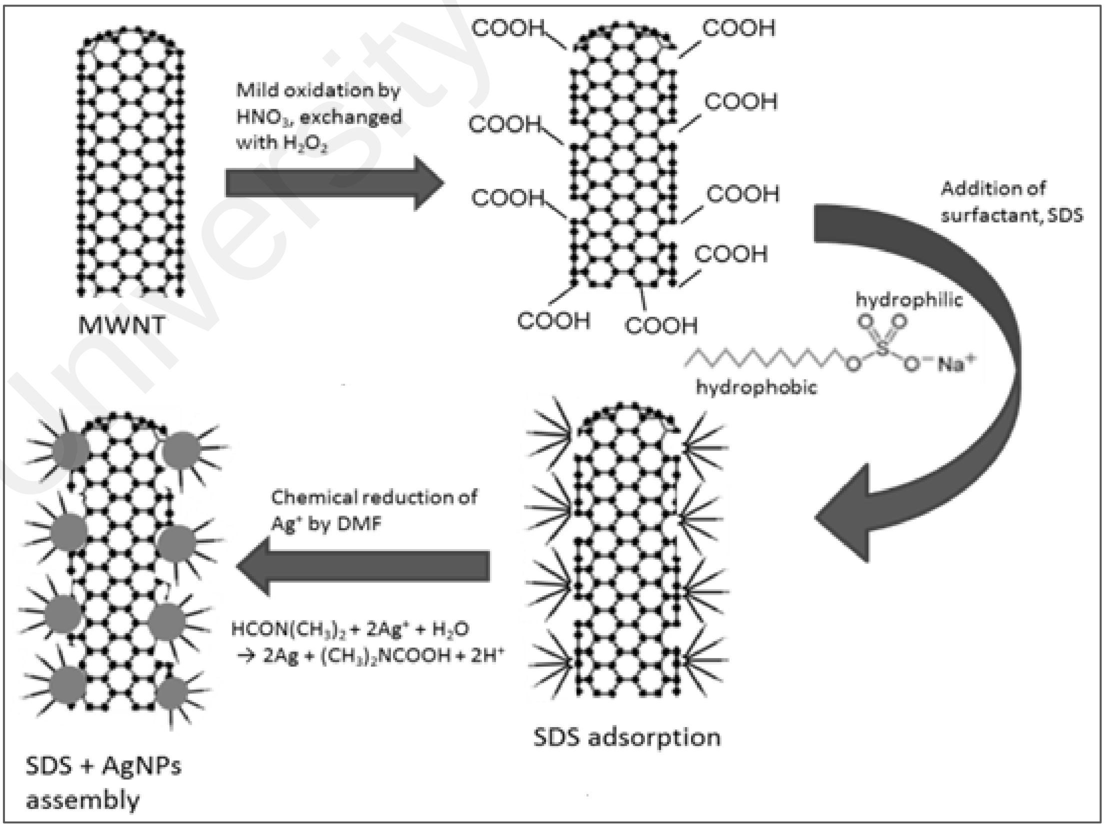

Figure 4.5: A schematic mechanism of depositing AgNP onto MWNT surface.

4.1.2 FTIR spectroscopy analysis

Figure 4.6 shows the FTIR spectra representing the functional groups of MWNT-AgNP hybrid as compared to pristine MWNT. The IR spectra indicates the presence of characteristic peaks within a wavenumber range of 1100–1380 cm^{-1} attributed to C–C stretching band of MWNT (Ahmed et al., 2013). As can be seen, the prominent peaks centred at 1720 cm^{-1} and 1170 cm^{-1} are assigned to C=O and C–O bands, respectively (Lehman et al, 2011). It is noted that the band between 1500-1800 cm^{-1} is attributed to the presence of carboxyl functional groups on the nanotube surfaces (MWNT-COOH) (He et al., 2009). It defines that some carbon double bonds at nanotube walls were oxidized via the mild oxidation treatment (Ahmed et al., 2013; Avile, 2009). While the characteristic peaks at 2380 cm^{-1} are attributed to O–H bending deformation mode from the hydrogen bonds of the carboxyl groups. The other peaks appeared at a wavenumber of 760 cm^{-1} are correspond to –CH_2 rocking. The small peaks centred at 3350 cm^{-1} are attributed to the presence of the hydroxyl (–OH) groups after the removal of water content.

Meanwhile, IR spectra for MWNT-AgNP hybrid (Figs. 4.6(b–e)) show that the transmittance intensity for C–O, C=O, and O–C=O decreases with increasing the volume of Ag precursor ($AgNO_3$). It suggests that the oxygenated groups of functionalized MWNT could serve as the nucleation sites for the reduction of Ag ions (Ag^+). In fact, the deposition of AgNP onto the nanotube surfaces may occur via carboxylic groups, or they physically stick to the surface via Van der Waals forces, weak intermolecular interactions such as π-π stacking and electrostatic attractions (Georgakilas et al., 2007). Thus, C–O–Ag and O=C–O–Ag bonds are formed due to the interactions between carboxyl functional groups and AgNP (Ramin & Taleshi, 2013). The small peaks appeared at 1460 cm^{-1} is attributed to the stretching of C=C bond also due to the interaction of carbon with AgNP. Although the intensity of the C=C bond of pristine MWNT was formerly weakened by nitric acid treatment (Ahmadpoor et al., 2013).

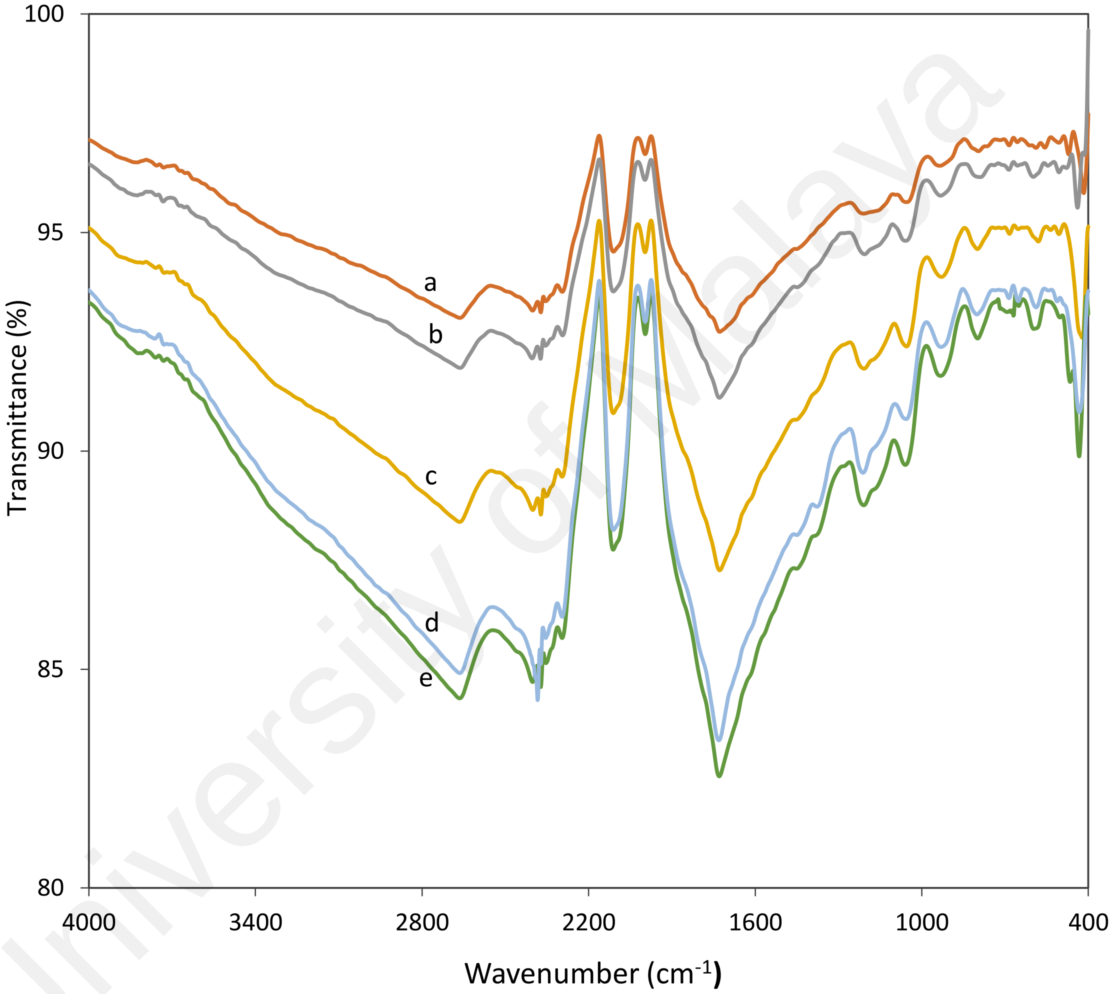

Figure 4.6: FTIR spectra of (a) pristine MWNT and MWNT-AgNP hybrid obtained with different vol. % of $AgNO_3$ (b) 10 (c) 30 (d) 50 and (e) 70.

4.1.3 Raman spectroscopy analysis

The spectral features of pristine MWNT and MWNT-AgNP hybrid are characterized further by Raman Spectroscopy as shown in Figure 4.7(i). It can be seen that there are two prominent features of D-band and G-band appeared at 1340 and 1580 cm^{-1}, respectively. The D-band is attributed to the vibrational mode which originates from the disordered structure of graphite, whereas the G-band is attributed to the tangential radial mode of sp^2 bonded carbon atoms in graphite. It is apparent that the intensity of the D-band is higher than that of the G-band in pristine MWNT, indicating the existence of a more disordered nanotube structures. The D and G-bands of MWNT-AgNP hybrid are broader than pristine MWNT due to the assembly of AgNP at different sizes and distribution that modulating the microenvironment of the MWNT to be more diverse (Yuan et al., 2008). The peaks broadening of MWNT-AgNP hybrid ascribed to the deposition of AgNP allowing the charge-transfer from silver ions to MWNT surface. This interaction is enhanced through hydrophobic interaction with SDS molecules, which cause a substantial change in electronic density state of the nanotubes (Valmalette et al., 2014).

The D to G-band intensity (I_D/I_G) ratio for pristine MWNT was 1.34. Whereas the I_D/I_G value for MWNT-AgNP hybrid was increased with increasing the volume of $AgNO_3$. The increase of D-band intensity is related to the presence of relatively small intensity of D' peaks. It indicates that the deposition of AgNP created some defects such as non-sp^2 carbon dangling bonds in the MWNT structures. As can be seen, there is a shoulder on the right side of the G peak due to the increase of disorder graphite structure. Figure 4.7(ii) shows a linear dependence between I_D/I_G and $I_{D'}/I_G$ ratio. While the I_G is considered as a constant, then the D and D' intensities are found proportionally increased due to some defects created in sp^2 carbon hybridized with AgNP.

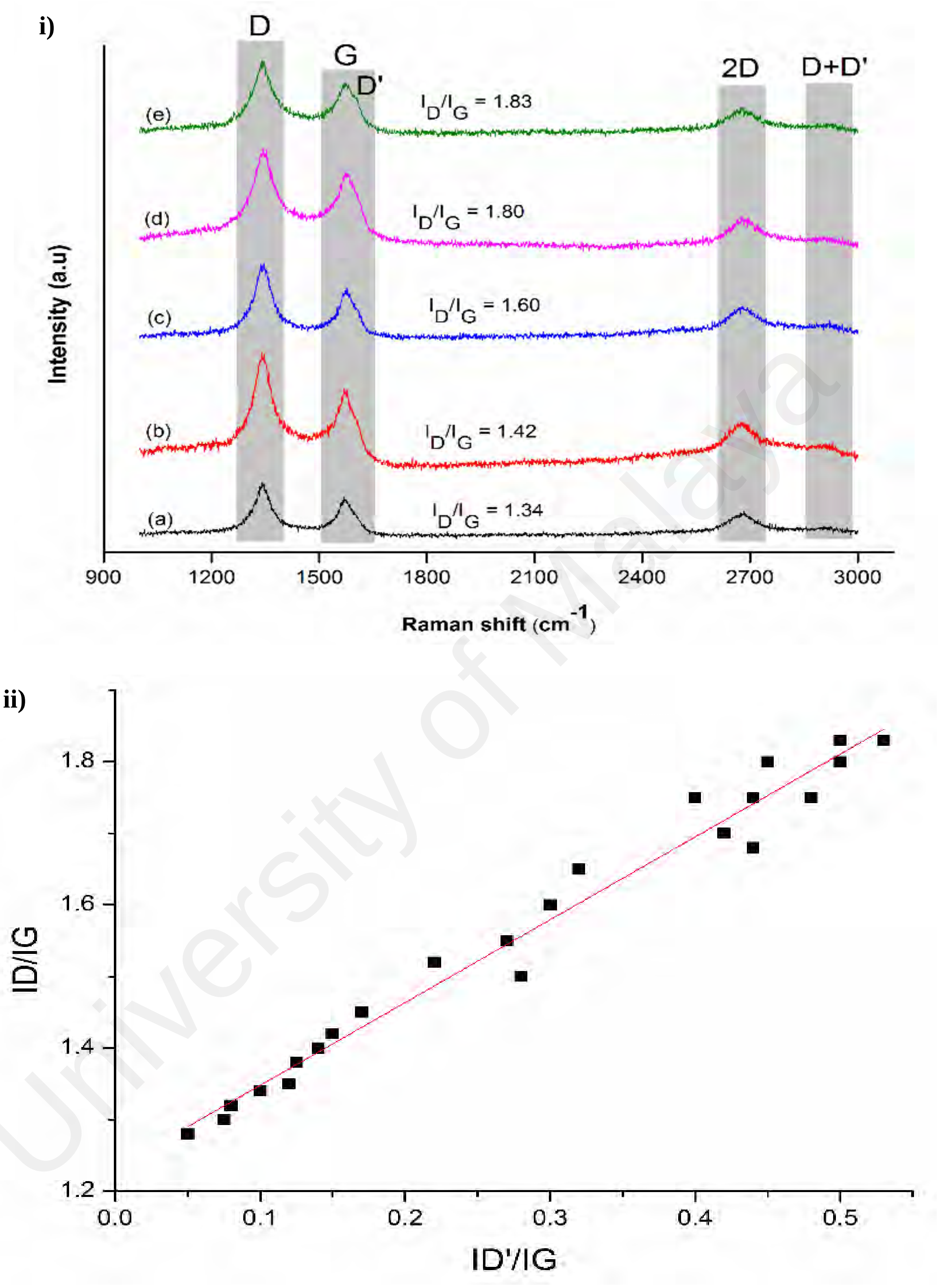

Figure 4.7: (i) Raman spectra of (a) pristine MWNT and MWNT-AgNP hybrid obtained with different vol.% of $AgNO_3$ (b) 10 (c) 30 (d) 50 (e) 70 and (ii) the plotted graph of I_D/I_G versus $I_{D'}/I_G$.

However, the proportionality factor may vary on the different type of defects present in the nanotube structures. This in good agreement with work done by Eckmann et al. (2012) described the nature of defects in graphene by Raman spectroscopy. The presence of G' band or 2D band at 2670 cm^{-1} is due to the two-phonon scattering which is sensitive to the defect density and purity of the MWNT (Vaisman et al., 2006). The intensity of the G'-band also evolves from metallicity enriched within the nanotubes (Kim et al., 2007). The interaction between AgNP and MWNT induced a slight increase in metallicity of the nanotubes. It is because the Ag atom can act as an electron donor when one Ag atom is replacing C atom of a graphene sheet. It also could create an interaction with a few of electronic levels close to the Fermi energy of metallic behaviour (Bittencourt et al., 2007).

4.2 Properties of PVA/MWNT-AgNP nanocomposites

4.2.1 Morphological analysis

Field-emission scanning electron microscopy (FESEM) images in Figure 4.8 reveal surface morphology of the as-synthesized PVA/MWNT-AgNP nanocomposites. The micrographs show microstructural variations of percolating MWNT-AgNP embedded in PVA matrix at different AgNP content. The structure of MWNT seems like much kinked and distributed randomly with high irregular interfaces. Meanwhile AgNP were seen as the bright spherical spots that deposited on the MWNT surfaces. The observed outer diameters of MWNT in the FESEM images are slightly bigger than the TEM size due to polymer wrapping along the nanotube surfaces (Wang, 2007).

Figure 4.8(a) shows poor dispersion of MWNT-AgNP within the nanocomposites where many pores exist between the fillers and the matrix. The lack of fillers distribution caused a weak interfacial interaction at low loading of 0.1 wt% AgNP, which resulted in low dielectric permittivity. There is an improvement in the dispersion of MWNT-AgNP with the increased AgNP content from 0.3 to 1.0 wt% within the nanocomposites (Figure 4.8 (b-c)). It shows that the attachment of AgNP on MWNT surface have reduced van der Waals forces and prevented agglomeration of the nanotubes. The observation is in good agreement with a study showed by Xin and Li (2011). The good distribution of MWNT-AgNP provides high physical interactions between polymer chains and both fillers, which can enhance the structure and electrical properties of the nanocomposites. The MWNT networks serve as the bridges that will facilitate current flow, while AgNP increases the concentration of charge carriers within the nanocomposites. There would be charge transfer complexes (CTC) of MWNT-AgNP in amorphous regions to the semi-crystalline part of the PVA. The transfer of charge carriers occurs with the increased of AgNP content that reducing the potential barrier of the two localized states. (Mahendia et al., 2010, Bhajantri et al., 2007, Chahal et al., 2015).

However, when the AgNP content increased further up to 1.8wt%, inducing large pores and metal clouds exist amongst the MWNT networks (Figure 4.8(d)). The poor fillers distribution was due to segregation of AgNP in some parts that caused high entanglement of the nanotubes. The bundle of MWNT at high concentration of AgNP formed a localized buckles due to the heat and forces applied during the solution-mixing process. This circumstance deteriorates flexibility of the nanocomposites and retards mobility of the charge carriers, leading to undesirable electrical conductivity and dielectric properties.

It is observable that particle sizes vary with the amount of AgNP attached together with MWNT in the nanocomposites. The average size of AgNP in the individual micrograph was around 17 nm, 22 nm, 36 nm and 55 nm as shown in Figure 4.9. It perceives that the size increment of AgNP was due to aggregation and growth of the AgNP clusters caused by the steric effect of metallic nanoparticles (Song et al., 2009). The large molecular chains of PVA have created another complex steric configurations that lead to the aggregation of AgNP within the nanocomposites (Zhang, Smith, & Oyanedel, 2011).

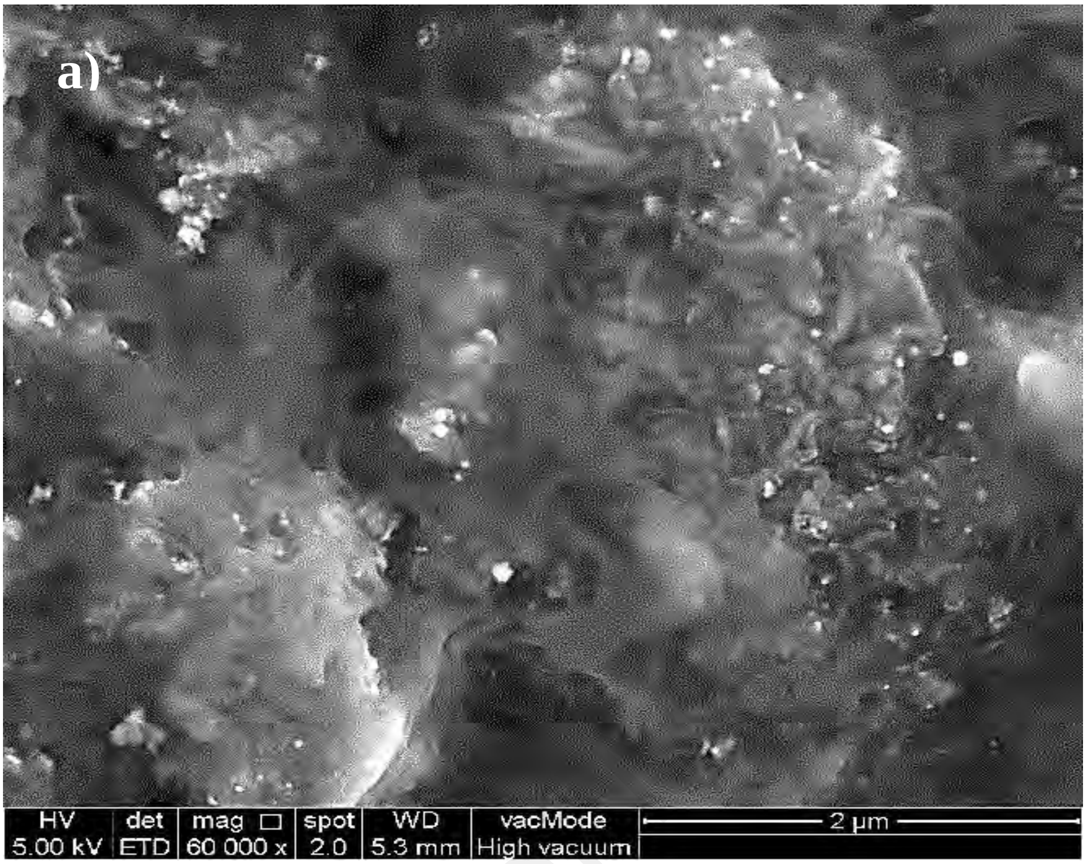
a)
HV
5.00 kV
det
ETD
mag □
60 000 x
spot
2.0
WD
5.3 mm
vacMode
High vacuum
2 µm

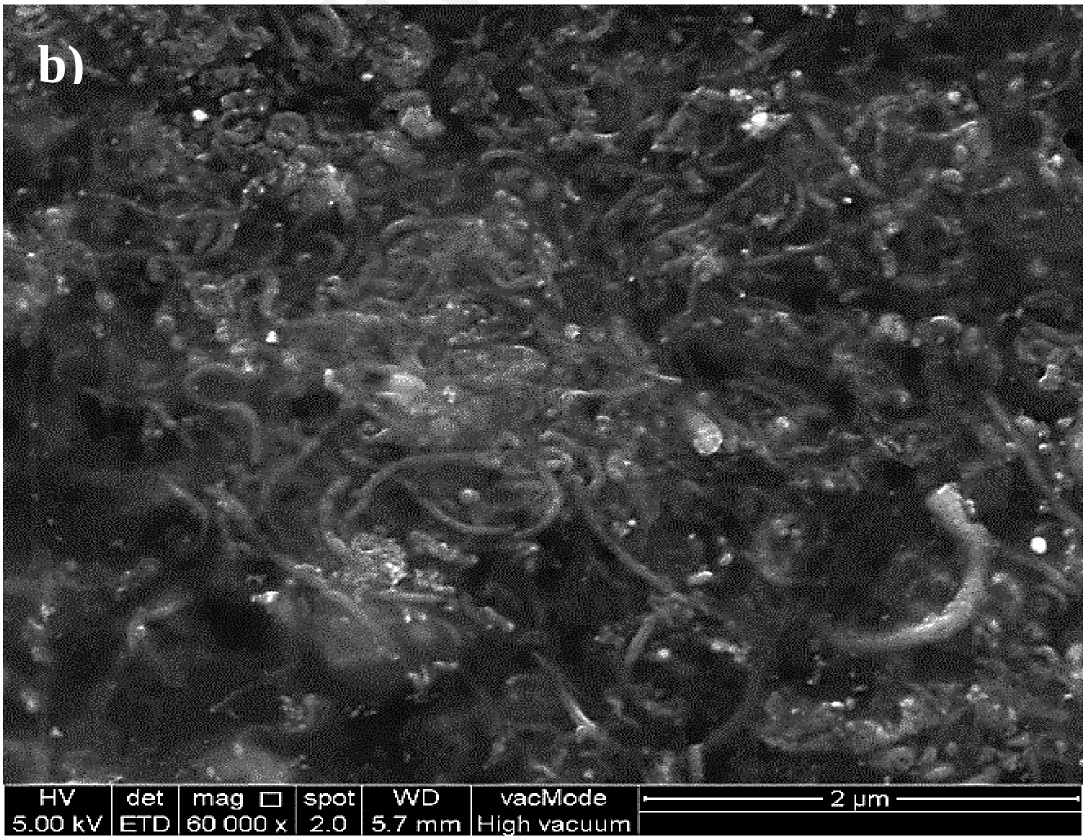
b)
HV
5.00 kV
det
ETD
mag □
60 000 x
spot
2.0
WD
5.7 mm
vacMode
High vacuum
2 µm

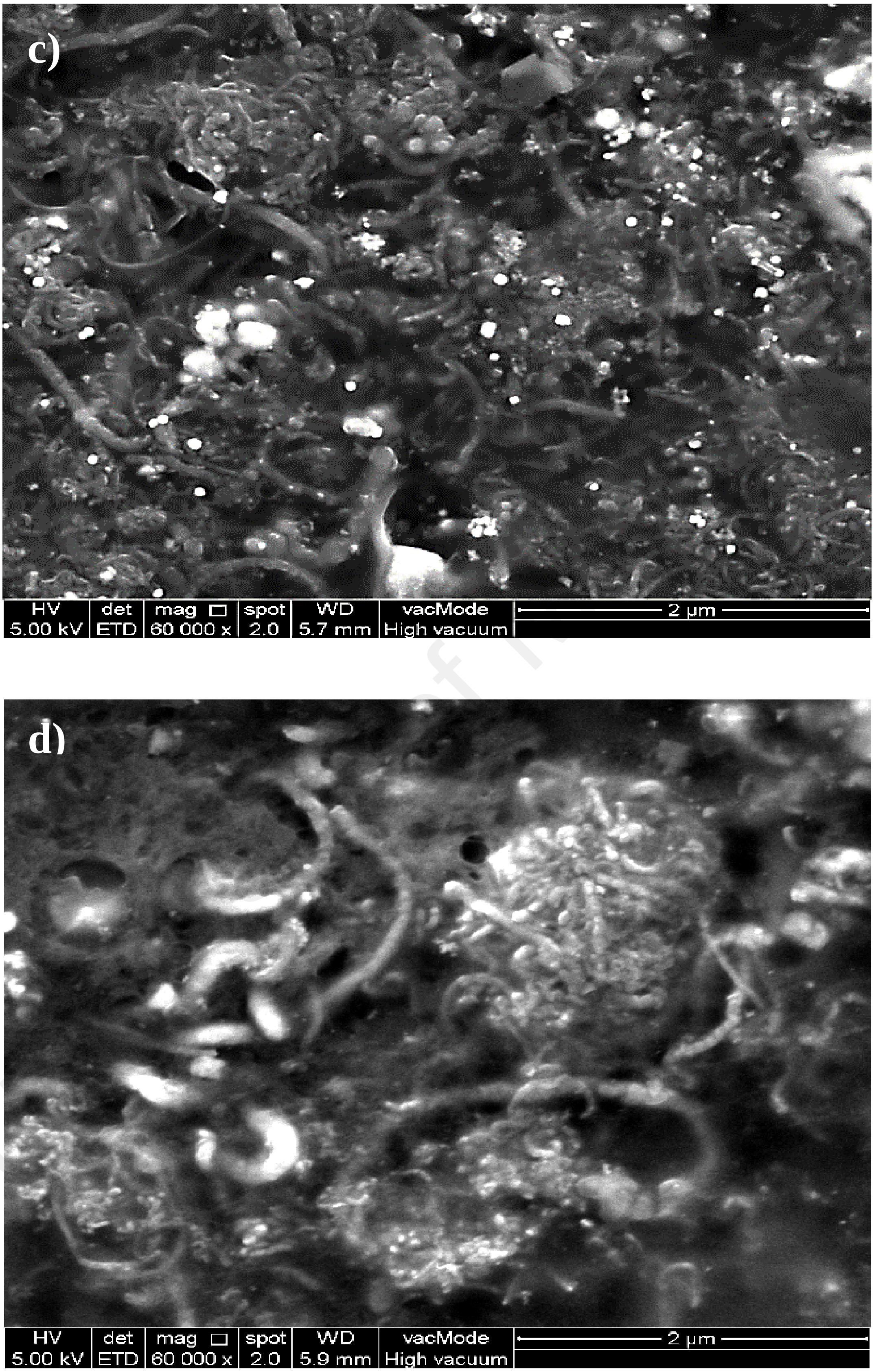

Figure 4.8: FESEM micrographs of the PVA/MWNT-AgNP nanocomposites with different AgNP contents (a) 0.1 wt% (b) 0.3 wt% (c) 1.0 wt% (d) 1.8 wt%.

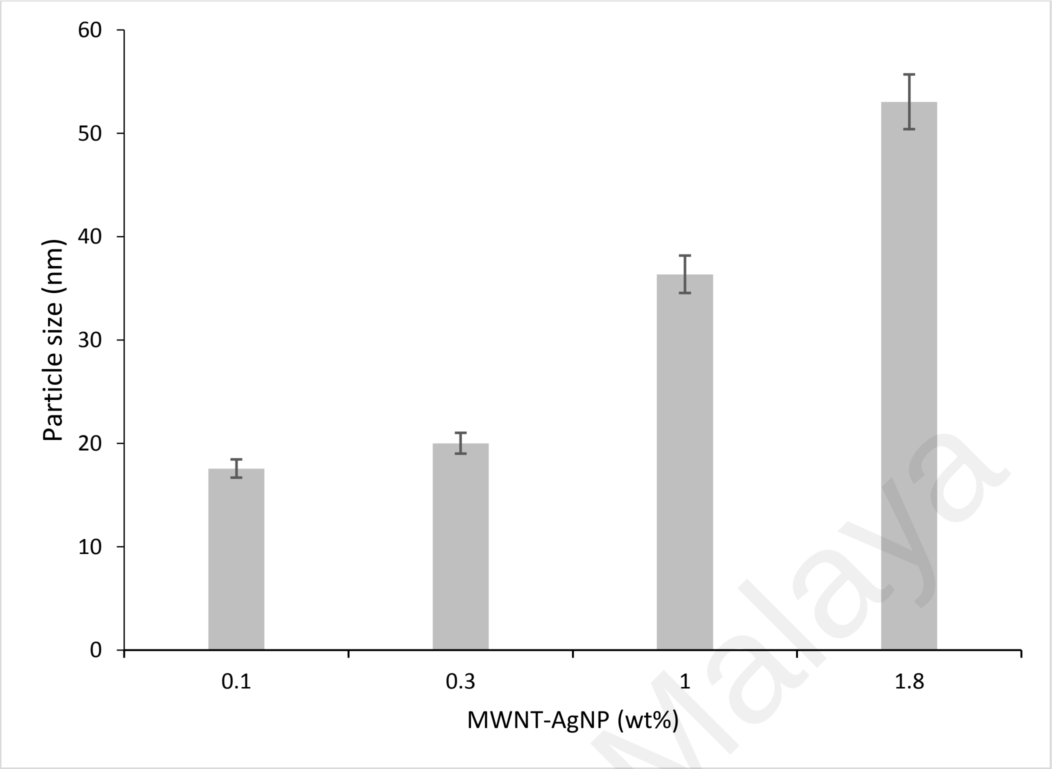

Figure 4.9: Shows the particle size distribution of AgNP for the PVA/MWNT-AgNP nanocomposites at different AgNP loading.

4.2.2 Structural analysis

4.2.2.1 X-Ray Diffraction (XRD) analysis

The structure properties of PVA/MWNT-AgNP nanocomposites with different content of AgNP was confirmed by XRD analysis as shown in Figure 4.10. The XRD profile describes the structure and phase composition of MWNT-AgNP embedded within the matrix. Figure 4.10 (a) shows a broad diffraction peak at $2\theta = 19.2°$ and a shoulder at $2\theta = 23.0°$, which corresponds to the micro-crystalline structure and the reflection plane (101) of pure PVA. While in Figure 4.10(b) shows the XRD pattern of PVA/MWNT nanocomposite with a new peak appeared at $2\theta = 26.3°$ that corresponds to a typical (002) plane of the MWNT. Meanwhile the XRD patterns for PVA/MWNT-

AgNP nanocomposites (Figure 4.10 (c-f)) show additional intense peaks located at 2θ = 38.1°, 44.3°, 64.5° and 77.4° are assigned to the reflections of Ag crystallographic planes (111), (200), (220) and (311), respectively (Larrude, Maia, & Jr, 2014). The interplanar distance, d_{hkl} value corresponds to the Ag planes possessing a face-centred cubic [FCC] structure was determined in accordance to Bragg's law is 0.236 nm, 0.204 nm, 0.144 nm and 0.123 nm Whereas the d_{hkl} for (002) plane of MWNT is 0.341nm. The values are consistent with the lattice fringes observed using high-resolution transmission electron microscopy. The average lattice constant (a) of the AgNP was 0.410 nm, which is in good agreement with the standard value [Silver file no. 01-087-0717]. This XRD spectra confirms the presence of polycrystalline AgNP in the nanocomposite structures.

The width and intensity of the peak at 2θ = 19.2° decreases with increasing AgNP content due to the increased in crystallite size of PVA. This correlation is conforming to Scherer formula where the crystallite size is inversely proportional to the total broadening of diffraction peak (Cullity, 1978). The crystallization of PVA is favoured due to high hydrolysis degree of the polymer containing much hydroxyl groups that can provide more intermolecular interactions with the fillers (Van Etten et al., 2014). It seems that the crystallite size of AgNP decreased by the broadening of peak-width at high concentration of AgNP. Even though, the crystallite size is not representing the exact particles size of AgNP. The measured particle sizes of AgNP in previous morphological analysis could be made up of numerous aggregated crystallites. At 0.1 wt% of AgNP, the size of AgNP particles seems to deliberate amorphous structure below 3 nm, but it turned out to be well crystallized when the particle size increased to 40 nm at a higher AgNP content (Qi et al, 2005).

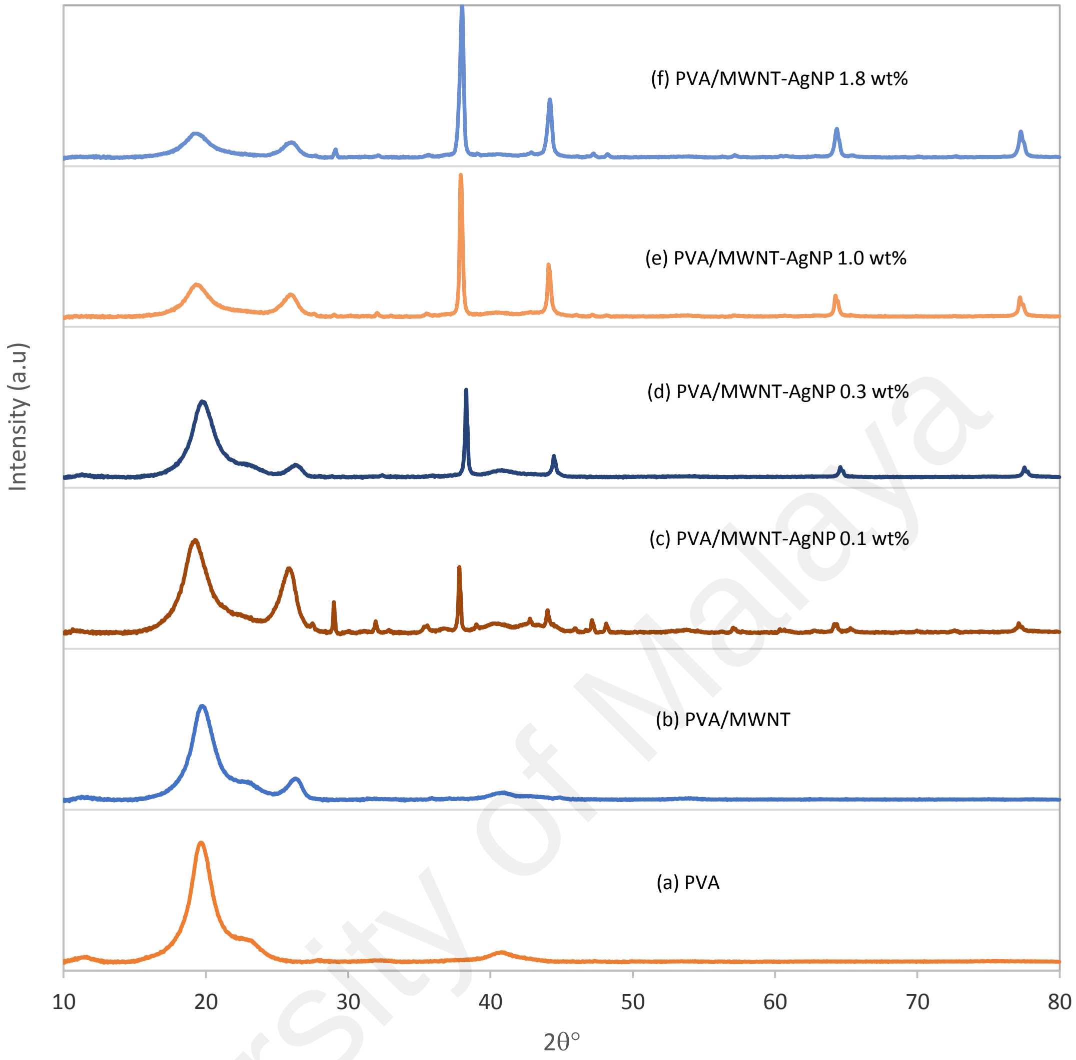

Figure 4.10: XRD patterns of PVA/MWNT-AgNP nanocomposites at different AgNP contents.

4.2.2.2 FTIR spectroscopy analysis

Figure 4.11 presents the FTIR spectra for PVA, PVA/MWNT and PVA/MWNT-AgNP nanocomposites in the wavenumber range of 400–4000 cm^{-1}. The spectrum of PVA in Figure 4.11(a) shows a prominent broad peak between 3000 and 3500 cm^{-1} corresponds to O-H stretching in the alcohol groups, whereas a weak peak at 2916 cm^{-1} corresponds to C-H stretching vibration. Other characteristics peaks appeared within the range of 500-1400 cm^{-1} corresponds to the C–O vibrations at 1090 cm^{-1} and the coupling of O-H vibrations with C-H wagging at 1420-1322 cm^{-1}. A broad band from 570-720 cm^{-1} is due to the out of plane vibration of O-H, while the peak appeared at 836 cm^{-1} is assigned to out-of-plane vibration of the C-H groups in skeleton bands of PVA at the fingerprint region (Mbhele et al., 2003, Khanna et al., 2005, Saat & Johan, 2014).

The spectrum of PVA/MWNT in Figure 4.11(b) shows a broader and strong O–H stretching band due to formation of hydrogen bond with hydroxyl group and absorption of moisture in the PVA. There is observable changes in peak intensity at 2916 cm^{-1} and a new characteristic peak split at 2850 cm^{-1} due to interaction between MWNT and C-H stretching of the PVA backbone. The band apparent at 1600 cm^{-1} corresponds to C=O stretch indicating the presence of carboxyl group at the MWNT surface grafted on the matrix PVA. It can be seen that the C-H plane vibration band at 836 cm^{-1} was shifted to 820 cm^{-1} due to interaction of open pi-bonds of MWNT with PVA bands (Malikov et al., 2014, Alghunaim, 2016).

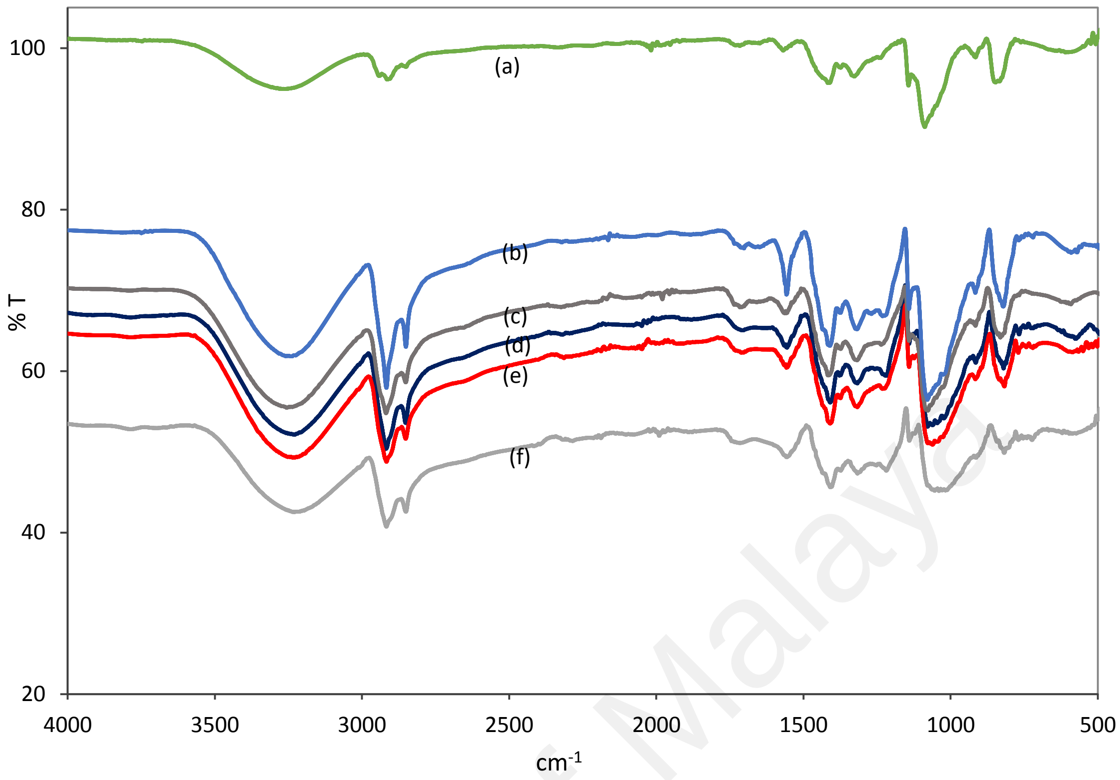

Figure 4.11: FTIR of the (a) PVA, (b) PVA/MWNT and PVA/MWNT-AgNP nanocomposites containing different AgNP content (c) 0.1 wt% (d) 0.3 wt% (e) 1.0 wt% (f) 1.8 wt%.

Meanwhile, the FTIR spectra of PVA/MWNT-AgNP nanocomposites with different AgNP contents are shown in Figure 4.11 (c-f). Based on the spectra, it shows that the incorporation of MWNT-AgNP in PVA leads to a major decrease in the transmittance intensity of several bands with the increase in AgNP content. It can be seen for the bands at 3000-3500 cm^{-1}, and 570-720 cm^{-1} are weakened due to interaction between AgNP and MWNT with different surroundings of O-H groups. The split peaks between 1096 and 1140 cm^{-1} are correspond to C=O, C-C and C-O-C stretching vibration, which shows the presence of embedded AgNP to backbone or side chains of PVA (Chahal et al., 2015). The incorporation of the AgNP also decreased the plane vibration of C-H groups at the band 820 cm^{-1}, while small peak at 917 cm^{-1} was diminished with increasing AgNP concentration due to the inhibited CH_2 rocking of the PVA chains. The decrease in ratio intensity of the peaks between 1420 cm^{-1} and 1322 cm^{-1} corresponds to decoupling vibrations of O-H plane and C-H wagging because of the interaction between AgNP with the O-H groups. This is in agreement with the observation found in others work (Mbhele, 2003, Khanna et al., 2005, Mahendia et al., 2011). In this case, there is a significant decrease in intensity at 1600 cm^{-1} due to the interaction of AgNP with carboxyl groups (O=C–O–Ag) at the MWNT surface. The overall FTIR spectral are much respond to the interaction between PVA matrix and both fillers. Thereby the pronounced effects of MWNT-AgNP content in the nanocomposites can be discussed further by thermal analysis.

4.2.3 Thermogravimetric analysis

The TGA thermogram in Figure 4.12(a) shows thermal analysis and decomposition behavior of pure PVA, PVA/MWNT and PVA/MWNT-AgNP nanocomposites by observing the mass changes as a function of temperature that subjected to heating process. In air atmosphere, the samples demonstrates multistep decomposition at temperatures in the range of 30°C to 600°C. In this figure, all samples have an initial weight loss occurred from 100-200°C due to elimination of water and low molecular organic components. PVA shows main steps of weight loss begin at 280°C until complete decomposition at 550°C due to the decomposition of high molecular weight organic compounds. The weight loss of PVA at elevated temperatures was attributed to pyrolysis process involving the loss of isobutyl groups, backbone fragments and charcoals (Kareem & Kaliani, 2011). PVA/MWNT nanocomposite exhibits almost identical TGA curve where the remaining residue corresponds to the oxidized MWNT and small fraction of SDS that used as surfactant in the composite system. Though, it was reported that pristine CNT could be burned completely and undergo total loss in the TGA curve under air atmosphere (Basiuk et al., 2009).

Meanwhile the addition of MWNT-AgNP provides a pronounced effect on the thermal behavior as compared to pure PVA. It seems that the onset decomposition temperature of the nanocomposites was shifted from 280 to 300°C as compared to PVA. The decomposition profile of PVA/MWNT-AgNP nanocomposites shows four main steps of weight loss begin at 300°C (64% loss), 350°C (30% loss), 450°C (8% loss) and 550°C (40-50% loss). The weight residues obtained around 6-10 wt% was due to the remaining amount of oxidized MWNT and different AgNP content in the nanocomposites. It is notable that the formation of silver oxide would occur during the TGA test under the presence of oxygen, which later decomposed again above 300 °C into silver and oxygen. This is because Ag is an effective oxidation catalyst to split oxygen molecules into atoms that could create sites for the oxidation of oncoming chemical compounds (Herley & Prout, 1960; Alimohammadi et al., 2012).

The peaks temperature of weight loss curve can be determined from the differential thermal gravimetric (DTG) analysis as shown in Figure 4.12(b). It is observable that the presence of MWNT with an increase in the AgNP content caused the oxidation peaks at 430 °C and 510 °C were shifted to 460 °C and 550 °C, respectively. A complete decomposition of the nanocomposites only takes place at a higher temperature than pure PVA by about 30-40 °C. It is consistent with the observation in others work (Khanna et al., 2005). It denotes that the inclusion of MWNT-AgNP improved thermal stability of the nanocomposite due to lower degradation rate when the chain transfer reaction was suppressed by the decrease in mobility of the PVA chains (Mbhele et al., 2003).

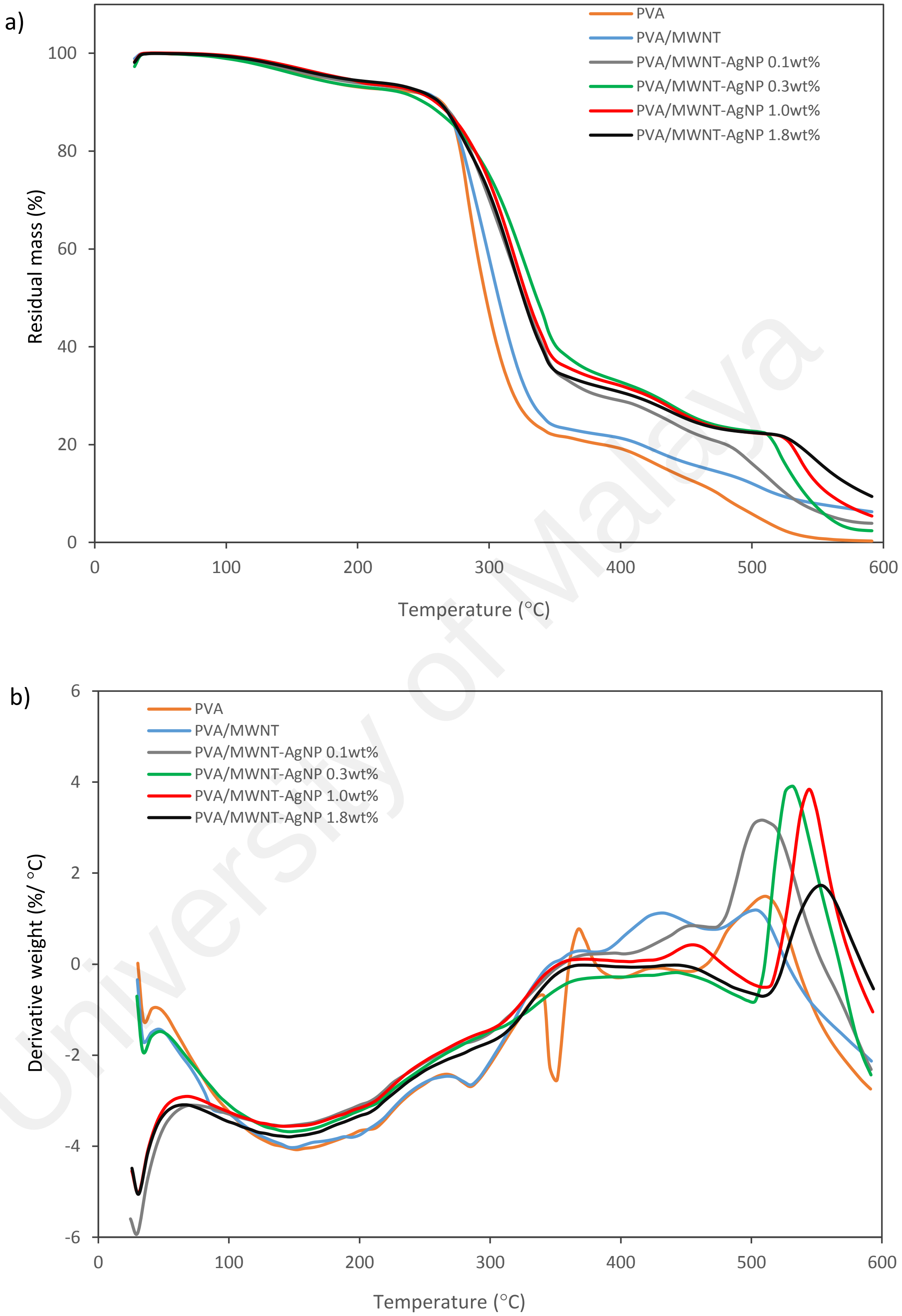

Figure 4.12: (a) Thermal gravimetric analysis (TGA) and (b) Differential thermal gravimetric (DTG) curves of PVA/MWNT-AgNP nanocomposites in air atmosphere.

4.2.4 UV-Vis spectroscopy analysis

Figure 4.13 shows the ultraviolet-visible (UV-Vis) spectra of the PVA/MWNT-AgNP nanocomposites. There is no absorption profile of pure PVA while PVA/MWNT nanocomposite (Figure 4.13a-b) displays broad peak at 254 nm. This is attributed to the absorption of black coloured MWNT arise from the π-π* transitions of the aromatic C-C bonds (Paredes et al., 2008). Meanwhile, PVA/MWNT-AgNP nanocomposites show more pronounced and asymmetrical absorption peaks in the range of 250 nm to 800 nm (Figure 4.13(c-f)). It is observable that the absorption peak at 254 nm was red-shifted to 262 nm with the increased of AgNP content in the nanocomposites. This because the presence of AgNP in the nanocomposites has influenced the absorption properties of MWNT to be shifted towards a longer wavelength. The absorption peak is followed by a weak shoulder appeared at 350 nm due to multiple AgNP transitions with increasing particles sizes (Bhui et al., 2009, Li & Liu, 2010). The width of absorption peaks become narrow with the increased content of AgNP especially at 1.0 wt% of AgNP. This indicates a preferential scattering of larger crystallites due to the interconnection of Ag nanoclusters during deposition process within the matrix. It was reported that the absorption profile was influenced by the dielectric effective constant of surrounding medium (Mulvaney, 1996). However, the surface plasmon resonance (SPR) of AgNP could not be seen around 420 nm due to no electronic interaction at ground state since the charge transfer from AgNP to the MWNT has decreased the electron density of the metal core (Henglein, 2001; Feng et al., 2010). The same observation was found by Zhang et al. (2016). The overall UV-vis spectra demonstrates a positive correlation with FESEM images, wherein the redshift of absorption peaks was ascribed to the charge transfer process of MWNT-AgNP embedded within the nanocomposites

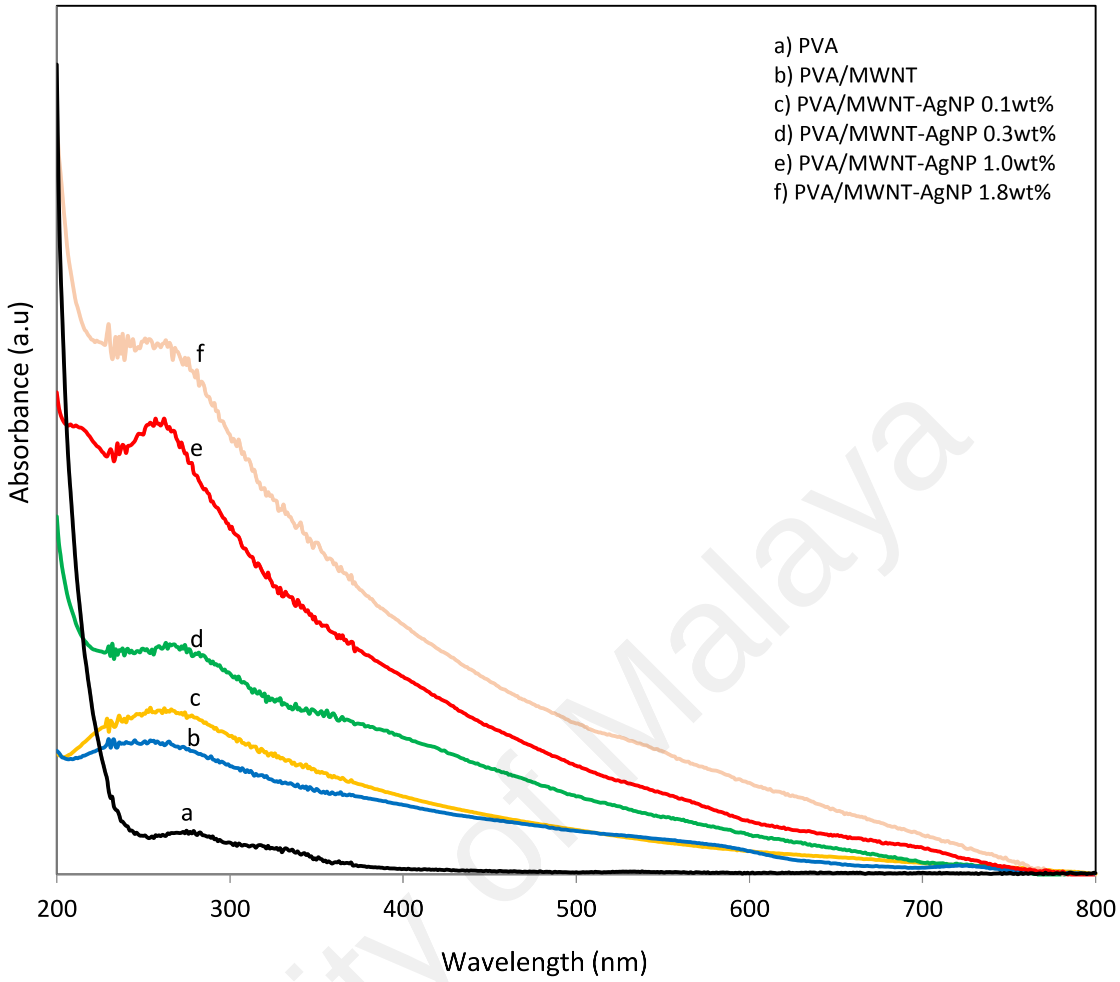

Figure 4.13: UV-vis absorption spectra of PVA/MWNT-AgNP nanocomposites at different content of AgNP.

4.2.5 Electrical and dielectric spectroscopy analysis

4.2.5.1 I-V characteristics

Electrical characteristics of PVA and PVA/MWNT-AgNP nanocomposites with different AgNP contents are shown by the graphs of current, *I* against potential difference, *V* as shown in Figure 4.14. As seen in the graphs, the current flow of pure PVA did not change with the applied voltage due to insulating property of the polymer. Meanwhile, PVA/MWNT-AgNP nanocomposites with increasing AgNP contents exhibit nonlinear *I-V* relationship as the current increases exponentially with the applied voltage. Likewise, Das and co-workers (2015) have revealed a similar symmetrical *I-V* behavior of merely PVA/MWNT at a reverse voltage. In this result, the inclusion of 0.1 wt% AgNP did not significantly change electrical behavior of the PVA/MWNT. It causes current flow of the nanocomposites remain close to the range of pure PVA. It arises due Coulomb blockade effect that might come from single-tunneling knots of nanoparticles that preventing charge carriers from moving at a voltage and thus preserving the insulating property of the polymer (Saini et al., 2013).

However, there is a sudden increase in the current flow above 0.3 wt% of AgNP, indicating the onset of space charge limited conduction that leads to substantial increase of gradient from the graph. It is also directly proportional to a higher conductivity of PVA/MWNT-AgNP nanocomposites. As seen, the *I-V* curves for MWNT-Ag hybrid were shifted at lower 'knee voltage' of 0.8 V at the highest loading of AgNP. It shows that the presence of AgNP and MWNT together in the matrix could reduce the contact resistance and improve electrical conductivity of the nanocomposites (Table 4.1). It suggests that bringing sufficient amount of AgNP into contact with MWNT has prompted a behaviour of p-n diode by allowing charge transfer when the current flow only occurs through outermost of the nanotubes (Bandaru, 2007).

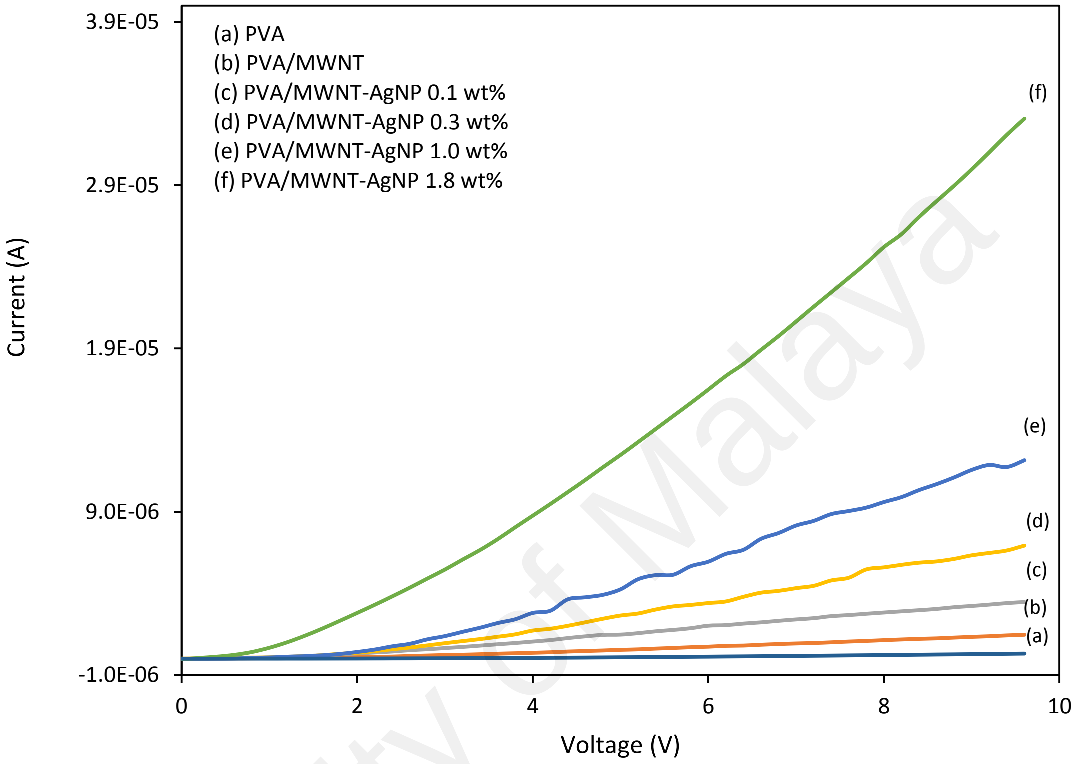

Figure 4.14: The I-V curves for PVA/MWNT-AgNP nanocomposites with different content of AgNP.

Table 4.1: Electrical resistance and dc-conductivity determined from the *I-V* curves.

	Samples	**Resistance (Ω)**	**Dc-conductivity (S/m)**
a)	PVA	3.33 x 10^7	1.71 x 10^{-8}
b)	PVA/MWNT	5.00 x 10^6	1.43 x 10^{-7}
c)	PVA/MWNT-AgNP 0.1wt%	2.50 x 10^6	2.85 x 10^{-7}
d)	PVA/MWNT-AgNP 0.3wt%	1.25 x 10^6	5.70 x 10^{-7}
e)	PVA/MWNT-AgNP 1.0wt%	1.00 x 10^6	7.13 x 10^{-7}
f)	PVA/MWNT-AgNP 1.8wt%	2.50 x 10^5	2.85 x 10^{-6}

4.2.5.2 Impedance spectroscopic analysis

Electrical impedance is another measure of effective resistance to alternating current (ac) in an electric circuit. Figure 4.15 shows the dependence of impedance on the applied frequency of the PVA/MWNT-AgNP nanocomposites. It shows the decreasing trend of the impedance values from low to high frequency. It is observed that the impedance values also decreases as the content of AgNP decorated onto MWNT increases, leading to the enhanced electrical transport of the nanocomposites This trend is due to high interfacial polarization arising from heterogeneity of both filler and the matrix (Elimat, Al-Hussami, & Zihlif, 2012).

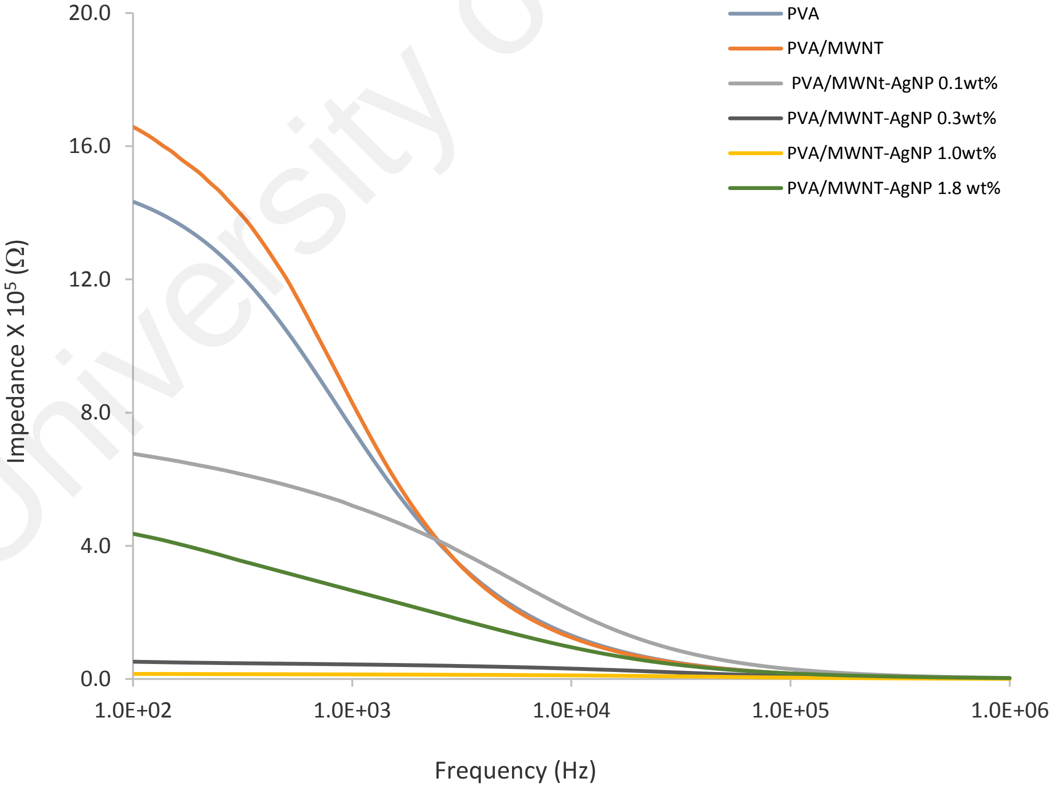

Figure 4.15: The variance of impedance versus frequency for PVA/MWNT-AgNP nanocomposites at different AgNP content.

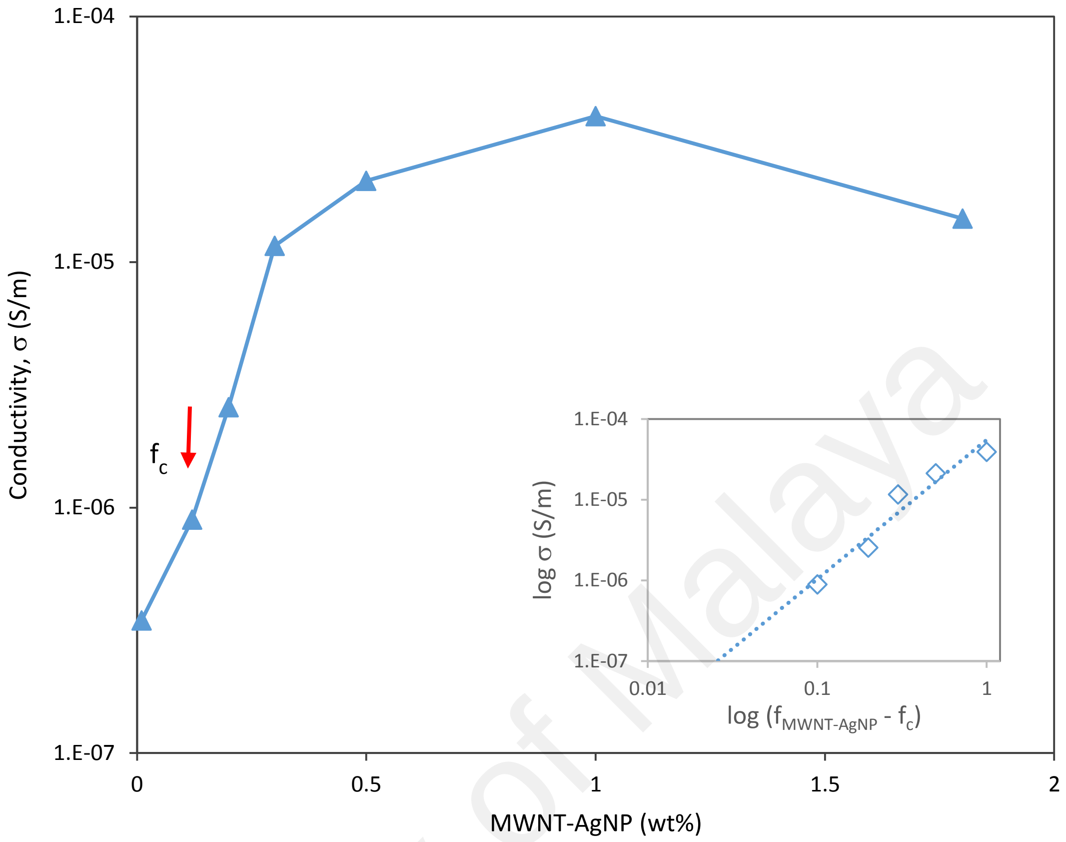

Figure 4.16: The plots of electrical conductivity versus MWNT-AgNP content of the PVA/MWNT-AgNP nanocomposites. The inset shows the best fit to log-log plot of the conductivity data.

Figure 4.16 shows a non-linear increasing trend of the ac conductivity with the increase of AgNP content in the nanocomposites measured at the frequency of 100 Hz. The conductivity of the nanocomposites were increased by two orders of magnitude compared to pure PVA, which strongly depend on the AgNP content above a critical fillers loading known as percolation threshold. The percolation theory describes electrical conductivity, σ and permittivity, ε of nanocomposites are varies with fillers content by power-laws as shown in the following relations (Dang et al., 2012: Zhang et al., 2009):

$$\sigma \propto (f - f_c)^t \qquad \text{for } f > f_c \tag{4.1a}$$

$$\sigma \propto (f_c - f)^q \qquad \text{for } f < f_c \tag{4.1b}$$

$$\varepsilon \propto (f_c - f)^{-q} \qquad \text{for } f < f_c \tag{4.1c}$$

where f is the content of conductive fillers, f_c is the percolation threshold, t is the critical exponent of conducting region and q is the dielectric exponent of insulating region. Based on Figure 4.16, the estimated values of f_c and t can be obtained by fitting the data in Eq. 4.1a using least square fit. An inset shows the best linear fit to the log-log plots of the conductivity power laws, which gives $f_c = 0.15$ wt% and $t = 1.70 \pm 0.10$. The attained value of the critical exponent, t is in good agreement with the universal value ($t \approx 1.6$-2.0) (Dang et al., 2012), which denotes morphology of the percolating MWNT-AgNP network.

Figure 4.17 shows the ac conductivity, σ_{ac} of the nanocomposites with different AgNP content is invariant at a lower frequency, and gradually increases at a higher frequency by power-law behaviour. It can be seen that the σ_{ac} plateau response of PVA ended towards higher frequency with increasing AgNP content in the nanocomposites. Here, the conductivity is remained due to the electrons easily move through infinite clusters of conductive networks. The electrical conduction occurred through numerous conductive pathways since the MWNT and AgNP are in good contact, leading to the efficient mechanism of electron hopping in localized states (Chen et al., 2015). However, there are limited percolating pathways below the threshold value, which resulted in low conductivity of the nanocomposites.

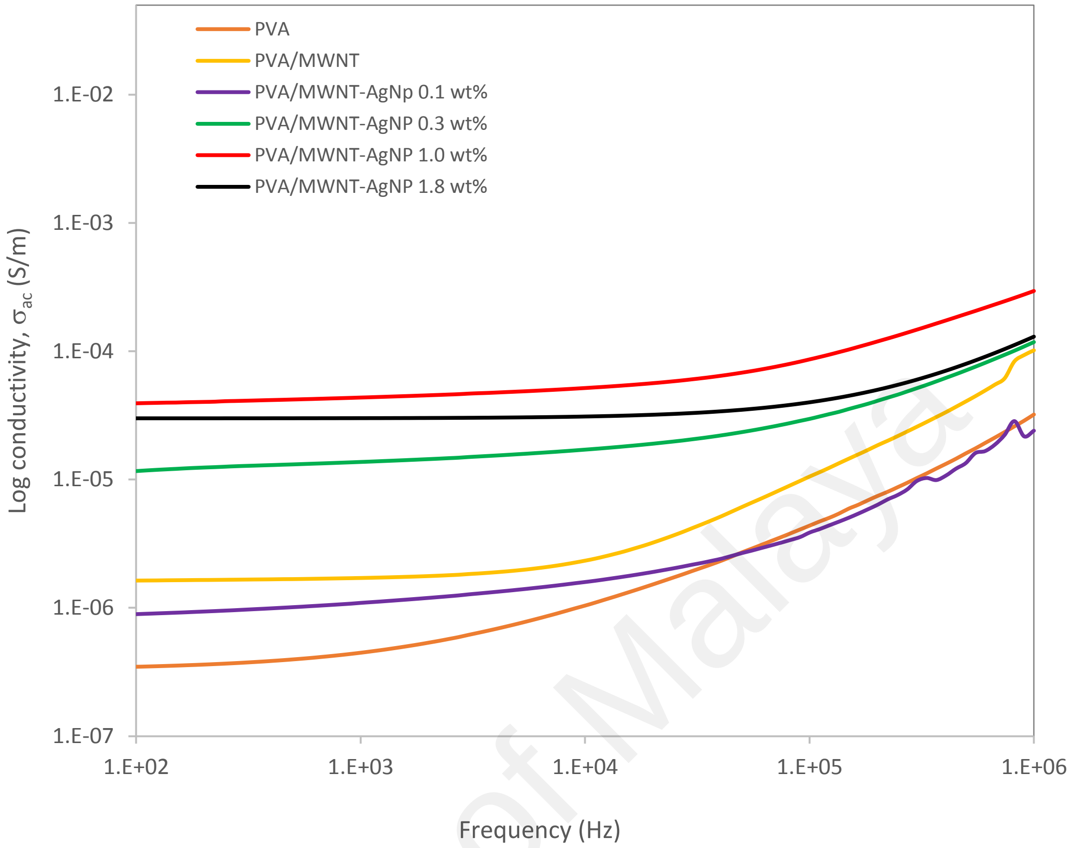

Figure 4.17: The dependence of ac conductivity on frequency for the PVA/MWNT-AgNP nanocomposites with different AgNP content.

Figure 4.18(a) shows the non-linear increasing trend of dielectric permittivity, ε′ of the PVA/MWNT-AgNP nanocomposites. It indicates that the addition of AgNP was not only improved the conductivity, but also induced polarization in the nanocomposites which lead to an increase in the dielectric permittivity. The increased conductivity was associated with a large increment of dielectric permittivity near the percolation threshold due to the divergence of both insulating and conducting sides. The ε′ values of the nanocomposites was increased substantially above the percolation threshold at the maximum value of 600, which is about 60 times higher than pure PVA.

For comparison, this increment is also nearly 20 times higher than PVA/MWNT (Zhang et al., 2009). However, the ε′ values are decreased at 1.8 wt% with a further loading of AgNP. The dielectric permittivity was initiated from MWNT π-orbital that provides a large field for moving electrons to be easily polarized (Dang et al., 2007). The charge carrier concentration was increased by incorporating AgNP, which induced more polar groups into the polymer chains. The presence of AgNP also can reduce the ohmic resistance between the nanotubes and induced the charge carriers (electrons or holes) by injection or ejection of electrons in the valence or conduction bands (W. Zhao et al., 2010). Thereby, it prompts the nanocomposites to be more conductive with high dielectric permittivity.

As seen in Figure 4.18(b), it shows the dependence of dielectric permittivity on frequency of the PVA/MWNT-AgNP nanocomposites at different AgNP content. High ε′ values are observed at low frequency due to the dipoles in polymer nanocomposites have a strong tendency to orient themselves in the direction of an applied field (Ray, Himanshu, & Sinha, 2005). The ε′ values then gradually decreased with increasing frequency due to the relaxation process of the oriented polarization. Primarily, the ε′ value of PVA exhibits a weak frequency dependence since the polarization depends on the freedom of chain movement attributed to hydroxyl groups as eternal dipoles in the polymer chains (Van Etten et al., 2014). Meanwhile, PVA/MWNT nanocomposite only shows a slight increment in the ε′ value with increasing frequency when compared to the pure PVA. This is in good agreement with Zhen et al. (2013), who claimed the weak frequency dependence of polymer nanocomposites filled by less than 5 wt% of MWNT.

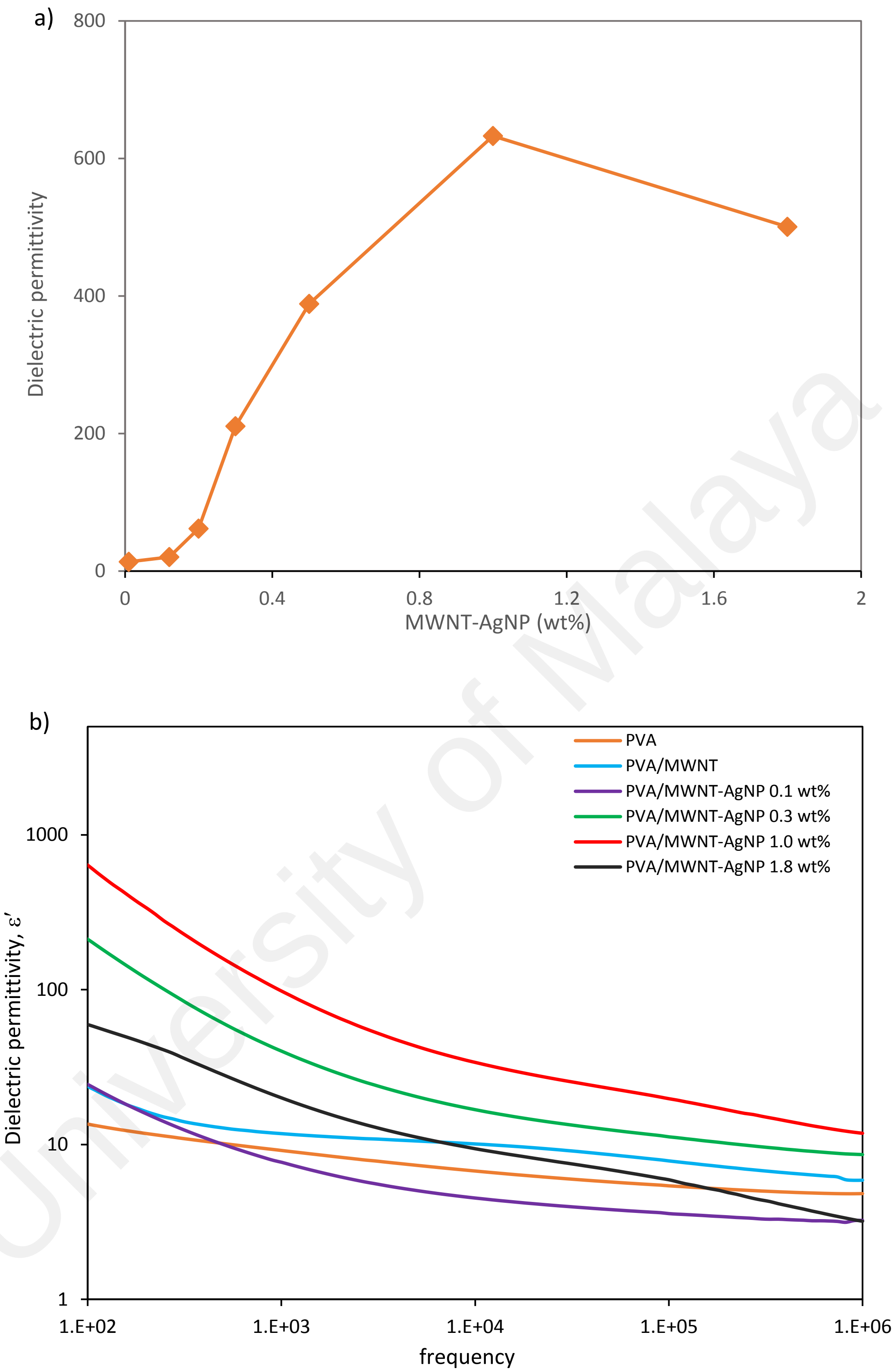

Figure 4.18: (a) The dielectric permittivity versus MWNT-AgNP of the PVA nanocomposites measured at 100 Hz; (b) The dependence of dielectric permittivity on frequency for the PVA/MWNT-AgNP nanocomposites.

Though, there was a drastic change above the percolation threshold with increasing slope of the ε′ curves when AgNP content increased from 0.3 to 1.0 w, which gradually decreases as the frequency increases from 10^2 to 10^6 Hz. The increased of dielectric permittivity with increasing AgNP was due to the piling of charges at the extended interfaces (Lu et al., 2006). This is ascribed to the strong interfacial polarization between matrix and MWNT-AgNP because of their differences in conductivity and polarizability. However, the ε′ values were slightly reduced with a further loading of AgNP up to 1.8 wt% due to less mobility of the charge carriers and lack segmental motion of the polymer. The dielectric relaxation takes place with increasing frequency when the percolating network become closer to each other, which later dominated by the matrix when many of the MWNT-AgNP were blocked by PVA layers. This is because PVA is a polar polymer where the dipoles entrap the electrons, while interfacial polarization lead to the formation of large dipoles on the metal particles (Bhajantri et al., 2007). Besides, the dielectric behaviour of nanocomposites also depends on several factors such as electrode effect, orientation, atomic and electronic polarization (Sreekumar et al., 2012).

Figure 4.19 shows dielectric loss, ε″ of the nanocomposites exhibit a decreasing trend with an increase of frequency. The dielectric loss is due to the energy loss associated with charges motion and dipoles alignment Once the induced charges are unable to follow the periodic reversal of electric field that is extremely fast at high frequency, it triggers the decrease in ε″ values with a decline of the charges accumulation (Senthil et al., 2012). The features display large dielectric loss of the nanocomposites with increasing AgNP content, which is inversely proportional to the frequency and gradually decreased towards a higher frequency. The addition of AgNP resulted in greater ε″ values compared to the pure PVA and PVA/MWNT nanocomposites. The significant increase in the ε′′ values is associated with improved electrical conductivity by tuning the insulator to conductor transition of the nanocomposites. However, the dielectric loss was minor below the percolation threshold due to low loading of AgNP. It is ascribed to Coulomb blockade phenomenon which arises from single electron effect of isolated nanoparticles distributed in a definite space within the nanocomposites. This caused many tunneling knots that prevent mobility of the electrons/charge carriers in a certain electric field (Saini et al., 2013).

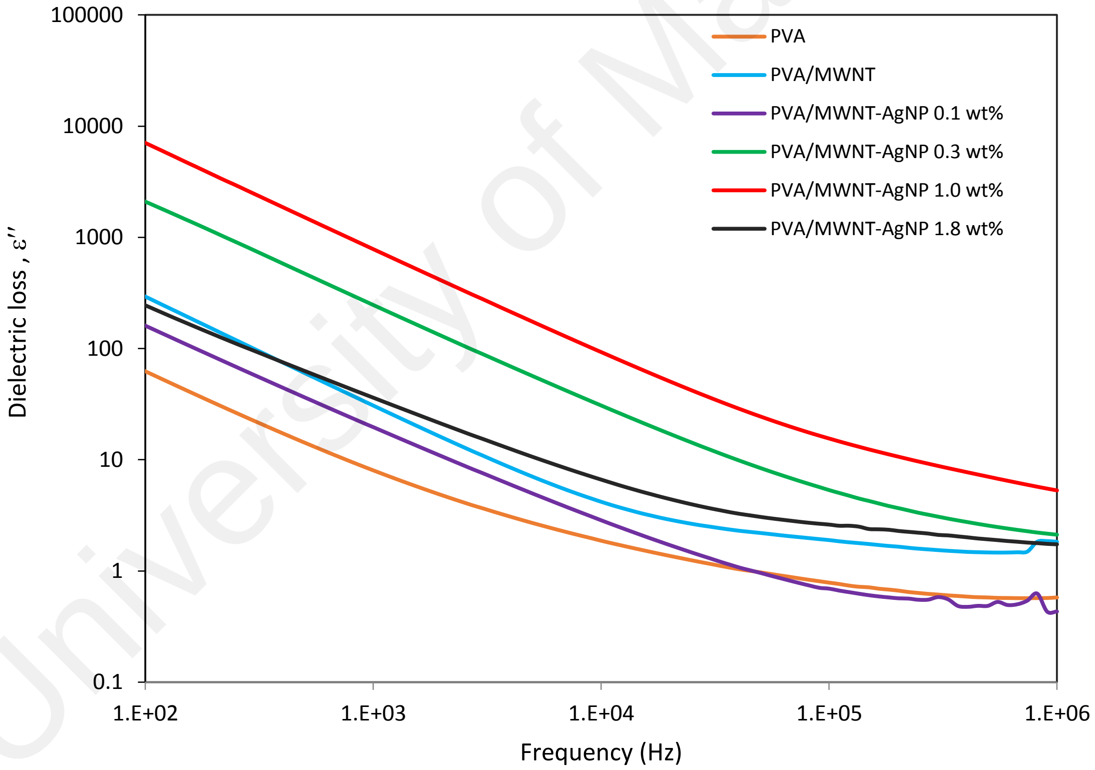

Figure 4.19: The dependence of dielectric loss on frequency for the PVA/MWNT-AgNP nanocomposites with different AgNP content.

Figure 4.20 (a-b) illustrate the frequency dependence of the real (M′) and imaginary part (M″) of the nanocomposites.A complex dielectric modulus (M^*=M′+iM″) is used to predict dielectric relaxation when electric displacement remains constant due to space charge polarization (Sengwa, Choudhary & Sankhla, 2008; Ioannou, Patsidis & Psarras, 2011). The M′ values initially were almost approaching zero at a lower frequency due to electrode polarization, and getting increased towards higher frequency (Dutta, Biswas, & De Kumar, 2002; Migahed et al, 2004). Meanwhile, M″ shows an asymmetric spectra that represents relaxation frequency of the nanocomposites. The M″ spectra elucidate mobility of the charge carriers with increasing the frequency. The charge carriers travelling over long distances at low frequency and upon reaching the maximum M″, their mobility is executed to localized motion over short distances. The peaks of M″ defines relaxation time, τ of the orientated dipoles ($\tau = 1/\ \omega_p$), where the angular frequency is given by $\omega_p = 2\pi f$ (Senthil et al., 2012). It can be seen that the relaxation frequency of the nanocomposites shifted towards higher frequency and the relaxation time was reduced with the increased of AgNP. It denotes high mobility of the charge carriers to transfer from one site to neighboring sites in a shorter time due to the enhanced conduction process by percolating MWNT-AgNP within the nanocomposites. However, the nanocomposites incorporated with very low AgNP content exhibited a longer relaxation time. This is because the nanoparticles at below percolation threshold require high charging energy and inhibits the electrons from transferring through isolated metal islands (Lu et al., 2006).

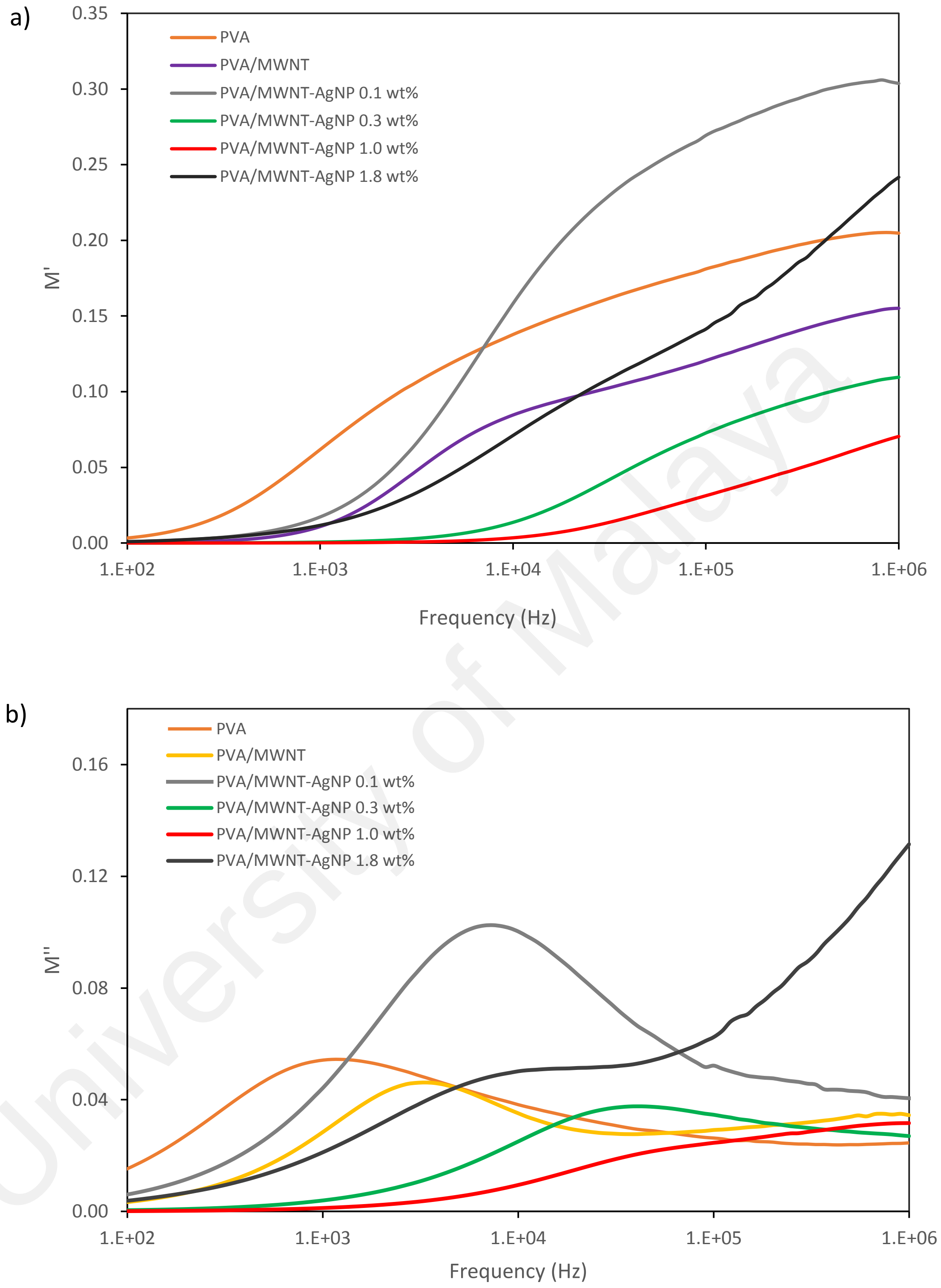

Figure 4.20: The frequency dependence of (a) real dielectric modulus, M′ and (b) imaginary dielectric modulus, M′′, for the PVA/MWNT-AgNP nanocomposites with different AgNP content.

4.2.6 Vector network analysis

4.2.6.1 Complex permittivity and permeability

The complex permittivity ($\varepsilon^* = \varepsilon' - j\varepsilon''$) and complex permeability ($\mu^* = \mu' - i\mu''$) of PVA/MWNT-AgNP nanocomposites are measured at microwave frequency (8-12 GHz). In this part, the composition variation of the nanocomposites was up to 1.0 wt% AgNP, which already shows the optimum permittivity at low frequency range. This is because beyond that composition, the results are no longer consistent with the others and not reliable due to poor structure properties and fillers distribution in the samples.

Figure 4.21 depicts the variation in real part (ε') and imaginary part (ε'') of complex permittivity as a function of frequency and fillers content in the X-band. The trend of ε' curves for all samples in Figure 4.21(a) depicts a good stability against the applied frequency, thus indicating charges displacement or polarizations remain constant within 8-12 GHz. However, the ε' values are varies depending on the amount of fillers content as well. Initially, the ε' value of pure PVA was increased from 4 to 12 with the inclusion of low MWNT content. On the other hand, the incorporation of MWNT-AgNP significantly increased ε' values in the range of 17-25. This result is even higher than that reported for polyurethane composites initiated at high loading of MWNT (30%) (Bhattacharya, Sahoo, & Das, 2012). It implies that the increased of AgNP content induced a larger magnitude of polarization due to the existence of more free mobile electrons coming from the metallic particles and the skeleton of MWNT.

The dielectric behavior is originated from different polarization modes including electronic, atomic and orientation polarization. It occurs as the charges locally bound in atoms, molecules or defect structures rearrange their position in response to the electromagnetic field (Ahmad, 2012). At high frequency, the ε' trend arises mainly from dipolar and interfacial polarization. Herein, the inclusion of electrically conductive MWNT-AgNP induced high interfacial or space charge polarization when the mobile charges are impeded at the interfaces between the conducting regions and the insulating polymers. The orientation (dipolar) polarization occurs due to permanent dipoles moment created by the strong interaction of polar molecules in the matrix. Whereas in Figure 4.21(b) demonstrates the dielectric loss, ε''(energy loss) of the nanocomposites in response to the external electric field is increased with increasing AgNP contents but slowly decreases with an increase in frequency. It denotes that the incorporation of MWNT-AgNP contributed to some energy loss by dissipating EM energy as heat.

.

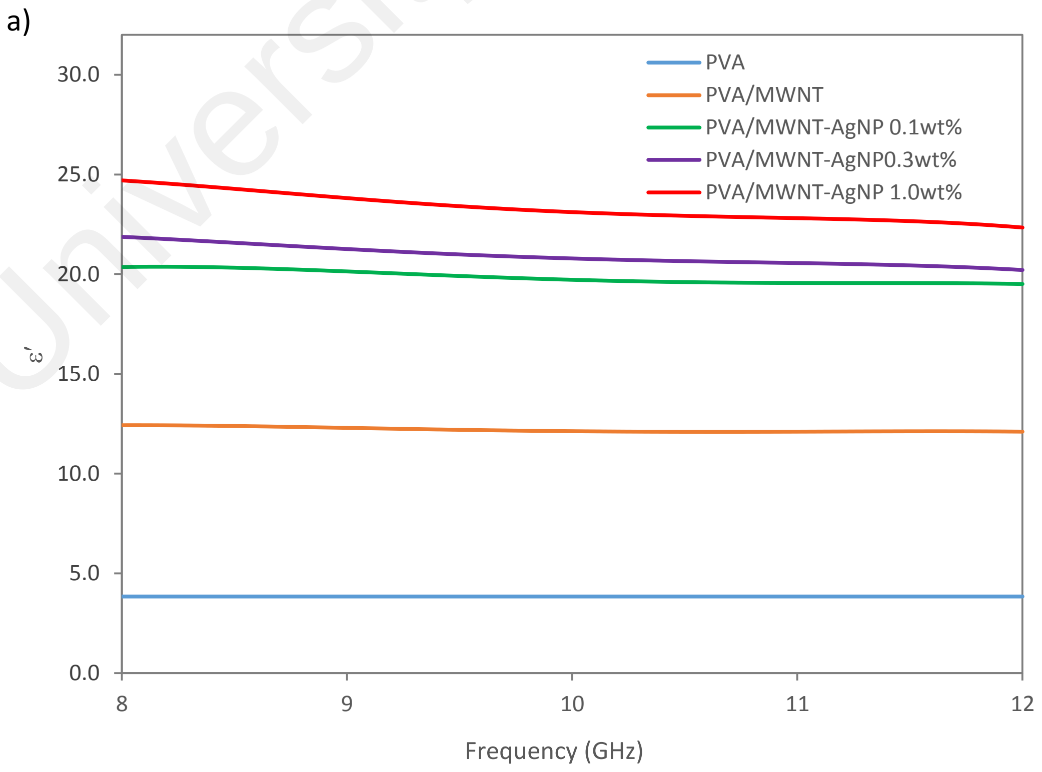

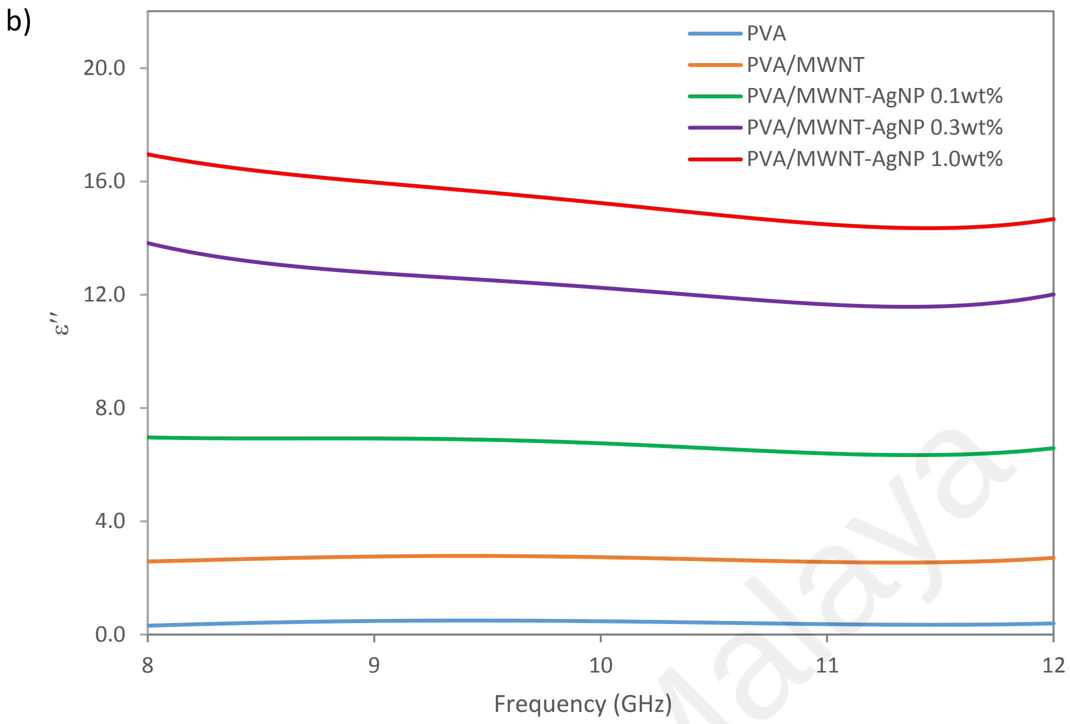

Figure 4.21: The variation in (a) real part, ε' and (b) imaginary part, ε'' of PVA/MWNT-AgNP nanocomposites.

Figure 4.22 depicts the correlation on dielectric permittivity and loss tangent (tan $\delta_\varepsilon = \varepsilon''/\varepsilon''$) or known as dissipation factor, D_f of the nanocomposites. It shows the potential as low loss dielectric materials at high frequency bandwidth. Meanwhile Figure 4.23 shows the ac conductivity for pure PVA and PVA/MWNT are initially independence of frequency. Conversely, upon loading of MWNT-AgNP in the nanocomposites resulted in gradual increment of ac conductivity in the range of 3-10 S/m as the frequency and AgNP content increases. This could be ascribed to the tunneling effect among the adjacent conductive particles when the electrons gain higher energy as the frequency increases (Yuping et al., 2008, Zhao et al., 2014).

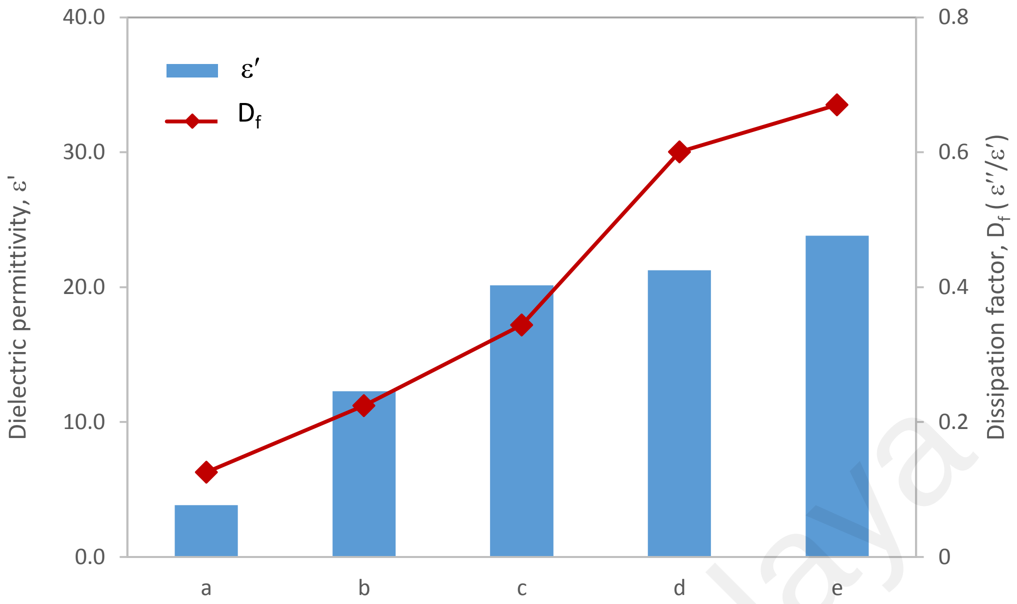

Figure 4.22: The correlation between dielectric permittivity and loss tangent of PVA/MWNT-AgNP nanocomposites at different AgNP contents (a) PVA (b) PVA/MWNT (c) 0.1 wt% (d) 0.3 wt% and (e) 1.0 wt% .

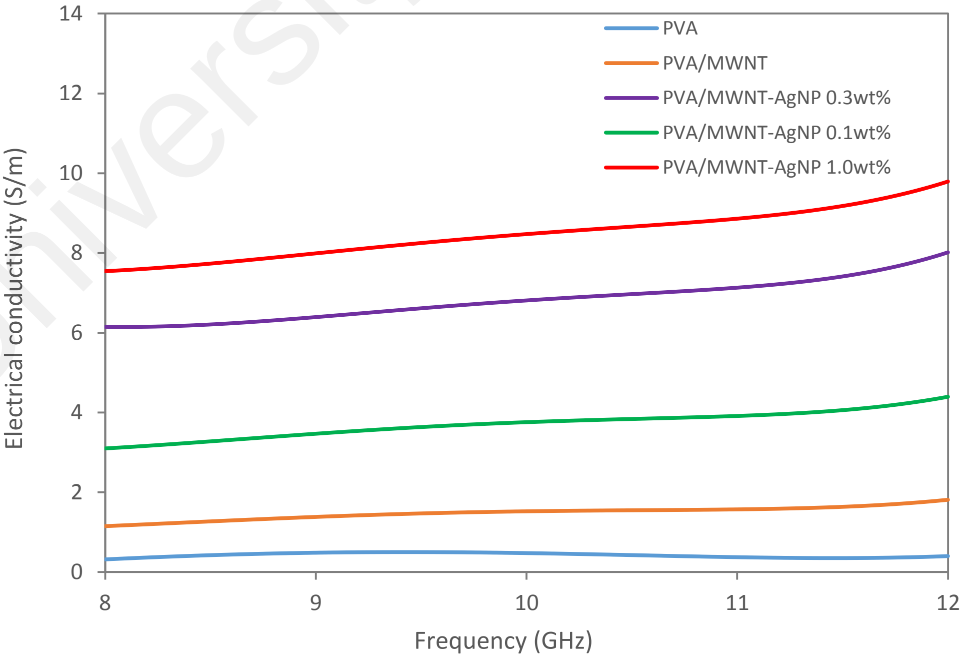

Figure 4.23: The variation of ac-conductivity in X-band frequency.

Figure 4.24 demonstrates the real part (μ') and imaginary part (μ'') of complex permeability for the nanocomposites measured in the X band frequency of 8-12 GHz. The trend of μ' for pure PVA and PVA/MWNT in Figure 4.24(a) are independent of the applied frequency, which lie constant at 0.8 and 0.7, respectively. Conversely, MWNT filled epoxy composites was reported with a greater μ' value of 1.1 (Zhang et al., 2017). Herein, the μ' trend for PVA/MWNT-AgNP nanocomposites with the result of increasing AgNP content up to 1.0 wt% has decreased the value to reach 0.55 and remain unchanged along the X-band frequency. Since the μ'value is much smaller than one, it shows that the nanocomposites exhibited a weak magnetic response to an external magnetic field because of no significant magnetization in the presence of AgNP. It is expected since MWNT and AgNP itself is non-magnetic materials with permeability close to one ($\mu' \approx 1$) (Groenen, 2010). Though, the structure and particle sizes of the fillers could influence permeability of the materials (Zhang et al., 2015). The μ' values of the nanocomposites vary for different AgNP content due to their numerous particle sizes as confirmed in previous microscopic study.

Whereas in Figure 4.24(b) shows the imaginary part, μ'' of permeability representing magnetic loss or energy loss that occur in the samples caused by alternating magnetization. It depicts that the magnetic loss of the nanocomposites increase as the AgNP content is increased and decrease gradually with an increase in frequency. This trend is due to spin rotation of the electrons and domain wall motion in response to the magnetic field (Li et al., 2007). Magnetic losses arise from hysteresis losses and eddy current losses induced in good conductor, which causing repulsive forces with the applied magnetic fields since both fillers and the matrix are inherently diamagnetic (Groenen, 2010). It can be seen for 1.0 wt% of AgNP content, the μ'' trends show rapid drop from 8 GHz to 9 GHz and gradually decrease with increasing frequency. It is caused by magnetic domain wall resonance attributed to the high concentration of AgNP (Ribadeneyra, 2014).

Figure 4.24(c) shows the variation in magnetic dissipation factor as expressed by $\tan \delta_\mu = \varepsilon''/\varepsilon''$, which is gradually decreased as a function of frequency. It seems that $\tan \delta_\mu$ followed the same trend induced by the magnetic loss since the real part, μ' of the nanocomposites did not discern strong magnetization with the external field. The maximum value of $\tan \delta_\mu$ is observed around 8.3 declines to reach 0.5 as the frequency increases from 8 to 12 GHz. Although the nanocomposites have demonstrated both dielectric and magnetic loss, but $\tan \delta_\mu$ is found more variable with frequency than the $\tan \delta_\varepsilon$ in the X-band region. This is because the inclusion of AgNP with MWNT do not provide significant value in magnetic permeability but is capable to enhance the dielectric properties of the nanocomposites.

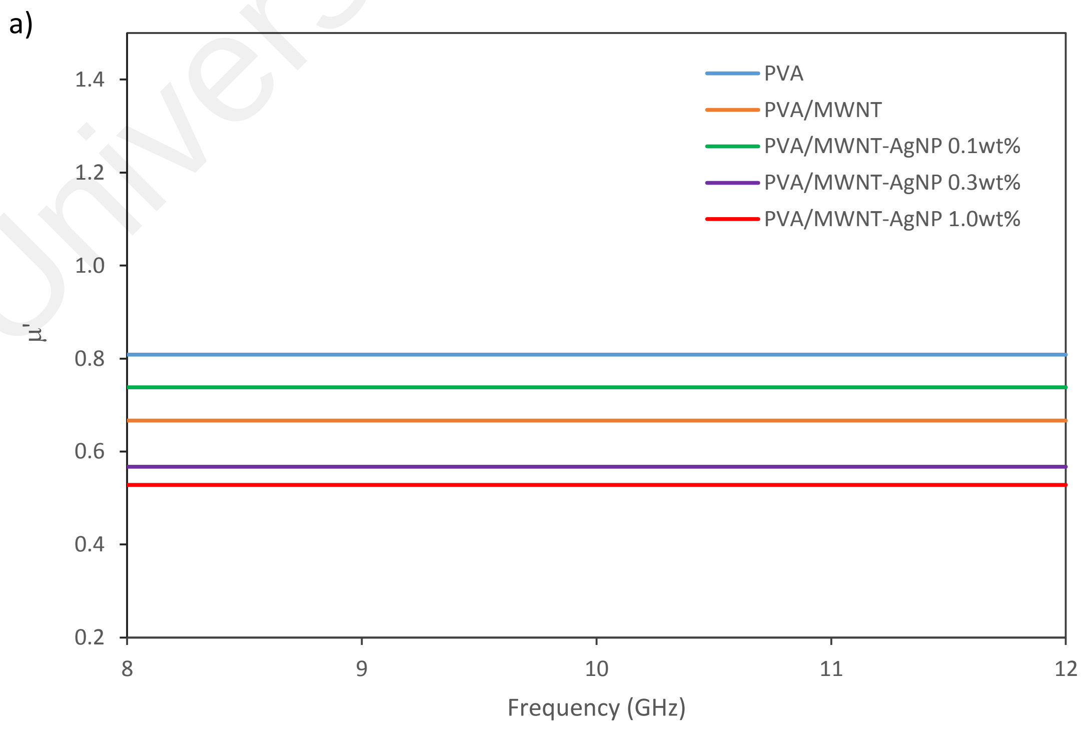

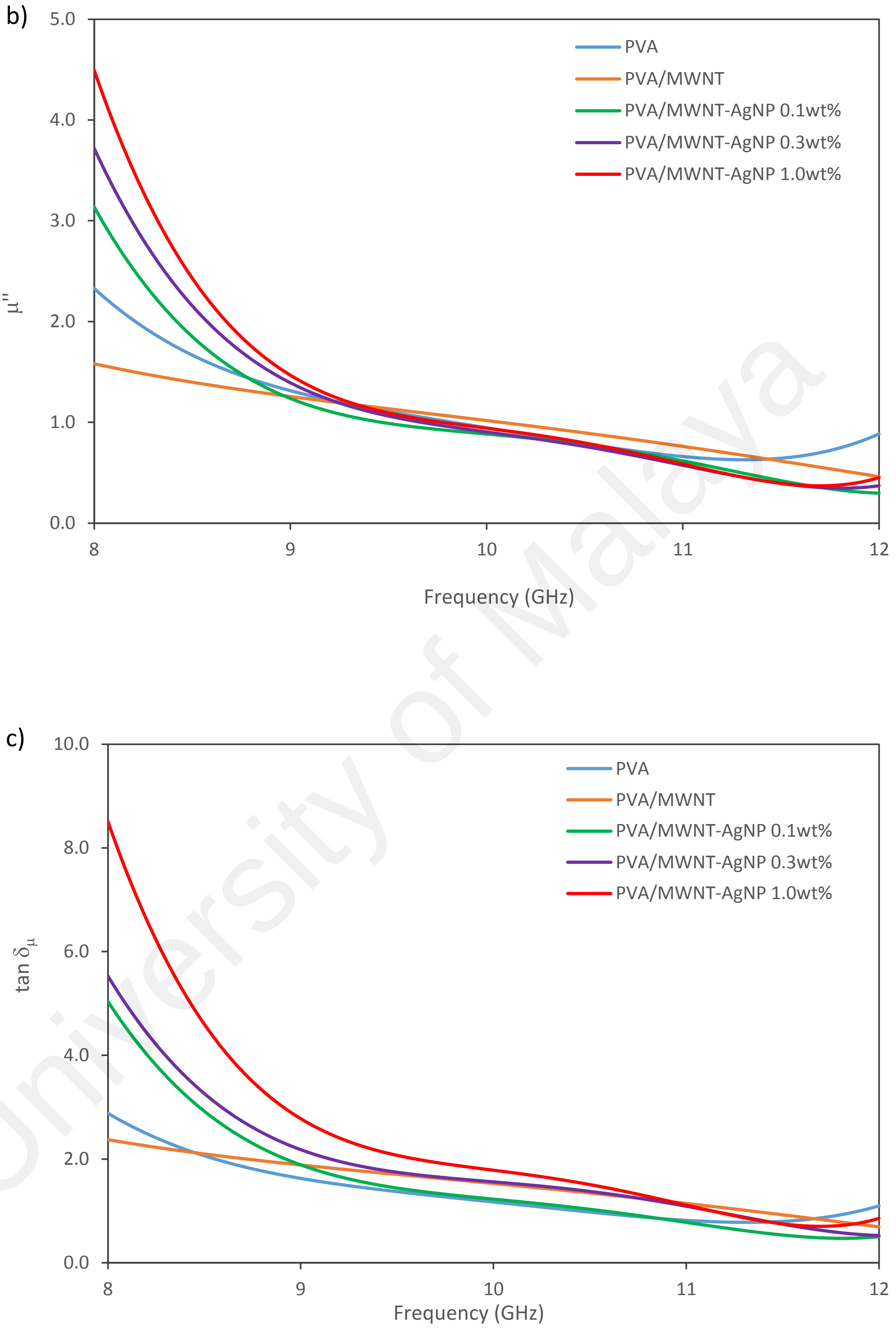

Figure 4.24: Shows (a) real part, μ' (b) imaginary part, μ'' of complex permeability and (c) tan μ for the nanocomposites.

4.2.6.2 Electromagnetic scattering properties

Electromagnetic scattering properties (S-parameters) of PVA/MWNT-AgNP nanocomposites in X-band frequency of 8 to 12 GHz have been analyzed as shown in Figure 4.25. The measured power data shows a tolerance from zero to one that corresponds to the constant value of incident power (P_{in} =1). The measurements for all samples are taken with an average film thickness of about 0.32 mm. As seen in Figure 4.25(a), the magnitude of transmitted power (P_{out}) in PVA/MWNT-AgNP nanocomposites are much lower than pure PVA that lie between 0.15 and 0.30 over the applied frequency. It suggests that the decrease of transmitted power is due to the contribution of reflection and absorption mechanism in the nanocomposite structures. Figure 4.25(b-c) depict the variation of reflected power (P_{ref}) and absorbed power (P_{abs}) as a function of X-band frequency. The absorbed power lies between 0.4 and 0.5, which is more stable over the applied frequency compared to pure PVA and PVA/MWNT. Whereas the magnitude of the reflected power lies between 0.25 and 0.35 over the same frequency. It shows that the amount of power blocked by the absorption is higher than the reflection when the content of AgNP increases in the nanocomposites. It is expected that increasing sample thickness could result in a higher reflection and lower transmission as reported in few studies (Soleimani et al., 2012; Kim et al., 2012).

The absorption mechanism originates from polarization of the materials arise mainly from dangling bonds of MWNT and its defect sites. It endows high electric dipoles steering and interfacial polarization when subjected under an external EM field (Vázquez & Prato, 2009; Zhang et al., 2014; Zhang et al., 2017). The increment of EM absorption was observed with increasing the AgNP contents due to the increased of defects density and charge carriers concentration in the nanocomposites. It proves that the deposition of AgNP induced more defects on the MWNT structures as discussed earlier by the Raman analysis in Section 4.1.3. Another absorption mechanism may be triggered from multiple scattering of internal reflection owing to the defect sites and porous structure of the MWNT-AgNP embedded in the nanocomposites (Zhang et al., 2011; Saini & Choudhary, 2013). The film-like morphologies and porous structure of the nanocomposites as seen in the previous FESEM analysis. Physically, the EM absorption increases as transparency of the materials decreases with increasing fillers content, suggesting the formation of higher crystalline parts than amorphous parts in the polymer matrix (Figure 4.26). Thereby, the multiple internal reflection could take place at the crystalline regions between MWNT-AgNP/dielectric matrix interfaces.

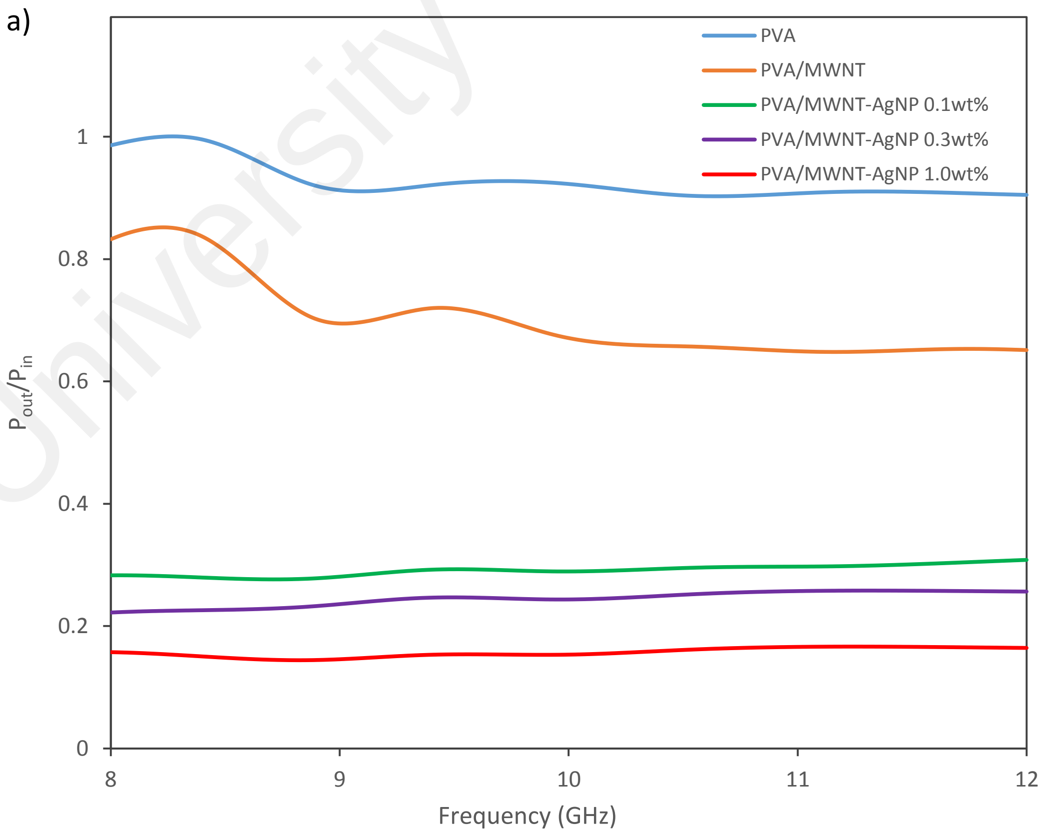

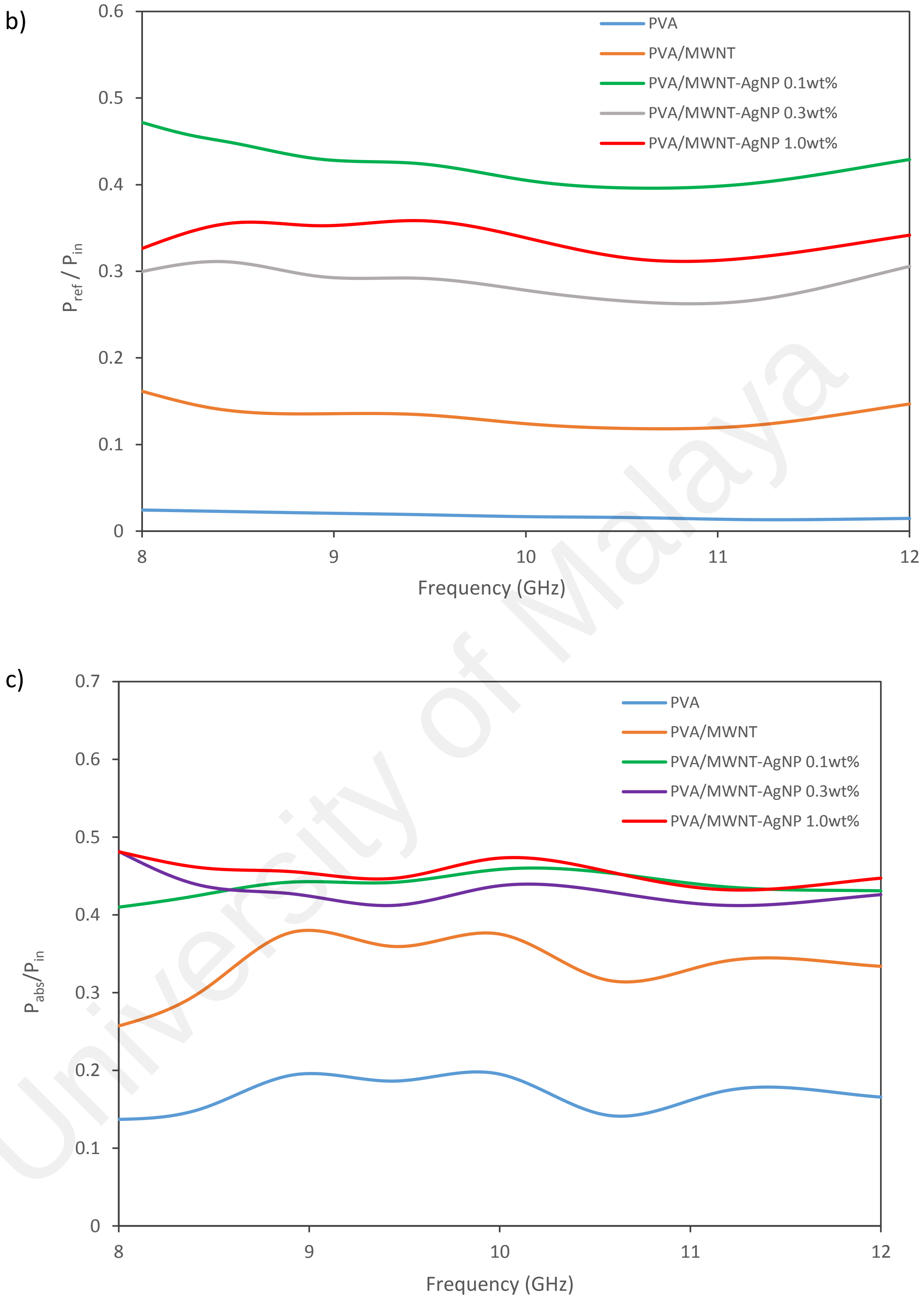

Figure 4.25: The variation in scattering parameters of the (a) transmitted power, (b) reflected power and (c) absorbed power in relation to the incident power source as a function of frequency for PVA/MWNT-AgNP nanocomposites.

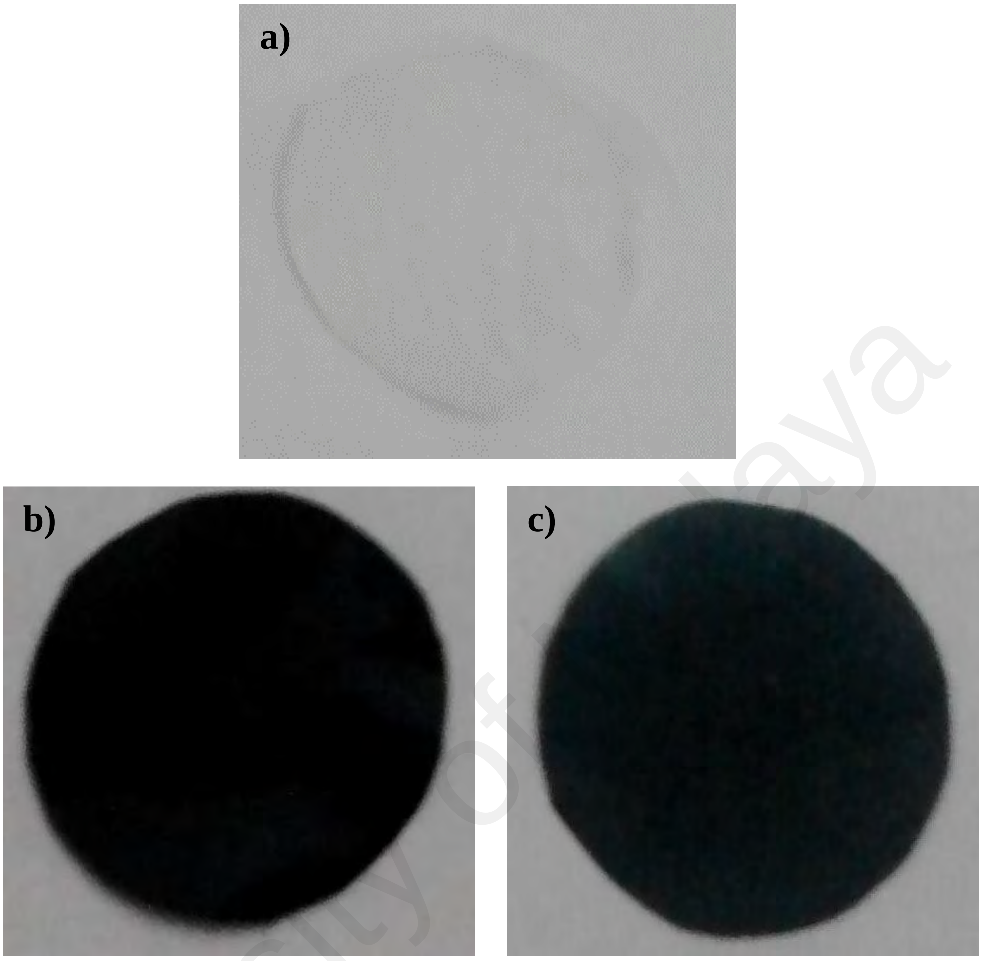

Figure 4.26: Pictures of (a) pure PVA, (b) PVA/MWNT and (c) PVA/MWNT-AgNP nanocomposites.

Figure 4.27 depicts the effect of different AgNP content on the scattered power data for PVA/MWNT-AgNP nanocomposites measured at 9 GHz. It is clearly seen that PVA shows almost 90% transmission of the incident power. Meanwhile, PVA/MWNT reduces the amount of transmitted power by 20% due to dominant contribution of absorption mechanism from the MWNT. However, the reflection is not much improved indicating low conductivity of the nanocomposites at low MWNT loading. In contrast, the inclusion of MWNT-AgNP significantly reduced EM wave from the incident power since the addition of AgNP increases the absorption capability of MWNT and reflection on the material surfaces. Initially at 0.1wt% of AgNP, the nanocomposite exhibit almost same magnitude between the reflected power and the absorbed power. This is ascribed to high surface reactivity of very fine Ag particles that contributed in much reflection.

However, it seems that increasing the AgNP contents in the nanocomposites up to 1.0 wt% significantly reduced the transmission of EM wave as compared to the PVA and MWNT. The reflection decreases as the absorption increases at a higher loading of AgNP due to the variation in their particles sizes. The optimum performance was obtained at 1.0 wt% of AgNP having the particles size of about 40 nm, which shows the highest absorption (47%) with the lowest reflection (30%). In comparison, the highest EM absorption of iron particle nanocomposites were reported up to 20% with the best size of 50 nm (Jalali, Dauterstedt, Michaud, & Wuthrich, 2011). The dominant amount of absorbed power in this work truly corresponds to their high permittivity values ($\varepsilon' \approx 25$). It implies capability of the materials to attenuate power or energy and dissipate as heat (dielectric loss). Even though the nanocomposites exhibit moderate conductivity ($\sigma \approx 8.0$ S/m) as compared to metallic materials, they still can be promising as thin and lightweight absorbing materials for high frequency applications.

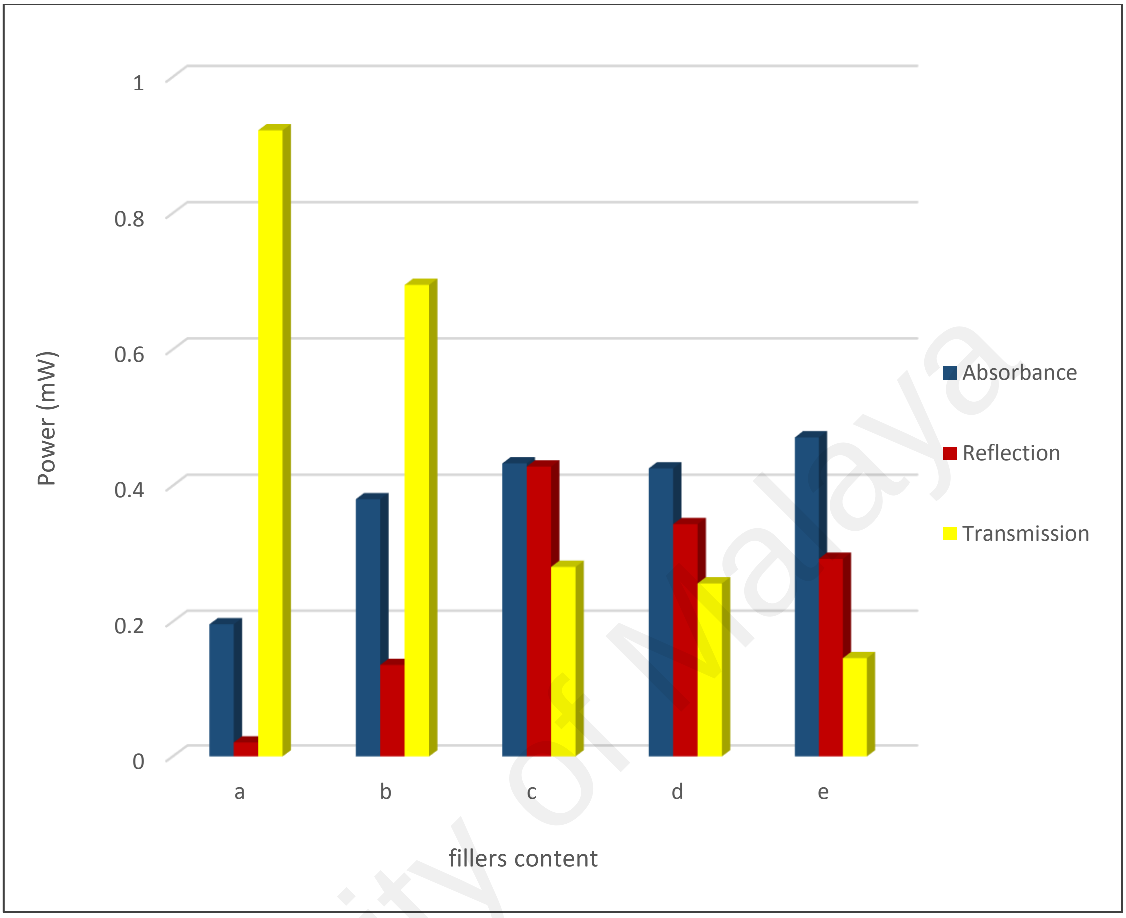

Figure 4.27: The power data versus fillers content in the X-band frequency for different samples: (a) PVA, (b) PVA/MWNT, (c) PVA/MWNT-AgNP 0.1wt%, (d) PVA/MWNT-AgNP 0.3wt% and (e) PVA/MWNT-AgNP 1.0wt%.

CHAPTER 5 : CONCLUSIONS

5.1 Conclusion

In conclusion, this work has covered extensively the synthesis and characterization of MWNT-AgNP filled PVA nanocomposites. MWNT-AgNP was primarily synthesized by reducing different volume of silver salt ($AgNO_3$) in the presence of functionalized MWNT, assisted with SDS as the surfactant agent. Sequentially, PVA/MWNT-AgNP nanocomposites were fabricated by solution mixing and casting method. This study emphasized the properties of MWNT-AgNP obtained with different AgNP contents and its distinctive effect as conductive fillers to attain high dielectric permittivity PVA nanocomposites.

The analysis of MWNT-AgNP have shown the morphology and structural properties of the hybrid filler as compared to the pristine MWNT. TEM images reveals that MWNT are much bent with increasing AgNP assembled onto the nanotube surface due to the presence of a defect in the graphitic network. FTIR spectra prove the presence of some oxygenated groups introduced to the nanotube walls, which served as nucleation sites for the reduction of Ag ions (Ag^+). The transmittance intensity of the MWNT-AgNP decreases upon increasing AgNP contents. Raman spectra indicate that deposition of AgNP results in linear dependence of I_D/I_G on $I_{D'}/I_G$ ratio with increasing AgNP due to the charge-transfer between AgNP and MWNT.

Meanwhile, the study of PVA/MWNT-AgNP discussed on the morphology, structural and electrical properties of the nanocomposites with an emphasis on the dielectric measurements. Morphological study shows the percolation of MWNT-AgNP at different AgNP loading resulted in particles size varies from 17nm to 55nm. UV-vis profile correlates the redshift of MWNT absorption peak at 262nm was due to the occurrence of charge transfer process and the increase in particle size of AgNP embedded together in the nanocomposites. The structural features were supported by FTIR and X-ray diffraction (XRD) patterns, which verified the intermolecular interactions between hydroxyl content in PVA and the filler that favours polymer crystallization. Thermal stability of the nanocomposites was found increased by 40°C as compared to pure PVA. Impedance Spectroscopy (IS) analysis revealed the high frequency dependence of electrical and dielectric properties of the nanocomposites at low frequency range (50Hz-1MHz). The nanocomposite has achieved the ultimate real permittivity of 600 at low frequency of 100 Hz, which decreases with increasing frequency. Remarkably, the permittivity value remains steady near 25 and shows weak frequency dependence in the X-band range from 8 GHz to 12 GHz. The nanocomposites are preference as metal behavior at high frequency where the value remains constant near 0.7. It implies a low interaction of the nanocomposites with a magnetic field in the presence of AgNP.

Overall, these findings established that the inclusion of MWNT-AgNP 1.0wt% filled PVA nanocomposites have attained the optimum dielectric permittivity, corresponding to their well structure properties, morphology, thermal and electrical properties. Interestingly, electromagnetic (EM) properties of the nanocomposites have shown the highest absorption (47%) and the lowest reflection (30%) were obtained at 1.0 wt% of AgNP having the particles size of about 40 nm. It implies the capability of PVA/MWNT-AgNP nanocomposites to attenuate EM wave and dissipate as heat (high dielectric loss). Thus, they could offer thin and flexible dielectric-absorbing materials for high frequency electronic devices.

5.2 Recommendations for future works

This study has established the high permittivity of MWNT-AgNP reinforced PVA nanocomposites. The results were achieved due to significant polarization induced by the interaction between both nanosize fillers and the polymer matrix. In this regards, still many aspects to be addressed for future prospects of this study.

Based on the state of this work, the difference in the Ag content can result in the difference in the size of AgNPs. It is worth to prepare the nanocomposites with diffferent Ag content but the same size of AgNP, and compare the performance of the PVA/MWNT-AgNP nanocomposites. This preparation may be performed by other method presented here. The structure properties of MWNT-AgNP hybrid can be carried out by other deposition technique that can control the assembly of AgNP on nanotube surfaces. This can be consider as one of the future research target.

Further investigation should elucidate the effect of varying the amount of surfactant, SDS used during the synthesis of MWNT-AgNP via chemical reduction method. Therefore, the physical mixture of MWNTs with SDS and free AgNPs prepared separately could provide the MWNT-AgNP hybrids with different Ag content and the same size of AgNP as well. The size, shape and concentration of MWNT-AgNP may have important effect on the electrical and dielectric properties of the polymer nanocomposites. The future works can analyze the performance of these nanocomposites at different temperature.

Meanwhile, it can be interesting to analyze the electromagnetic properties towards Terahertz frequency, in order to impart the synergetic effect of integrating high permittivity of PVA/MWNT-AgNP nanocomposites as the dielectric-absorbing materials. However, this study was limited due to very thin film thickness. Further research can consider a greater sample thickness to measure shielding effectiveness of the materials as one of the potential electronic devices for high frequency applications. Nowadays, the advanced materials and nanotechnology has been recognized as one of the new growth engines for the New Economic Model (NEM) in Malaysia especially for Electronic and Electrical (E & E) sector.

REFERENCES

Abdul kareem, T., & Anu kaliani, A. (2011). Synthesis and thermal study of octahedral silver nano-plates in polyvinyl alcohol (PVA). *Arabian Journal of Chemistry*, *4*(3), 325–331.

Ahmad, Z. (2012). Polymeric Dielectric Materials. *Dielectric Material*, 3–26.

Ahmadpoor, F., Zebarjad, S. M., & Janghorban, K. (2013). Decoration of multi-walled carbon nanotubes with silver nanoparticles and investigation on its colloid stability. *Materials Chemistry and Physics*, *139*(1), 113–117.

Ahmed, D. S., Haider, A. J., & Mohammad, M. R. (2013). Comparesion of Functionalization of multi Ğ walled carbon nanotubes treated by oil olive and nitric acid and their characterization. *Energy Procedia*, *36*, 1111–1118.

Alghunaim, N. S. (2016). Optimization and spectroscopic studies on carbon nanotubes/PVA nanocomposites. *Results in Physics*, *6*, 456–460.

Alimohammadi, F., Parvinzadeh, M., & Shamei, A. (2012). Superlattices and Microstructures Deposition of silver nanoparticles on carbon nanotube by chemical reduction method : Evaluation of surface , thermal and optical properties. *Superlattices And Microstructures*, *52*(1), 50–62.

Amrin, S., & Deshpande, V. D. (2016). Dielectric relaxation and ac conductivity behavior of carboxyl functionalized multiwalled carbon nanotubes / poly (vinyl alcohol) composites. *Physica E: Low-Dimensional Systems and Nanostructures*, *87*, 317–326.

Avile, F, Cauich-Rodrı´guez, J.V., Moo-Tah, L., May-Pat, A., Vargas-Coronado, R. (2009). Evaluation of mild acid oxidation treatments for MWCNT functionalization. *Carbon*, *47*, 2970–2975.

Bandaru, P. R. (2007). Electrical Properties and Applications of Carbon Nanotube Structures. *Journal of Nanoscience and Nanotechnology*, *7*(4), 1239–1267.

Bartholome, C., Miaudet, P., Derré, A., Maugey, M., Roubeau, O., Zakri, C. & Paulin, P. (2008). Influence of surface functionalization on the thermal and electrical properties of nanotube-PVA composites. *Composites Science and Technology*, *68*, 2568–2573.

Basiuk, E. V., Anis, A., Bandyopadhyay, S., Alvarez-Zauco, E., Chan, S. L. I., & Basiuk, V. A. (2009). Poly(vinyl alcohol)/CNT composites: An effect of cross-linking with glutaraldehyde. *Superlattices and Microstructures*, *46*(1–2), 379–383.

Bhajantri, R. F., Ravindrachary, V., Harisha, A., Ranganathaiah, C., & Kumaraswamy, G. N. (2007). Effect of barium chloride doping on PVA microstructure: Positron annihilation study. *Applied Physics A: Materials Science and Processing*, *87*(4), 797–805.

Bhattacharya, P., Sahoo, S., & Das, C. K. (2012). Microwave absorption behaviour of MWCNT based nanocomposites in X-band region. *Express Polymer Letters*, *7*(3), 212–223.

Bhui, D. K., Bar, H., Sarkar, P., Sahoo, G. P., De, S. P., & Misra, A. (2009). Synthesis and UV-vis spectroscopic study of silver nanoparticles in aqueous SDS solution. *Journal of Molecular Liquids*, *145*(1), 33–37.

Bittencourt, C., Felten, A., Ghijsen, J., Pireaux, J. J., Drube, W., Erni, R., & Van Tendeloo, G. (2007). Decorating carbon nanotubes with nickel nanoparticles. *Chemical Physics Letters*, *436*(4–6), 368–372.

Bushroa, A. R., Rahbari, R. G., Masjuki, H. H., & Muhamad, M. R. (2012). Approximation of crystallite size and microstrain via XRD line broadening analysis in TiSiN thin films. *Vacuum*, *86*, 1107–1112.

Chahal, R. P., Mahendia, S., Tomar, A. K., & Kumar, S. (2015). UV irradiated PVA-Ag nanocomposites for optical applications. *Applied Surface Science*, *343*, 160–165.

Chen, C., Kine, A., Nelson, R. D., & LaRue, J. C. (2015). Impedance spectroscopy study of conducting polymer blends of PEDOT:PSS and PVA. *Synthetic Metals*, *206*, 106–114.

Chiellini, E., Corti, A., Antone, S. D., & Solaro, R. (2003). *Biodegradation of poly (vinyl alcohol) based materials* (Vol. 28).

Cullity, B. D., & Stock, S. R. (2001). *Elements of X-ray Diffraction* (Vol. 3, p. 15). New Jersey: Prentice hall.

Daenen, M., De Fouw, R. D., Hamers, B., Janssen, P. G. A., Schouteden, K., & Veld, M. A. J. (2003). The wondrous world of carbon nanotubes. *Eindhoven University of Technology*, *27*.

Dang, Z. M., Wang, L., Yin, Y., Zhang, Q., & Lei, Q. Q. (2007). Giant dielectric permittivities in functionalized carbon-nanotube/electroactive-polymer nanocomposites. *Advanced Materials*, *19*(6), 852–857.

Dang, Z. M., Yuan, J. K., Zha, J. W., Zhou, T., Li, S. T., & Hu, G. H. (2012). Fundamentals, processes and applications of high-permittivity polymer-matrix composites. *Progress in Materials Science*, *57*(4), 660–723.

Du, J., Bai, J., & Cheng, H. (2007). The present status and key problems of carbon nanotube. *Express Polymer Letters*, *1*(5), 253–273.

Dutta, P., Biswas, S., & De Kumar, S. (2002). Dielectric relaxation in polyaniline-polyvinyl alcohol composites. *Materials Research Bulletin*, *37*(1), 193–200.

Eckmann, A., Felten, A., Mishchenko, A., Britnell, L., Krupke, R., Novoselov, K. S., & Casiraghi, C. (2012). Probing the Nature of Defects in Graphene by Raman Spectroscopy. *Nano Letters*, *12*, 3925–3939.

Elimat, Z., Al-Hussami, S. A., & Zihlif, A. M. (2012). Effect of carbon black on the thermoelectrical properties of poly(ethylene-oxide) composites. *Journal of Composite Materials*, *47*(28), 3525–3534.

Ellis, A.V., Vijayamohanan, K., Goswami, R., Chakrapani, N., Ramanathan, L.S., Ajayan, P.M. & Ramanath, G. (2003) Hydrophobic anchoring of monolayer-protected gold nanoclusters to carbon nanotubes, *Nano Letters.* 3, 279–282.

Feng, M., Sun, R., Zhan, H., & Chen, Y. (2010). Decoration of carbon nanotubes with CdS nanoparticles by polythiophene interlinking for optical limiting enhancement.

Carbon, *48*, 1177–1185.

Forro, L., & Schoenenberger, C. (2001). Physical properties of multi-wall nanotubes. In *Carbon Nanotubes* (pp. 329-391). Springer, Berlin, Heidelberg.

Fortunati, E., Angelo, F. D., Martino, S., Orlacchio, A., Kenny, J. M., & Armentano, I. (2011). Carbon nanotubes and silver nanoparticles for multifunctional conductive biopolymer composites. *Carbon*, *49*, 2370–2379.

Georgakilas, V., Gournis, D., Tzitzios, V., Pasquato, L., Guldi, D. M., & Prato, M. (2007). Decorating carbon nanotubes with metal or semiconductor nanoparticles. *Journal of Materials Chemistry*, *17*, 2679–2694.

Groenen, R. (2010). Electrical and Microwave Characteristics of Silver Nanoparticle Composites. *University of Twente Enschede*, (May). Retrieved from http://www.utwente.nl/tnw/ims/people/formerMSc/Rik Groenen.pdf.

Grossiord, N., Kivit, P. J. J., Loos, J., Meuldijk, J., Kyrylyuk, A. V, Schoot, P. Van Der, & Koning, C. E. (2008). On the influence of the processing conditions on the performance of electrically conductive carbon nanotube / polymer nanocomposites. *Polymer*, *49*, 2866–2872.

Hallensleben, M. L., Fuss, R., & Mummy, F. (2000). Polyvinyl compounds, others. *Ullmann's Encyclopedia of Industrial Chemistry*, 1-23.

He, F., Lau, S., Chan, H. L., & Fan, J. (2009). High dielectric permittivity and low percolation threshold in nanocomposites based on poly(vinylidene fluoride) and exfoliated graphite nanoplates. *Advanced Materials*, *21*(6), 710–715.

Henglein, A. (2001). Reduction of Ag(CN)2- on silver and platinum colloidal nanoparticles. *Langmuir*, *17*(8), 2329–2333.

Herley, P. J., & Prout, E. G. (1960). The Thermal Decomposition of Silver Oxide. *Journal of the American Chemical Society*, *82*(7), 1540–1543.

Iijima, S. (1991). Helical Microtubules of Graphitic Carbon. *Nature,* 354, 56-58.

Inverter Technology, Trends and Market Expectations report. (2016). *Yole*

Development.

Ioannou, G., Patsidis, a., & Psarras, G. C. (2011). Dielectric and functional properties of polymer matrix/ZnO/BaTiO3 hybrid composites. *Composites Part A: Applied Science and Manufacturing*, *42*(1), 104–110.

Jalali, M., Dauterstedt, S., Michaud, A., & Wuthrich, R. (2011). Composites : Part B Electromagnetic shielding of polymer – matrix composites with metallic nanoparticles. *Composites Part B*, *42*, 1420–1426.

Kelly, K. L., Coronado, E., Zhao, L. L., & Schatz, G. C. (2003). The Optical Properties of Metal Nanoparticles: The Influence of Size, Shape, and Dielectric Environment. *J. Phys. Chem. B*, *107*, 668–677.

Khanna, P. K., Singh, N., Charan, S., Subbarao, V. V. V. S., Gokhale, R., & Mulik, U. P. (2005). Synthesis and characterization of Ag/PVA nanocomposite by chemical reduction method. *Materials Chemistry and Physics*, *93*(1), 117–121.

Kim, H. R., Kim, B. S., & Kim, I. S. (2012). Fabrication and EMI shielding effectiveness of Ag-decorated highly porous poly(vinyl alcohol)/Fe 2O 3 nanofibrous composites. *Materials Chemistry and Physics*, *135*(2–3), 1024–1029.

Kim, K. K., Park, J. S., Kim, S. J., Geng, H. Z., An, K. H., Yang, C. M., Sato, K., Saito, R. & Lee, Y. H. (2007). Dependence of Raman spectra G′ band intensity on metallicity of single-wall carbon nanotubes. *Physical Review B - Condensed Matter and Materials Physics*, *76*(20), 205426-1-8

Kulshrestha, N., Chatterjee, B., & Gupta, P. N. (2014). Characterization and electrical properties of polyvinyl alcohol based polymer electrolyte films doped with ammonium thiocyanate. *Materials Science and Engineering: B*, *184*, 49–57.

Larrude, D. G., Maia, M. E. H., & Jr, F. L. F. (2014). Synthesis and Characterization of Silver Nanoparticle-Multiwalled Carbon Nanotube Composites, *Journal of Nanomaterials*, *654068*, 1–7.

Lehman, J. H., Terrones, M., Meunier, V., Mansfield, E., & Hurst, K. E. (2011). Evaluating the characteristics of multiwall carbon. *Carbon*, *49*(8), 2581–2602.

Li, B. W., Shen, Y., Yue, Z. X., & Nan, C. W. (2007). Influence of particle size on electromagnetic behavior and microwave absorption properties of Z-type Ba-ferrite/polymer composites. *Journal of Magnetism and Magnetic Materials*, *313*(2), 322–328.

Li, J., & Liu, C. (2010). Ag/Graphene Heterostructures: Synthesis, Characterization and Optical Properties. *European Journal of Inorganic Chemistry*, *2010*(8), 1244–1248.

Liang, G. D., Bao, S. P., & Tjong, S. C. (2007). Microstructure and properties of polypropylene composites filled with silver and carbon nanotube nanoparticles prepared by melt-compounding. *Materials Science and Engineering B*, *142*, 55–61.

Liu, Y., Tang, J., Chen, X., Chen, W., Pang, G. K. H., & Xin, J. H. (2006). A wet-chemical route for the decoration of CNTs with silver nanoparticles. *Carbon*, *44*(2), 381–383.

Lu, G., Zhu, L., Wang, P., Chen, J., Dikin, D. A., Ruoff, R..S & Ren, Z. F. (2007). Electrostatic-force-directed assembly of Ag nanocrystals onto vertically aligned carbon nanotubes. *Journal of Physical Chemistry C*, *111*(48), 17919–17922.

Lu, J., Moon, K.-S., Xu, J., & Wong, C. P. (2006). Synthesis and dielectric properties of novel high-K polymer composites containing in-situ formed silver nanoparticles for embedded capacitor applications. *Journal of Materials Chemistry*, *16*(16), 1543–1548.

Lu, J., Moon, K. S., Xu, J., & Wong, C. P. (2005). Dielectric loss control of high-K polymer composites by coulomb blockade effects of metal nanoparticles for embedded capacitor applications. *Proceedings of the International Symposium and Exhibition on Advanced Packaging Materials Processes, Properties and Interfaces*, 237–242.

Lu, X., Zhang, W., Wang, C., Wen, T., & Wei, Y. (2011). Progress in Polymer Science One-dimensional conducting polymer nanocomposites : Synthesis , properties and applications. *Progress in Polymer Science*, *36*(5), 671–712.

Ma, P. C., Tang, B. Z., & Kim, J. K. (2008). Effect of CNT decoration with silver nanoparticles on electrical conductivity of CNT-polymer composites. *Carbon*, *46*, 1497–1505.

Ma, P.C., Siddiqui, N. A., Marom, G., & Kim, J. (2010). Composites : Part A Dispersion and functionalization of carbon nanotubes for polymer-based nanocomposites : A review. *Composites Part A*, *41*(10), 1345–1367.

Mahendia, S., Tomar, a. K., & Kumar, S. (2010). Electrical conductivity and dielectric spectroscopic studies of PVA–Ag nanocomposite films. *Journal of Alloys and Compounds*, *508*(2), 406–411.

Mahendia, S., Tomar, A. K., Chahal, R. P., & Kumar, S. (2011). Synthesis and characterization of silver-poly(vinyl alcohol) nanocomposites. *AIP Conference Proceedings*, *1349*(PART A), 339–340.

Majeed Khan, M., Kumar, S., Ahamed, M., Alrokayan, S., & AlSalhi, M. (2011). Structural and thermal studies of silver nanoparticles and electrical transport study of their thin films. *Nanoscale Research Letters*, *6*(434), 1–8.

Malikov, E. Y., Muradov, M. B., Akperov, O. H., Eyvazova, G. M., Puskás, R., Madarász, D. & Kónya, Z. (2014). Synthesis and characterization of polyvinyl alcohol based multiwalled carbon nanotu be nanocomposites. *Physica E: Low-Dimensional Systems and Nanostructures*, *61*, 129–134.

Matsubara, E. Y., Takahashi, G. H., Macedo, N. G., Gunnella, R., & Rosolen, J. M. (2016). Electronic enhancement of hybrid specific capacity of carbon nanotube/bone charcoal composite with Ag nanoparticle decoration. *Journal of Electroanalytical Chemistry*, *765*, 58–64.

Mbhele, Z. H., Salemane, M. G., Van Sittert, C. G. C. E., Nedeljković, J. M., Djoković, V., & Luyt, A. S. (2003). Fabrication and Characterization of Silver-Polyvinyl Alcohol Nanocomposites. *Chemistry of Materials*, *15*(26), 5019–5024.

Melvin, G. J. H., Ni, Q. Q., Suzuki, Y., & Natsuki, T. (2014). Microwave-absorbing properties of silver nanoparticle/carbon nanotube hybrid nanocomposites. *Journal of Materials Science*, *49*(14), 5199–5207.

Melvin, G. J. H., Ni, Q. Q., Natsuki, T., Wang, Z., Morimoto, S., Fujishige, M., … Endo, M. (2015). Ag/CNT nanocomposites and their single- and double-layer electromagnetic wave absorption properties. *Synthetic Metals*, *209*, 383–388.

Mercader, C., Poulin, P., & Zakri, C. (2010). Synthesis and Properties of PVA / Carbon Nanotube Nanocomposites. *Polymer Nanotube Nanocomposites: Synthesis, Properties, and Applications.* Mittal,V. (Eds):Wiley, 315-343.

Migahed, M. D., Ishra, M., Fahmy, T., & Barakat, A. (2004). Electric modulus and AC conductivity studies in conducting PPy composite films at low temperature. *Journal of Physics and Chemistry of Solids*, *65*(6), 1121–1125.

Mulvaney, P. (1996). Surface Plasmon Spectroscopy of Nanosized Metal Particles. *Langmuir*, *12*(3), 788–800.

Paredes, J. I., Villar-Rodil, S., Ma z-Alonso, A., & Tascon, J. M. D. (2008). Graphene oxide dispersions in organic solvents. *Langmuir*, *24*(19), 10560-10564.

Pastoriza-Santos, I., & Liz-Marzán, L. M. (1999). Formation and stabilization of silver nanoparticles through reduction by N, N-dimethylformamide. *Langmuir*, *15*(4), 948-951.

Peng, Y., & Chen, Q. (2012). Fabrication of one-dimensional Ag/multiwalled carbon nanotube nano-composite. *Nanoscale Research Letters*, *7*(1), 195.

Planeix, J.M., Coustel, N., Coq, B., Brotons, V.,. Kumbhar, P. S, Dutartre, R., Geneste, P., Bernier, P. & Ajayan, P.M. (1994). Application of carbon nanotubes as supports in heterogeneous catalysis, *J. Am. Chem. Soc*. 116, 7935–7936.

Qi, L., Lee, B. I., Chen, S., Samuels, W. D., & Exarhos, G. J. (2005). High-dielectric-constant silver-epoxy composites as embedded dielectrics. *Advanced Materials*, *17*(14), 1777–1781.

Qu, L., & Dai, L. (2005). Substrate-enhanced electroless deposition of metal nanoparticles on carbon nanotubes. *Journal of the American Chemical Society*, *127*(31), 10806-10807.

Quinn, B. M., Dekker, C., & Lemay, S. G. (2005). Electrodeposition of noble metal nanoparticles on carbon nanotubes. *Journal of the American Chemical Society*, *127*(17), 6146-6147.

Ramin, M., & Taleshi, F. (2013). The effect of carbon nanotubes as a support on morphology and size of silver nanoparticles. *International Nano Letters*, *3*(32), 1-6.

Ray, D. K., Himanshu, A. K., & Sinha, T. P. (2005). Study of impedance spectroscopy conducting polymer prepared with the use of water soluble support polymer. *Indian Journal of Pure and Applied Physics*, *43*(10), 787–793.

Reilly, R. M. (2007). Carbon Nanotubes: Potential Benefits and Risks of Nanotechnology in Nuclear Medicine. *Journal of Nuclear Medicine*, *48*(7), 1039–1042. http://doi.org/10.2967/jnumed.107.041723

Ribadeneyra, M.C. (2014). EMI shielding composites based on magnetic nanoparticles and nanocarbons. Unpublished Doctoral thesis, Universidad Carlos III de Madrid.

Saat, A. M., & Johan, M. R. (2014). The Surface Structure and Thermal Properties of Novel Polymer Composite Films Based on Partially Phosphorylated Poly (vinyl alcohol) with Aluminum Phosphate. *The Scientific World Journal*, *2014*, 7.

Sahoo, N. G., Rana, S., Cho, J. W., Li, L., & Chan, S. H. (2010). Progress in Polymer Science Polymer nanocomposites based on functionalized carbon nanotubes. *Progress in Polymer Science*, *35*, 837–867.

Sahoo, S., Husale, S., Karna, S., Nayak, S. K., & Ajayan, P. M. (2011). Controlled assembly of Ag nanoparticles and carbon nanotube hybrid structures for biosensing. *Journal of the American Chemical Society*, *133*(11), 4005-4009.

Saini, I., Rozra, J., Chandak, N., Aggarwal, S., Sharma, P. K., & Sharma, A. (2013). Tailoring of electrical, optical and structural properties of PVA by addition of Ag nanoparticles. *Materials Chemistry and Physics*, *139*(2–3), 802–810.

Saini, P., & Choudhary, V. (2013). Enhanced electromagnetic interference shielding effectiveness of polyaniline functionalized carbon nanotubes filled polystyrene composites. *Journal of Nanoparticle Research*, *15*(1415), 1–7.

Sengwa, R. J., Choudhary, S., & Sankhla, S. (2008). Low frequency dielectric relaxation processes and ionic conductivity of montmorillonite clay nanoparticles colloidal suspension in poly(vinyl pyrrolidone)-ethylene glycol blends. *Express Polymer Letters*, *2*(11), 800–809.

Senthil, V., Badapanda, T., Kumar, S. N., Kumar, P., & Panigrahi, S. (2012). Relaxation and conduction mechanism of PVA: BYZT polymer composites by impedance spectroscopy. *Journal of Polymer Research*, *19*(9838).

Singh, R. & Ulrich, R.K. (1999). High and low dielectric constant materials. *The Electrochemical Society Interface*, *8*, 26.

Smalley, R. E. (2003). *Carbon nanotubes: synthesis, structure, properties, and applications* (Vol. 80). Springer Science & Business Media.

Soleimani, H., Abbas, Z., Yahya, N., Soleimani, H., & Ghotbi, M. Y. (2012a). Determination of complex permittivity and permeability of lanthanum iron garnet filled PVDF-polymer composite using rectangular waveguide and Nicholson-Ross-Weir (NRW) method at X-band frequencies. *Measurement: Journal of the International Measurement Confederation*, *45*(6), 1621–1625.

Soleimani, H., Abbas, Z., Yahya, N., Soleimani, H., & Ghotbi, M. Y. (2012b). Microwave characterization of lanthanum iron garnet-filled PVDF-polymer composite using rectangular waveguide at X-band frequency. *Journal of Composite Materials*, *46*(12), 1497–1501.

Song, K. C., Lee, S. M., Park, T. S., & Lee, B. S. (2009). Preparation of colloidal silver nanoparticles by chemical reduction method. *Korean Journal of Chemical Engineering*, *26*(1), 153–155.

Sreekumar, P. A., Marc, J., Joseph, K., Unnikrishnan, G., & Thomas, S. (2012). Composites : Part A Electrical properties of short sisal fiber reinforced polyester composites fabricated by resin transfer molding. *Composites Part A*, *43*(3), 507–511.

Thongruang, W., Spontak, R. J., & Balik, C. M. (2002). Bridged double percolation in conductive polymer composites: An electrical conductivity, morphology and mechanical property study. *Polymer*, *43*(13), 3717–3725.

Vaisman, L., Wagner, H. D., & Marom, G. (2006). The role of surfactants in dispersion of carbon nanotubes. *Advances in Colloid and Interface Science*, *128–130*, 37–46.

Valmalette, J. C., Tan, Z., Abe, H., & Ohara, S. (2014). Raman scattering of linear chains of strongly coupled Ag nanoparticles on SWCNTs. *Scientific reports*, *4(5238)*, 1-8.

Van Etten, E. A., Ximenes, E. S., Tarasconi, L. T., Garcia, I. T. S., Forte, M. M. C., & Boudinov, H. (2014). Insulating characteristics of polyvinyl alcohol for integrated electronics. *Thin Solid Films*, *568*(1), 111–116.

Vázquez, E., & Prato, M. (2009). Carbon Nanotubes and Microwaves : *ACS Nano 2009, 3*(12), 3819–3824.

Wang, F., Arai, S. & Endo, M. (2004). Metallization of multi-walled carbon nanotubes with copper by an electroless deposition process. *Electrochem. Comm.* 6, 1042–1044.

Wang, Y., Duan, G., Zhang, L., Ma, L., Zhao, X., & Zhang, X. (2018). Terahertz Dispersion Characteristics of Super-aligned Multi-walled Carbon Nanotubes and Enhanced Transmission through Subwavelength Apertures. *Scientific Reports*, *8*(1), 1–10.

Wang, Z. (2007). Reinforcing Efficiency of Carbon Nanotubes in PVA Composites. Unpublished Doctoral thesis. Queen Mary, University of London.

Wei, H., & Eilers, H. (2009). From silver nanoparticles to thin films: Evolution of microstructure and electrical conduction on glass substrates. *Journal of Physics and Chemistry of Solids*, *70*(2), 459–465.

Xin, F., & Li, L. (2011). Composites : Part A Decoration of carbon nanotubes with silver nanoparticles for advanced CNT / polymer nanocomposites. *Composites Part A*, *42*(8), 961–967.

Yeum, J. H., Park, S. M., Kwon, I. J., Kim, J. W., Kim, Y. H., Rabbani, M. M., Hyun, J.M., Kim, K. & Oh, W. (2012). Carbon Nanotube Embedded Multi-Functional Polymer Nanocomposites. *Nanocomposites-New Trend and Developments*, Intech, 19–35.

Yuan, J. K., Li, W. L., Yao, S. H., Lin, Y. Q., Sylvestre, A., & Bai, J. (2011). High dielectric permittivity and low percolation threshold in polymer composites based on SiC-carbon nanotubes micro/nano hybrid. *Applied Physics Letters*, *98*(32901), 1-3.

Yuan, W., Jiang, G., Che, J., Qi, X., Xu, R., Chang, M. W. & Chan-park, M. B. (2008). Deposition of silver nanoparticles on multiwalled carbon nanotubes grafted with hyperbranched poly amidoamine) and their antimicrobial effects. *Journal of Physical Chemistry B*, *112*, 18754–18759.

Yuping, D., Ma, H., Shunhua, L., Xiaodong, C., Huifeng, C., Duan, Y., … Chen, H. (2008). Absorbing properties of α-manganese dioxide/carbon black double-layer composites. *Journal of Physics D: Applied Physics*, *41*(125403), 1-6.

Zhang, H. Bin, Yan, Q., Zheng, W. G., He, Z., & Yu, Z. Z. (2011). Tough graphene-polymer microcellular foams for electromagnetic interference shielding. *ACS Applied Materials and Interfaces*, *3*(3), 918–924.

Zhang, D., Hao, Z., Qian, Y., Huang, Y., Bizeng, Yang, Z., & Qibai, W. (2017). Simulation and measurement of optimized microwave reflectivity for carbon nanotube absorber by controlling electromagnetic factors. *Scientific Reports*, *7*(1), 1–8.

Zhang, D., Xu, F., Lin, J., Yang, Z., & Zhang, M. (2014). Electromagnetic characteristics and microwave absorption properties of carbon-encapsulated cobalt nanoparticles in 2-18-GHz frequency range. *Carbon*, *80*(1), 103–111.

Zhang, H., Smith, J. A., & Oyanedel-craver, V. (2011). The effect of natural water conditions on the anti-bacterial performance and stability of silver nanoparticles capped with different polymers. *Water Research*, *46*(3), 691–699.

Zhang, J., Mine, M., Zhu, D., & Matsuo, M. (2009). Electrical and dielectric behaviors and their origins in the three-dimensional polyvinyl alcohol/MWCNT composites with low percolation threshold. *Carbon*, *47*(5), 1311–1320.

Zhang, W., Li, W., Wang, J., Qin, C., & Dai, L. (2010). Composites of Polyvinyl Alcohol and Carbon Nanotubes Decorated with Silver Nanoparticles. *Fibers and Polymers*, *11*(8), 1132–1136. http://doi.org/10.1007/s12221-010-1132-3

Zhang, W., Xiong, H., Wang, S., Li, M., & Gu, Y. (2015). Electromagnetic characteristics of carbon nanotube film materials. *Chinese Journal of Aeronautics*, *28*(4), 1245–1254.

Zhang, X., Zhang, J., Quan, J., Wang, N., & Zhu, Y. (2016). Surface-enhanced Raman scattering activities of carbon nanotubes decorated with silver nanoparticles. *The Analyst*, *141*(19), 5527–5534.

Zhang, Y., Franklin, N.W., Chen, R.J. & Dai, H. (2000) Metal coating on suspended carbon nanotubes and its implication to metal–tube interaction, *Chem. Phys. Lett.* 331, 35–41.

Zhao, T., Hou, C., Zhang, H., Zhu, R., She, S., Wang, J., Li, T., Liu, Z. & Wei, B. (2014). Electromagnetic wave absorbing properties of amorphous carbon nanotubes. *Scientific Reports*, *4* (5619), 1–7.

Zhao, W., Li, M., Zhang, Z., & Peng, H. (2010). EMI shielding effectiveness of silver carbon nanotube sheets. *International Journal of Smart and Nano Materials*, *1*(4), 249–260.

Zhen, Y., Arredondo, J., & Zhao, G. (2013). Unusual Dielectric Loss Properties of Carbon Nanotube — Polyvinylidene Fluoride Composites in Low Frequency Region (100 Hz < f < 1 MHz). *Open Journal of Organic Polymer Materials*, *3*, 99–103.

LIST OF PUBLICATIONS

Academic journals

1. Yusof, Y., Zaidi, M. I., & Johan, M. R. (2016). Enhanced Structural, Thermal, and Electrical Properties of Multiwalled Carbon Nanotubes Hybridized with Silver Nanoparticles. *Journal of Nanomaterials*, 6141496, 1-9.

2. Yusof, Y., Ng, Z.Y, Wong, Y. H & Johan, M. R. (2018). The tunable permittivity of multi-walled carbon nanotubes/silver nanoparticles reinforced polyvinyl alcohol (PVA) nanocomposites at low frequency. *Mater. Res. Express* 5, 085604, 1-12.

Workshop/seminar

1. Yusof, Y., Ng, Z.Y, Wong, Y. H & Johan, M. R. (2017). Structural And Electrical Properties Of Silver Nanoparticles Decorated MWNT/Polyvinyl Alcohol Nanocomposites, Proceeding of National Workshop on Functional Materials, Physics Department, University of Malaya, pp. 23-28.